

**Optical coherence vibrography: a quantitative tool
for probing auditory and ocular biomechanics**

by

Antoine Ramier

M.A.Sc. Engineering Physics
Polytechnique Montreal (2014)
B.Eng. Engineering Physics
Polytechnique Montreal (2012)

Submitted to the Harvard-MIT Program in Health Sciences and
Technology

in partial fulfillment of the requirements for the degree of

Doctor of Philosophy

at the

MASSACHUSETTS INSTITUTE OF TECHNOLOGY

September 2019

© Massachusetts Institute of Technology 2019. All rights reserved.

Author
Harvard-MIT Program in Health Sciences and Technology
August 29, 2019

Certified by
Seok-Hyun Yun, PhD
Professor of Dermatology, Harvard Medical School
Thesis Supervisor

Accepted by
Emery N. Brown, MD, PhD
Director, Harvard-MIT Program in Health Sciences and Technology
Professor of Computational Neuroscience and Health Sciences and
Technology

Optical coherence vibrography: a quantitative tool for probing auditory and ocular biomechanics

by

Antoine Ramier

Submitted to the Harvard-MIT Program in Health Sciences and Technology
on August 29, 2019, in partial fulfillment of the
requirements for the degree of
Doctor of Philosophy

Abstract

Mechanical properties of biological tissues are inherently tied to their function. As such, they can provide direct insight into the structure and integrity of organs, and how they are affected by physiological and pathological processes. Optical coherence tomography (OCT) is a powerful imaging modality that can image the anatomy of biological tissues with near-cellular resolution. It can also be used to measure vibrations and deformations with nanometer-level sensitivity. This combination of tomography and vibrometry – OCT vibrography – forms a tool that is singularly positioned to quantify biomechanical behavior at the tissue scale.

This thesis focuses on two promising fields of application for OCT vibrography: otology and ophthalmology. Sound-driven vibrations in the middle-ear ossicular chain and in the tympanic membrane are fundamental to hearing. Using the chinchilla ear as a model, we investigate the vibrational amplitude and phase as a function of sound frequency. Our 3-dimensional measurements reveal with unprecedented detail the modes of motion of the ossicular chain of an intact middle-ear.

The ability of the cornea to focus light into a sharp image on the retina depends on its shape, which in turn is regulated by its mechanical properties. By measuring the velocity of mechanical waves, induced by an external stimulus and tracked using OCT vibrography, acoustic theory can be used to calculate the shear-elastic modulus of the corneal stroma. Our study demonstrates the first OCT-based quantification of corneal elasticity in live humans.

Thesis Supervisor: Seok-Hyun Yun, PhD
Title: Professor of Dermatology, Harvard Medical School

Acknowledgments

First and foremost, I wish to thank Prof. Andy Yun for his guidance and support. His patient confidence in my ability to overcome the numerous challenges of a research project and his unwavering enthusiasm have kept me going forward on many occasions. I cannot thank him enough for that. I leave his lab with the hope that I can retain just a small fraction of his incredible ability to think outside the box.

I also wish to thank all the members of the Yun Lab, starting with the small but amazing crew at our MGH satellite and with the so-called biomechanics subgroup. Amira Eltony, Behrouz Tavakol, Fatima Clouser, Imran Akca, Judith Birkenfeld, Liane Bernstein, Peng Shao ; I have learned much from you, struggled with you, but mostly had lots of fun working with all of you. Amira, as perhaps the colleague I have spent the most time with in the last couple of years, deserves a special mention. I will dearly miss our illuminating brainstorms and her intelligent optimism. I also had the chance of being supported in my work by 3 highly talented undergraduates and rotating students that I wish to thank: Yuanzhe Su, Yitong Chen and Yong-Chul Yoon. I am also most grateful for having been surrounded by all of the brilliant OCT minds that populate the 8th and 7th floor of Bartlett Hall. A special thanks to Norman Lippok and to Néstor Uribe-Patarroyo who helped me on so many occasions and from whom I have learned so much.

This work would not have been possible without the support of many people who worked for me behind the scenes: our two amazing lab admins, James Schulz and Jonathan Lawson, and the always so welcoming staff of the HST department. Brian Battersby also deserves my uttermost gratitude for developing and maintaining the software at the core of our OCT system. There are also many other people who have contributed to this work and that I wish to thank: Sarah Forward, Zeinab Hajjarian, Laurent Demanet, Stefan Kassumeh, Christian Wertheimer, Andreas Wartak.

Interdisciplinary research is based on collaboration, and I extend my gratitude to our numerous partners at the Massachusetts Eye and Ear. It was a pleasure to work with Prof. John Rosowski who provided precious guidance and mentorship, as well as

Michael Ravicz and Tao Cheng. I am also thankful to Dr. Amy Watts for her advice, enthusiasm and willingness to help us in our clinical study of cornea biomechanics.

I also wish to thank the members of this thesis committee, Profs. Dennis Freeman and Ming Guo. They have been incredibly available, enthusiastic and supportive, and their advice helped to crystallize my project into this final form.

I want to conclude on a more personal note by thanking all of the friends and family who have allowed me to remain (almost) sane after 5 years of doctoral studies. To all the incredible people I have met here in Boston, many of whom were already mentioned above: thank you again for those extraordinary years. To all the friends from home who crossed the border to visit me on so many occasions: you have no idea how much this meant to me. To my parents: over a lifetime, the list of things I should thank you for cannot hold on this page, but let me at least thank you for your unconditional love and support, and for instilling in me this appetite for learning. And finally, to Émilie: thank you for being my confidant, counselor, cheerleader, part-time project manager and scientific advisor, but mostly just for being the most amazing life partner I could ever wish for.

Contents

1	Introduction	15
1.1	Thesis organization	17
2	Background and Theory	19
2.1	Optical coherence tomography	19
2.1.1	OCT vibrometry	28
2.1.2	OCT elastography	31
2.2	Elastic waves in solids	35
2.2.1	Fundamental equations of linear elasticity	36
2.2.2	Guided waves in plates	40
2.3	Middle ear imaging and vibrometry	51
2.3.1	Imaging the middle ear with OCT	52
2.3.2	Vibrometry of the auditory system	53
2.4	Cornea biomechanics	54
2.4.1	Corneal anatomy and histology	55
2.4.2	Collagen structure and organization	57
2.4.3	Complex mechanical behavior of the cornea	60
2.4.4	Measuring cornea biomechanical properties	61
3	Middle-ear vibrography	69
3.1	Introduction	70
3.2	OCT vibrography system	71
3.2.1	Optical system, sound stimulus, and time synchronization . .	71

3.2.2	Data acquisition in synchrony with sound frequency	73
3.2.3	Data processing to determine the amplitude and phase of vibration	74
3.2.4	System performance measurement: Phase sensitivity and stability	76
3.3	Results of chinchilla ear measurements	79
3.3.1	Vibrography imaging of the chinchilla middle ear	79
3.3.2	Acoustic transfer function of the middle ear	80
3.3.3	Projected and volumetric vibrography images of the TM and ossicular chain	83
3.4	Discussion	86
4	Measuring cornea mechanical properties using optical coherence elas-	
tography		89
4.1	Introduction	90
4.2	OCE system	91
4.3	Data processing and validation using an elastomer	93
4.3.1	Displacement field	93
4.3.2	Dispersion measurement	95
4.4	Elastography of the cornea	100
4.4.1	Displacement field and dispersion	100
4.4.2	Viscoelasticity	103
4.4.3	Correlation of wave velocity with anatomical parameters . . .	106
4.5	Discussion and conclusion	108
5	Mechanical characterization of the human cornea <i>in vivo</i> using opti-	
cal coherence elastography		113
5.1	Introduction	114
5.2	Results	116
5.2.1	Mechanical model of wave propagation in the cornea	116
5.2.2	Mechanical wave velocity in human cornea	120
5.2.3	Factors influencing wave velocity	123
5.3	Discussion	126

5.4 Materials and Methods	127
5.4.1 Study design	127
5.4.2 Instrument design	127
5.4.3 Imaging protocol	128
5.4.4 Displacement field measurement	130
6 Conclusion and outlook	133

List of Figures

1-1 Comparison of OCT with other imaging modalities in terms of resolution and depth of penetration	15
2-1 Elementary interferometer for OCT	20
2-2 Example autocorrelation function for a Gaussian source	22
2-3 Elementary OCT system with multiple reflectors	23
2-4 Time-domain LCI example with multiple reflectors	24
2-5 Principle of Fourier-Domain OCT	27
2-6 Motion detection using OCT	29
2-7 Schematic of OCT elastography techniques	32
2-8 Mechanical wave propagation in an infinite, linear elastic medium . .	39
2-9 Geometry and variable definitions for the fluid-plate-vacuum system .	40
2-10 Example wave velocities and mode shapes	50
2-11 Anatomy of the middle and inner ear	51
2-12 Corneal anatomy and histology	55
2-13 Molecular structure of collagen fibrils	58
2-14 Hierarchical arrangement of collagen cornea	59
3-1 Schematic of the optical system	72
3-2 Timing diagrams of data acquisition, sound wave, and beam position	74
3-3 Measured SNR and sensitivity	78
3-4 OCT images of the chinchilla middle ear	81
3-5 Acoustic transfer function of the ossicular chain	82
3-6 Projection view of the TM vibration	84

3-7	Projection view of the ossicular chain	85
3-8	Reconstructed ossicular motion	86
4-1	Probe schematic and stimulus waveforms	92
4-2	Displacement field of elastic waves at the surface of an elastomer phantom	95
4-3	Processing steps to compute the mechanical wave dispersion	96
4-4	Measured phase velocity and comparison with shear rheometry (phantom)	99
4-5	Porcine eye experiment schematic and displacement field profile	101
4-6	Phase velocity measurement of porcine corneas	102
4-7	Parameter estimation using the Lamb wave model	105
4-8	Wave attenuation measurement of porcine corneas as a function of frequency	106
4-9	Shear modulus of porcine corneas as a function of weight, thickness and radius of curvature	107
5-1	Multilayer model of the cornea	119
5-2	Lamb wave spectrum and mode shapes	120
5-3	System used for <i>in vivo</i> corneal elastography	121
5-4	Wave propagation in a human cornea <i>in vivo</i>	122
5-5	Key processing steps for measuring the corneal elastic wave velocity and attenuation	122
5-6	Distribution of the measured wave velocities as a function of frequency for each subject	124
5-7	Factors influencing wave velocity	125
5-8	Stimulus waveforms and scanning pattern used for <i>in vivo</i> OCE	129

List of Tables

2.1	Boundary conditions in linear elastodynamics	45
2.2	Relative weight of the different cornea components	56
2.3	Methods used for biomechanical measurements of the cornea	62

Chapter 1

Introduction

Optical coherence tomography (OCT) is an emerging medical imaging modality that can perform high speed cross-sectional and volumetric imaging of biological tissues. With a typical resolution on the order of 5 to 15 microns and a depth of penetration on the order of a few millimeters, it bridges the gap between high-resolution *ex vivo* microscopy and conventional medical imaging technologies (Fig. 1-1).

Since the introduction of this technology in the early 90's [67], OCT has become a standard-of-care ophthalmic imaging technology, with about 30 million scans performed yearly [38]. The use of OCT is also rapidly growing in the fields of gastroenterology,

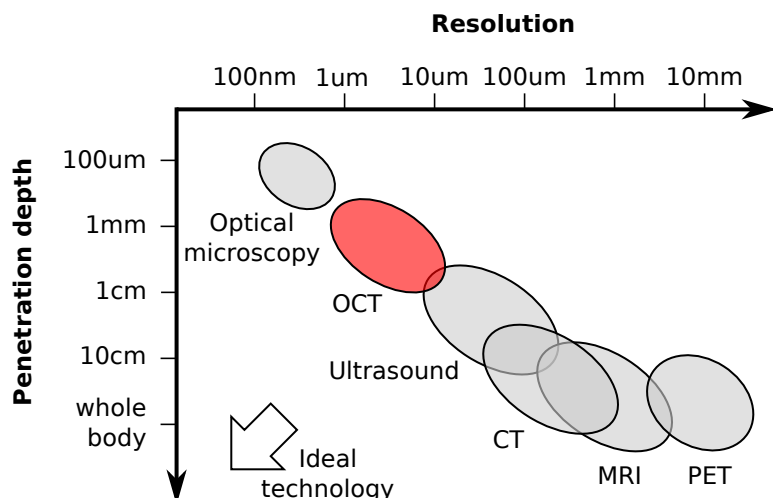


Figure 1-1: Comparison of OCT with other imaging modalities in terms of resolution and depth of penetration.

otolaryngology, dermatology, cardiovascular imaging, and non-destructive testing.

Standard OCT images are based on light scattering intensity: tissues that reflect more light appear brighter, and vice versa. While this type of contrast can provide important information on tissue structure and organization, there is a well recognized need for extending the functionality of OCT beyond pure anatomical imaging. These functional extensions, collectively known as contrast-enhanced or functional OCT, include the highly successful OCT angiography and polarization-sensitive OCT [91, 130]. Optical coherence vibrography (OCV) and elastography (OCE), which form the core of this thesis, are other functional extensions of OCT.

OCV – Mapping vibrations of the auditory system

OCV measures vibrations and deformations in biological tissues in 3 dimensions and as a function of time. The vibrations are generated by an external mechanical stimulus that is synchronized with the OCT acquisition, such that both the amplitude and phase of the mechanical vibration can be obtained with good accuracy. The displacement sensitivity of OCV can be on the scale of 1 nm, about 3 to 4 orders of magnitude smaller than the resolution of OCT imaging [23]. The unique combination of high-resolution imaging and high-sensitivity vibrometry is a defining feature of OCV that can be harnessed to provide information on the dynamic behavior of moving tissues.

One promising application of OCV is to characterize sound transduction in the auditory system. Because transmitting and detecting vibrations is the intrinsic function of the ear, measuring the detailed vibratory motions within the hearing organ is critical in understanding the role of specialized tissues and structures, in validating theoretical models against accurate experimental data, and in uncovering unknown mechanisms. While other methods such as laser Doppler vibrometry can measure vibrations with high sensitivity, they only measure displacement at the surface of a sample, rely on exogenous probes, and thus require invasive surgical preparation [153, 158]. OCV is the only known approach that can make such measurements below the surface of an intact tympanic membrane. It is therefore simple to use, less invasive than

existing methods, and greatly enhances spatial resolution. This opens up new avenues in hearing research, and has the potential to diagnose and analyze various pathologies of the middle ear [22].

OCE – Quantitative corneal biomechanics

The goal of OCE is to map the mechanical properties (for example Young's modulus) of biological tissues. It is highly linked to OCV as mechanical measurements are accomplished by inducing a mechanical stimulus in biological tissues and measuring the resulting deformation with OCT. Mechanical properties of biological tissues often dictate their ability to play their physiological role. Changes in the mechanical behavior can thus reflect a loss of structural integrity and provide important information about physiological and pathological processes.

There is a large body of scientific evidence that biomechanics play critical roles in numerous corneal diseases and treatments. The loss of mechanical strength is a hallmark of ectatic disorders, including keratoconus and iatrogenic ectasia [9, 40, 119]. These mechanical changes are thought to drive the geometrical abnormalities observed clinically. New tools such as OCE for evaluating corneal biomechanics offer great opportunities for improvement over current approaches, from earlier and more sensitive diagnosis to personalized risk assessment and treatment planning.

1.1 Thesis organization

Chapter 2 presents the theoretical foundations and the background information over which the rest of the thesis is built. It first lays out the basic concepts of OCT imaging, phase-sensitive vibration sensing (OCV), and how elastic properties of materials can be assessed (OCE). It then presents the fundamentals of linear elasticity, with an emphasis of anisotropic materials and guided waves in plates. The later sections of chapter 2 present the general anatomy and physiology of the middle ear and cornea, and review specific literature on imaging, vibrometry and mechanical characterization of these tissues.

Chapter 3 presents our progress in developing 3-dimensional, sound-synchronous measurements of mechanical vibrations, in the context of middle ear imaging. We demonstrate measurements of the vibration amplitude and phase of the tympanic membrane and the ossicular chain over a significant part of the auditory frequency range, with high spatial resolution. Results can be shown as intuitive motion pictures which reveal the detailed modes of motion of the ossicles.

Chapter 4 describes how OCV can be used to quantitatively measure the mechanical properties of viscoelastic tissues. We present a simple scheme to excite acoustic waves at the corneal anterior surface using a piezoelectrically-driven vibrating probe. This study focuses on the frequency dependence of wave velocity and its impact on elastic modulus estimation.

Chapter 5 builds upon the methods developed in chapter 4 and presents the first-in-human implementation of this technology. A refined model involving corneal anisotropy is presented, which provides a more rigorous description the corneal mechanical behavior in relationship with its microstructure.

Finally, chapter 6 concludes this dissertation by discussing some of the future perspectives for OCV and OCE.

Chapter 2

Background and Theory

2.1 Optical coherence tomography

Optical coherence tomography (OCT) is an imaging modality that produces high-resolution cross-sectional images of tissues and materials. It can be understood as an optical analogue to pulse-echo ultrasound imaging: a wave is sent towards the target tissue, and images are formed by measuring the intensity and depth at which this wave is backscattered within the sample.

In OCT, measuring the depth at which a light echo was produced is not achieved by a direct time-of-flight measurement as in ultrasonography. Instead, depth discrimination is based on the concept of low coherence interferometry (LCI), or white light interferometry. In this section, the fundamentals of LCI and OCT are introduced. The developments follow closely those of Refs. [16, 38].

Mathematical description of low-coherence light

LCI uses a broadband, incoherent light source, which can equivalently be described in the time or frequency domain. In the time domain description, the electric field $E(t)$ is a random variable, generally considered to be governed by stationary and ergodic stochastic process. The autocorrelation function $\Gamma(\tau)$ and the normalized correlation

function (degree of coherence) $\gamma(\tau)$ of the electric field are defined by:

$$\Gamma(\tau) = \langle E^*(t)E(t - \tau) \rangle \quad (2.1)$$

$$\gamma(\tau) = \frac{\Gamma(\tau)}{\Gamma(0)} = \frac{\langle E^*(t)E(t - \tau) \rangle}{\langle |E(t)|^2 \rangle} \quad (2.2)$$

where τ is a time delay variable, $\langle \cdot \rangle$ represents an ensemble average, and $*$ denotes complex conjugation.

In the frequency domain, the field is described as an integral superposition of monochromatic waves $E(\omega)$:

$$E(t) = \int E(\omega)e^{j\omega t}d\omega \quad (2.3)$$

where ω is the angular frequency.

The power spectral density, or spectrum of the light source, defined by $S(\omega) = \langle |E(\omega)|^2 \rangle$ forms a Fourier transform pair with the autocorrelation function by virtue of the Wiener-Kintchin theorem:

$$\Gamma(\tau) = \int S(\omega)e^{j\omega\tau}d\omega \quad (2.4)$$

Interference of low-coherence light

To describe the interference of low-coherence light, consider a simple interferometer system as shown in Fig. 2-1.

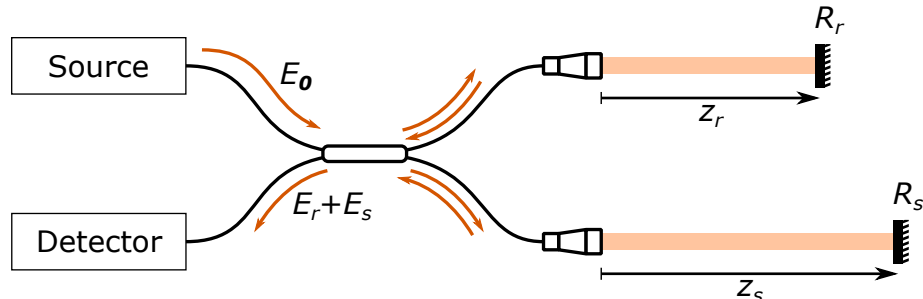


Figure 2-1: Elementary interferometer for OCT imaging with a single reflector in the sample path.

The electric field produced by the light source E_0 is divided in two beam paths: a reference path and a sample path, indicated by subscripts r and s , respectively. Light travels over a certain distance (z_r and z_s) before reaching reflectors R_r and R_s which reflect back the two beams. The beams are then recombined after traveling total distances of $2z_r$ and $2z_s$. The resulting fields E_r and E_s at the detector originate from the same source, and can be considered as simple delayed and scaled copies of the source: $E_r(t) = a_r E_0(t)$ and $E_s(t) = a_s E_0(t - \tau)$. A unique time delay variable $\tau = 2(z_s - z_r)/c$ can be defined without loss of generality as the delay associated with pathlength difference $z_s - z_r$. The coefficients a_r and a_s are amplitude scaling coefficients that lump the power reduction effects from various sources, including the partially reflecting mirrors and the transmission coefficients of the beam splitter.

The resulting electric field at the detector is given by the sum of the reference and sample fields $E_r + E_s$. The time-averaged intensity measured by the detector is given by:

$$I = \langle |E_r + E_s|^2 \rangle = \langle E_r^* E_r \rangle + \langle E_s^* E_s \rangle + \langle E_r^* E_s \rangle + \langle E_r E_s^* \rangle \quad (2.5)$$

$$= a_r^2 \langle |E_0|^2 \rangle + a_s^2 \langle |E_0|^2 \rangle + a_r a_s \langle E_0^*(t) E_0(t - \tau) \rangle + a_r a_s \langle E_0(t) E_0^*(t - \tau) \rangle \quad (2.6)$$

We recognize the $\langle |E_0|^2 \rangle$ factor in the two first terms of Eq. (2.6) as the total intensity from the source I_0 . The expression $\langle E_0^*(t) E_0(t - \tau) \rangle$ in the third and fourth terms represents the autocorrelation function of the source. We can thus rewrite Eq. (2.6) as

$$I(\tau) = (a_r^2 + a_s^2) I_0 + 2a_r a_s \operatorname{Re}(\Gamma(\tau)) \quad (2.7)$$

$$= I_0 (a_r^2 + a_s^2 + 2a_r a_s \operatorname{Re}(\gamma(\tau))) \quad (2.8)$$

To illustrate the meaning of equation (2.8), consider a source with a Gaussian spectrum centered around ω_0 and a spectral width defined by its standard deviation σ_ω :

$$S(\omega) = S(\omega_0) e^{-\frac{1}{2} \left(\frac{\omega - \omega_0}{\sigma_\omega} \right)^2} \quad (2.9)$$

The autocorrelation function of such a source, by virtue of Wiener-Kintchin's theorem, is given by the normalized Fourier transform of $S(\omega)$:

$$\gamma(\tau) = e^{i\omega_0\tau} e^{-\frac{1}{2}\left(\frac{\tau}{\sigma_\tau}\right)^2} \quad (2.10)$$

where $\sigma_\tau = 1/\sigma_\omega$ is a measure of the temporal coherence of the source (here defined as a standard deviation; the precise term “coherence time” is generally reserved for the corresponding full width at half-maximum $\tau_c = 2\sqrt{2\ln 2}$) . If we substitute this in the expression for the detected intensity of our simple single-reflector interferometer system, we get

$$I(\tau) = I_0 \left(a_r^2 + a_s^2 + 2a_r a_s \cos(\omega_0\tau) e^{-\frac{1}{2}\left(\frac{\tau}{\sigma_\tau}\right)^2} \right) \quad (2.11)$$

This equation is illustrated in Fig. 2-2. As we vary the delay between the two beam paths (for example by moving one of the mirrors), the detected signal oscillates between constructive and destructive interference due to the $\cos(\omega_0\tau)$ factor. This oscillation is modulated by an envelope function (in this case a Gaussian envelope of standard deviation σ_τ) that represents the effect of temporal coherence of the stochastic broadband light. Far from the zero-delay point ($|\tau| \gg 0$), waves interfere completely incoherently, and the detected intensity is simply the sum of the transmission coefficients times the source power.

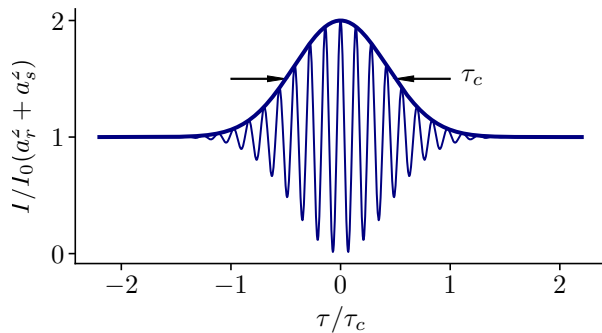


Figure 2-2: Example autocorrelation function for a Gaussian source.

Multiple reflectors

A case of much greater practical importance is when multiple partial reflectors are positioned the sample arm of the interferometer (Fig. 2-3), which occurs when a biological sample is analyzed. The expressions derived above can be generalized by considering the total field from the sample arm as a sum of N individual scattered fields $E_n = a_n E_0(t - \tau_n)$ identified with subscript n and associated with their own amplitude a_n and delay τ_n corresponding to a position $z_n = c\tau_n/2$:

$$E_s = \sum_{n=0}^N a_n E_0(\tau_r - \tau_n) \quad (2.12)$$

where τ_r is the time delay in the reference arm.

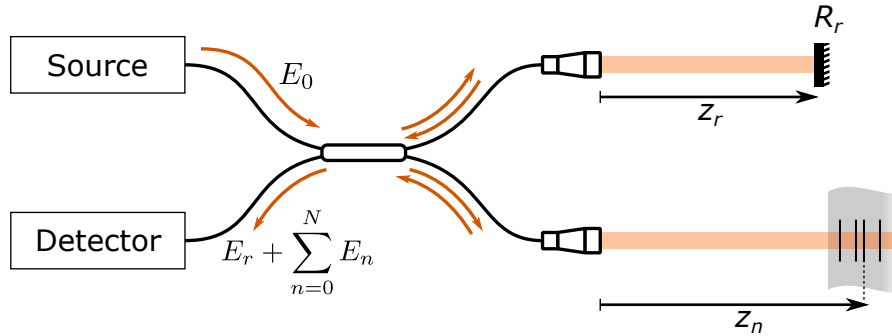


Figure 2-3: Elementary OCT system with multiple reflectors in the sample arm

Following the same steps as in the single-reflector case, we arrive at the expression:

$$\begin{aligned} I(\tau_r) &= I_0 \left(a_r^2 + \sum_{n=1}^N a_n^2 + 2a_r \sum_{n=1}^N a_n \operatorname{Re}(\gamma(\tau_r - \tau_n)) \right. \\ &\quad \left. + \sum_{n=1}^N \sum_{m \neq n} a_n a_m \operatorname{Re}(\gamma(\tau_n - \tau_m)) \right) \end{aligned} \quad (2.13)$$

The first two terms in equation (2.13) are constants (commonly referred to as D.C. terms) that represent the average power reflected by the reference mirror and by each individual sample reflector. The third term is given by the interference between the signal from the reference reflector with that of each sample reflector (also referred to as

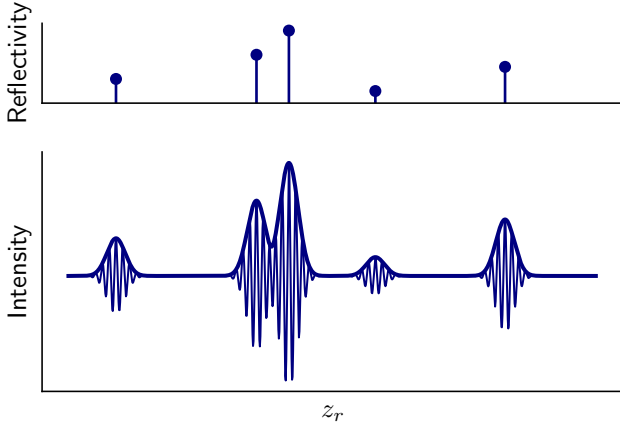


Figure 2-4: Reflectivity profile of a sample composed of a few scattering particles and corresponding time-domain LCI measurement

the cross-correlation term). It can be seen as a series of copies of the autocorrelation function $\gamma(\tau)$, offset by τ_n . The last term represent the interference between each possible pair of sample reflectors (also referred to as the auto-correlation term). This term is constant and generally small compared to the cross-correlation term.

Equation (2.13) forms the basis of the so-called time-domain OCT (TD-OCT). In this implementation, the reflectivity profile of the sample is measured by varying the position of the reference mirror z_r , which effectively varies the time delay variable $\tau_r = z_r/c$. Figure 2-4 shows an example TD-LCI measurement of a sample that would be composed of 5 scatterers with different reflectivities.

The measured intensity is essentially a repetition of the autocorrelation function, with different amplitudes, centered around the position of each scatterer. If the interference trace is low-pass filtered to keep only the envelope (thick curve), then this measurement represents an approximation of the sample reflectivity profile as a function of depth. A single reflectivity profile is known as an A-line. To compose a complete OCT scan, multiple A-lines are obtained at different transverse locations in the sample and displayed size by side as an image, known as a B-scan.

Fourier-Domain OCT

Up to now, the analysis of LCI was conducted using the time-domain description of low-coherence light. Equivalently, we can consider the problem in the Fourier

domain. Given the linearity of the system, each frequency component in the Fourier decomposition can be treated separately. The field at a given frequency is expressed as:

$$E(z, t) = E(k, \omega)e^{i(kz - \omega t)} \quad (2.14)$$

where $k = 2\pi/\lambda$ is the wavenumber. Once again, the reference and sample-arm fields are expressed as scaled and offset copies of the source field $E_0(k, \omega)$

$$E_r = a_r E_0(k, \omega)e^{i(2kz_r - \omega t)} \quad (2.15)$$

$$E_s = \sum_n a_n E_0(k, \omega)e^{i(2kz_n - \omega t)} \quad (2.16)$$

where the factor 2 in the exponentials comes from the round-trip travel of the lightwave. The detected intensity is computed by substituting the field expressions in Eq. (2.5), which yields

$$\begin{aligned} I(k) = S(k) & \left(a_r^2 + \sum_{n=1}^N a_n^2 + 2a_r \sum_{n=1}^N a_n \cos(2k(z_n - z_s)) \right. \\ & \left. + \sum_{n=1}^N \sum_{m \neq n} a_n a_m \cos(2k(z_n - z_m)) \right) \end{aligned} \quad (2.17)$$

where $S(k) = \langle |E_0(k, \omega)|^2 \rangle$ is by definition the power spectral density of the source.

We now calculate the Fourier transform of Eq. (2.17) with respect to k . The calculation makes use of the Fourier transform pairs $\cos(kz_0) \xleftrightarrow{FT} (\delta(z - z_0) + \delta(z + z_0))/2$ and $F(k)G(k) \xleftrightarrow{FT} f(z) \otimes g(z)$, as well as Wiener-Kintchin's theorem $S(k) \xleftrightarrow{FT} \gamma(z)$ and the sifting property of the Dirac function $f(z) \otimes \delta(z - z_0) = f(z - z_0)$. The origin of the z axis is also redefined with respect to the reference mirror position.

We omit the algebra and present the final result:

$$\begin{aligned}
I(z) = & \gamma(z) \left(a_r^2 + \sum_{n=1}^N a_n^2 \right) \\
& + 2a_r \sum_{n=1}^N a_n (\gamma(z - z_n) + \gamma(z + z_n)) \\
& + \sum_{n=1}^N \sum_{m \neq n} a_n a_m (\gamma(z - (z_n - z_m)) + \gamma(z + (z_n - z_m)))
\end{aligned} \tag{2.18}$$

We recognize the same overall form as previously encountered in our study of TD-OCT: a sum of scaled and shifted copies of the autocorrelation function of the source. We also identify DC terms (first line), cross-correlation terms (second line) and auto-correlation terms (third line).

As seen previously, the dominant cross-correlation terms of Eq. 2.18 can be interpreted as a measurement of the reflectivity profile of the sample, widened by the autocorrelation function of the source. The remarkable implication of this is that the reflectivity profile of the sample can be recovered by a *spectral* measurement, without requiring to move the reference mirror. If the intensity of the interfering light is measured at a series of discrete wavelengths, the reflectivity can be simply reconstructed by performing a discrete Fourier transform (DFT) of the measurement. The magnitude of the DFT then represents the reflectivity profile of the sample, broadened by the width of the source autocorrelation function. This method is known as Fourier-Domain OCT (FD-OCT).

Figure 2-5 presents a visual interpretation of equations (2.18) and (2.17). Only the cross-correlation terms are shown for simplicity. The interference fringes (bottom-left panel) coming from reflectors at different positions (top-right panel), are read as sinusoids with different periods (gray curves). They are summed to form the overall interferogram (blue curve). Since the frequency of each sinusoid is equal to $2(z_n - z_r)$, the Fourier transform (bottom-right panel) forms a peak corresponding to the position of each reflector. Because the Fourier transform is a linear operation, the combined signal (A-line) represents the reflectivity profile of the sample.

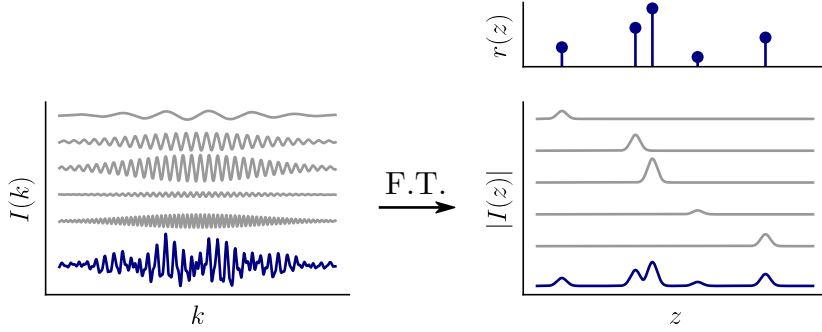


Figure 2-5: Principle of Fourier-Domain OCT. Top-right: position and reflectivity of various scatterers in the sample arm. Bottom-left: Interferogram corresponding to each reflector (gray) and the whole sample (blue). Bottom-right: The reflectivity profile is obtained by Fourier transformation of the interferograms.

FD-OCT has two main advantages over its time-domain counterpart. First, no moving part is required to scan the position of the reference mirror, which enables considerably faster imaging speed. Second, there is a significant signal-to-noise advantage in performing the measurement in the Fourier domain, which originates from the fact that in FD-OCT, light coming from all depths is usable for any given measurement, whereas in TD-OCT only the light originating from the point of zero-delay contributes to the signal [199].

Finally, we note that there are two practical implementations of Fourier-Domain OCT. One way is to use a broadband light source that illuminates the sample with all wavelengths at once. Spectral components are then separated at the point of detection using a spectrometer (diffraction grating and line-scan camera). This approach is known as spectral-domain OCT (SD-OCT). The second approach is to use a wavelength-swept laser. Only one wavelength illuminates the sample at any given time, and the signal can be measured using a fast, discrete detector such as a photodiode. Different time points then correspond to different wavelengths. This method is known either as swept-source OCT (SS-OCT) or optical frequency-domain imaging (OFDI). Both SD- and SS-OCT offer the same benefits in terms of improved SNR and acquisition speed compared to TD-OCT, but there are subtle differences in their relative advantages in shortcomings. As a general rule of thumb, spectral-domain systems can offer higher resolution and lower costs, whereas swept-source systems

boasts the fastest acquisition speeds and allow deeper imaging ranges.

2.1.1 OCT vibrometry

We now examine the question of how to detect vibrations and deformations in tissues using optical coherence tomography. For simplicity, consider the signal of a basic interferometer with a single reflector placed in the sample arm, as was first illustrated in Fig 2-1. The Fourier-domain signal given by Eq. (2.17) becomes:

$$I(k) = S(k)(a_r^2 + a_s^2 + 2a_r a_s \cos(2kz_s)) \quad (2.19)$$

where z_s is the position difference between reference and sample reflector. After Fourier transformation, this expression becomes:

$$I(z) = \gamma(z) \otimes (a_r^2 + a_s^2 + 2a_r a_s (\delta(z - z_s) + \delta(z + z_s))) \quad (2.20)$$

Where $\gamma(z)$ is the autocorrelation function of the source given by Wiener-Kintchin's theorem. If the source spectrum $S(k)$ is bandwidth limited around a central wavenumber k_0 , a valid hypothesis for real-world broadband sources, $\gamma(z)$ takes the form:

$$\gamma(z) = e^{2ik_0z} \gamma_0(z) \quad (2.21)$$

where $\gamma_0(z)$ is the Fourier-transform of the source spectrum after centering it around the center wavenumber k_0 . For example, if the source is Gaussian, then $\gamma_0(z)$ is the real-valued envelope $\gamma_0(z) = e^{-\frac{1}{2}(\frac{z}{\sigma_z})^2}$. With this definition, the complex-valued, z -domain A-line profile can then be expressed in the perhaps more instructive form:

$$I(z) = e^{ik_0z} (\gamma_0(z)(a_r^2 + a_s^2) + 2a_r a_s (\gamma_0(z - z_s)e^{-2ik_0z_s} + \gamma_0(z + z_s))e^{2ik_0z_s})) \quad (2.22)$$

Let's now examine what happens if we let the sample reflector position be a function of time. We will define its initial position as z_0 and consider a small displacement from this initial position $u_z(t)$, such that $z_s(t) = z_0 + u_z(t)$. We can immediately see that this

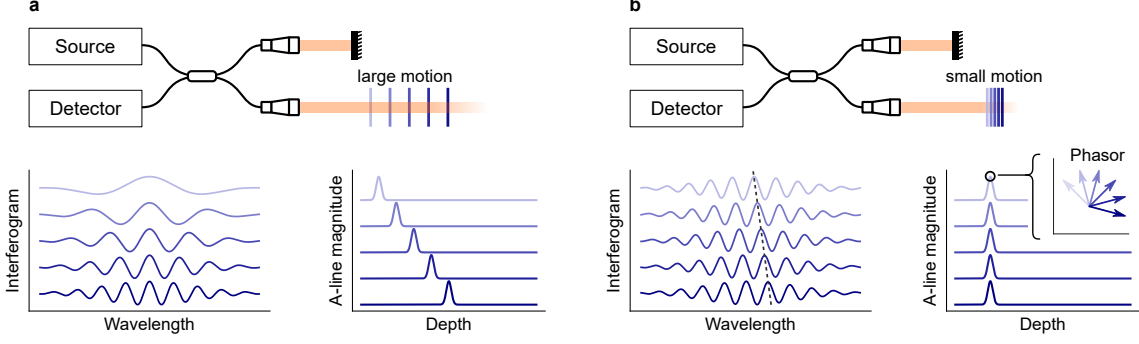


Figure 2-6: Motion detection using OCT. (a) Intensity tracking for large displacements. (b) Phase-sensitive detection for sub-resolution motion.

results in a small offset in the envelope function $\gamma_0(z - z_s) \rightarrow \gamma_0(z - (z_0 + u_z(t)))$, and that the complex exponential term $e^{2ik_0z_s}$ undergoes a phase change $\Delta\phi(t) = 2k_0u_z(t)$.

We can conclude from this analysis that there are essentially two ways of measuring axial displacements with OCT, which are illustrated in Fig. 2-6. First, we can directly track the position shift of the peak $\gamma_0(z - z_s)$ from the magnitude of $I(z)$. In principle, this can be achieved with good accuracy, but it is challenging for subpixel displacements in the presence of multiple scattering reflectors. The second approach is to use the phase of $I(z)$, which at a given depth z is related to the displacement by:

$$\Delta\phi(t) = 2k_0u_z(t) \iff u_z(t) = \frac{\lambda_0}{4\pi}\Delta\phi(t) \quad (2.23)$$

where k_0 and λ_0 are the central wavenumber and wavelength of the source. This approach is known as phase-sensitive OCT, and is most widely used in OCT vibrometry.

Importantly, we note that the absolute phase in an OCT measurement is difficult to obtain because the phase can wrap multiple times within a single pixel. Consequently, only the relative displacement of scatterers can be obtained from changes in the phase $\Delta\phi$.

An important limitation of phase-sensitive detection is that it can only measure the axial (z) component of the displacement (parallel to the axis of the probing OCT beam). Also, phase measurement may present phase-wrapping errors when the displacement amplitude is greater than the optical wavelength.

Also note that the overall phase of $I(z)$ is ultimately determined by that of all its

reflectors. However, because the function $\gamma(z)$ is sharply peaked, the local phase is dominated by the motion of the reflectors that are within the width of $\gamma(z)$, usually one to a few neighboring pixels. This principle is known as coherence gating.

Sensitivity of displacement measurements

The smallest displacements that can be measured in phase-sensitive OCT is ultimately dictated by the signal to noise ratio (SNR) of the OCT measurement. The complex-valued FD-OCT signal after Fourier-transformation can be described by a large deterministic constant (the signal, X_0) plus a random phasor with a Gaussian distribution (the noise, δX). It can be shown that if the SNR is high, then the phase ϕ of the combined signal $X = X_0 + \delta X$, is approximately Gaussian with a variance $\text{VAR}[\phi] = \text{VAR}[\delta X]/X_0^2 = 1/\text{SNR}$ [57].¹ This result can be used to show that the smallest (noise-equivalent) displacement σ_u that can be measured with phase-sensitive OCT is:

$$\sigma_u = \frac{\lambda}{4\pi} \frac{1}{\sqrt{\text{SNR}}} \quad (2.24)$$

Phase-based displacement measurements can be remarkably sensitive. For example, brighter areas on an OCT image can have SNR on the order of 40 dB. For a typical center wavelength of 1300 nm, the displacement sensitivity is approximately 1 nm. This is 3-4 orders of magnitude smaller than the axial resolution and pixel size in OCT imaging.

It is worth mentioning that other noise sources, such as mechanical vibrations of optical components in an OCT system can increase the phase noise above the fundamental SNR limit. Some of the noise may be reduced by common-path interferometer designs [27]. Wavelength swept lasers in swept-source OCT tend to introduce

¹This result evidently breaks down if the random phasor becomes as large or larger than the constant, because the probability distribution of the phase would extend beyond $\pm\pi$. The general expression for the probability density function is

$$p(\phi) = \frac{e^{-\xi^2/2}}{2\pi} + \frac{\xi \cos \phi}{\sqrt{2\pi i}} e^{-(\xi^2 \sin^2 \theta)/2} \Phi(\xi \cos \phi)$$

where $\Phi(x) = 1/\sqrt{2\pi} \int_{-\infty}^x e^{-y^2/2} dy$ and $\xi = X_0/\sqrt{\text{VAR}[\delta X]}$.

additional noise due to phase jitter between wavelength sweep cycles and the data acquisition clock. This problem can be resolved by introducing a calibration mirror in a secondary sample arm [186], or by k-clocking (synchronizing the acquisition of each sample point with the source wavelength sweep) using an external interferometer [17].

2.1.2 OCT elastography

OCT elastography (OCE) is the use of OCT to map the mechanical properties of biological tissues. It was originally proposed by Schmitt in 1998 [163], but has recently started to receive considerable attention, following the progress of high-speed and phase-sensitive OCT technology.

Much of the original concepts of OCE were originally developed for the more mature fields of ultrasonic imaging and magnetic resonance imaging (MRI) [53, 105], but the unique balance of resolution, penetration and imaging speed offered by OCT makes it an ideal modality for imaging certain organs, including the eye and the ear.

The interest in mapping the mechanical properties is that pathological processes often modify the structure and integrity of tissues. Simply put, diseased tissues often appear either softer or stiffer than their normal counterpart, a fact that has been used for centuries by physicians who perform manual palpation to probe these changes. Elastography could therefore be used for diagnosis, clinical evaluation, or various research purposes in biomedicine.

There are numerous implementations and variations of OCT elastography, but their basic principle can generally be summarized in 3 key steps. First, a mechanical stimulus or perturbation is applied to the tissue being measured. Second, the tissue deformation resulting from the applied load is quantified using OCT. Finally, given the known stimulus and deformation, some mechanical model of tissue response can be used to infer the tissue properties.

The second component, measuring tissue deformation, has been presented in section 2.1.1 above. The third component, mechanical modeling, requires a relatively detailed discussion of continuum mechanics, and will be covered in section 2.2. The main purpose of this section will therefore be to present a taxonomy of the different

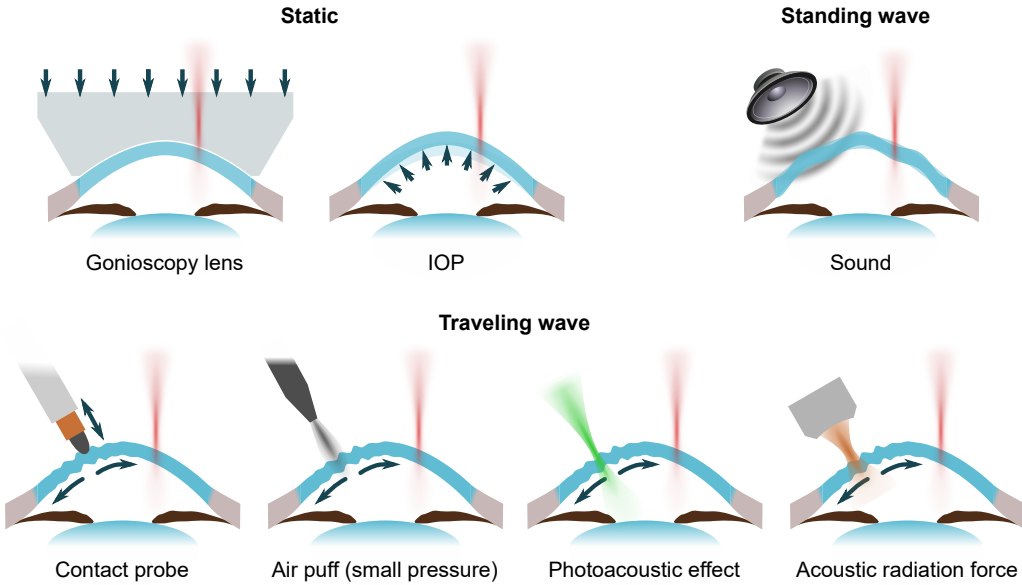


Figure 2-7: Schematic of OCT elastography techniques. Various loading methods that have been employed to induce a mechanical perturbation in the tissue. They can be classified in 3 broad categories based on the type of stimulus and on the data analysis paradigm: quasi-static compression, standing wave (resonance) and traveling acoustic waves.

types of OCE, with a focus on corneal applications. We will also provide some examples of approaches used for mechanical stimulation.

OCE techniques can be classified in 3 broad groups based on the type of stimulus used, which generally dictates the mechanical model to be applied: quasi-static, standing waves and traveling waves. Those categories, as well as some practical examples of stimulus methods, have been illustrated in Fig. 2-7.

Quasi-static OCE

Quasi-static or compression OCE was the first proposed approach in Schmitt's original work [163] and was also the first one adapted for ophthalmic applications [48]. It is based on a simple concept: under mechanical load, softer tissues tend to deform more than stiffer ones. Typically, the external stress is applied by compressing the tissue with a contact device, such as an objective lens or a transparent plate.

This simple and robust method has considerable potential for measurements of the skin or ex vivo tissue samples [3, 45, 76], but was not as commonly used for

ophthalmic applications. One possible reason is that many researcher have preferred to develop non-contact methods. Another limitation of this method is that solving the inverse problem of computing the material elasticity from the measured deformation is not simple [35], and is likely to be further complicated by the presence of the liquid aqueous humor in the anterior chamber, behind the cornea. Nonetheless, this OCE method is the only one that has been used clinically [49, 50].

Another variant of static OCE is to externally modulate intraocular pressure as a loading mechanism. Proof-of-concept experiments were performed on *ex vivo* corneal explants [48, 52], but this approach seems unsuited for clinical applications.

Traveling wave OCE

Traveling wave OCE has been extensively used for corneal elastography. The basic principle of operation was adapted from shear wave elastography in ultrasound imaging. It uses a localized energy source to excite mechanical acoustic waves, which then propagate in the tissue. The key advantage of traveling-wave OCE is that analytical relationships between the elastic modulus and the acoustic wave velocity can be established. For example, in an infinite, isotropic, homogeneous, linear elastic material, the velocity of pure shear waves c_s is related to the shear elastic modulus μ by

$$c_s = \sqrt{\frac{\mu}{\rho}} \quad (2.25)$$

where ρ is the material density.

An important difficulty for ophtalmic applications is that virtually none of the abovementioned conditions are valid in the case of the cornea. More elaborate models must be used, which are valid under different circumstances depending on the sample geometry and frequency content of the stimulus waveform. Vibrations generated at the surface of a semi-infinite sample can be modeled as Rayleigh surface waves, and the shear elastic modulus μ can be obtained from the group velocity c_g , using $\mu \approx 0.95\rho c_g^2$. This formula is accurate only in a high-frequency limit in which the acoustic wavelength is much smaller than the corneal thickness. This model was

initially applied to the cornea [93, 191], but it was later recognized that the finite thickness and viscoelasticity of the cornea had to be considered through a Lamb wave (waveguide) model [59, 61].

Various contact and non-contact approaches are available to excite traveling waves in the cornea. Our group has recently used a contact probe actuated by a piezoelectric transducer [143], which is a simple and flexible way to generate acoustic waves, but implies a small level of discomfort for clinical applications. Small, focused air puffs (with much lower pressure than those used in tonometry) have been introduced and extensively used by the Larin group [191]. One limitation of this approach is that the bandwidth of air pulses is limited to a few hundreds of Hz, and thus the acoustic wavelengths are on the order of the size of the cornea itself, making the measurements subjects to artifacts from reflections at the cornea-sclera boundary and potentially reducing the contrast-to-noise ratio. Intense pulsed laser light can excite acoustic waves via the photo-acoustic effect [93]. Because of safety limitations, the photoacoustic signal in the eye is very weak, and dye-loaded nanodroplets have been recently proposed to enhance the optical to mechanical conversion efficiency [95]. Finally, the acoustic radiation force (ARF) generated by air-coupled ultrasounds has been used in corneal elastography, a promising non-contact approach that can provide a relatively wide frequency band [7].

Standing wave OCE

Standing wave OCE is based on modal analysis, with the rationale that for a given structure geometry, a stiffer material will cause a higher resonance frequency. A frequency-domain method using sound wave stimulus has been proposed, in which the vibrational modes of the cornea or the whole eye globe are analyzed by sweeping the acoustic frequency. Porcine eyes were found to have a fundamental resonance frequency of about 100 Hz [1]. However, this method is highly sensitive to boundary conditions (cornea-sclera junction), and elaborate numerical models are likely to be needed in order to quantitatively estimate the elastic modulus.

Applications of OCE in ophthalmology

Corneal biomechanics has been the major application area of OCE in ophthalmology. This is in part because cornea is readily accessible for the induction of a mechanical stimulus, but mostly because the mechanical properties of the cornea are involved in number of corneal ectasias (keratoconus being the most common). Biomechanics are also an important factor to consider in refractive surgeries (LASIK, PRK, etc.). However, the technology is still in its early stage and these applications have not directly been investigated.

Corneal cross-linking (CXL) is an emerging treatment to halt the progression of ectasia by crosslinking collagen fibrils and glycoproteins in the corneal stroma. OCE can measure the biomechanical changes induced by CXL, and compare the standard CXL procedure with novel ones [12, 50, 171, 172, 184].

OCE has also been proposed to characterize the mechanical properties of the sclera [173], the crystalline lens [196], and the retina [138, 139]. These applications are generally at the stage of *ex vivo* and animal experiments.

2.2 Elastic waves in solids

The section reviews the fundamentals of wave propagation in elastic solids, which form the basis of the elastography techniques described in the later chapters. The fundamental governing equations of linear elasticity and the propagation of waves in infinite solids are described in great details in classic textbooks on mechanical waves such as Refs. [2, 58]. They are presented here in condensed form to lay out the ground concepts and notations used in the following sections. Our main focus here is to describe elastic wave propagation in structures of finite thickness, which form the basis of our analysis of corneal biomechanics.

2.2.1 Fundamental equations of linear elasticity

Deformation of matter in a linear elastic solid is governed by two well known equations: Newton's second law and Hooke's law. When applied to infinitesimal elements of a continuum, the equation of motion (Newton's second law) can be written:

$$\nabla \cdot \boldsymbol{\sigma} + \mathbf{f} = \rho \frac{\partial^2 \mathbf{u}}{\partial t^2} \quad \text{or} \quad \sigma_{ji,j} + f_i = \rho \partial_{tt} u_i \quad (2.26)$$

where \mathbf{u} is the displacement vector, ρ is the volumetric mass density, $\boldsymbol{\sigma}$ is the stress tensor and \mathbf{f} is an external applied force per unit volume. This equation is shown in its vector, engineering form (left) and using Einstein's tensor notation (right).

A strain tensor $\boldsymbol{\varepsilon}$ is also defined, as a function of the displacement \mathbf{u} :

$$\boldsymbol{\varepsilon} = \frac{1}{2} [\nabla \mathbf{u} + (\nabla \mathbf{u})^T] \quad \text{or} \quad \varepsilon_{ij} = \frac{1}{2}(u_{j,i} + u_{i,j}) \quad (2.27)$$

The constitutive equation (Hooke's law), establishes a linear relationship between the stress tensor $\boldsymbol{\sigma}$ to the strain tensor $\boldsymbol{\varepsilon}$:

$$\boldsymbol{\sigma} = \mathbf{C} \cdot \boldsymbol{\varepsilon} \quad \text{or} \quad \sigma_{ij} = C_{ijkl} \varepsilon_{kl} \quad (2.28)$$

The stiffness tensor C_{ijkl} is the continuum equivalent of a spring constant. In the most general case, it is a fourth order tensor of 81 components, although only 21 of them are independent due to various symmetries in the definition of stress, strain and energy. For representation purposes, the tensor expression (2.28) can be conveniently converted to a 6×6 symmetric matrix using the convention $(xx, yy, zz, yz, xz, xy) \rightarrow (1, 2, 3, 4, 5, 6)$

(Voigt's notation):

$$\begin{bmatrix} \sigma_{xx} \\ \sigma_{yy} \\ \sigma_{zz} \\ \sigma_{yz} \\ \sigma_{xz} \\ \sigma_{xy} \end{bmatrix} = \begin{bmatrix} C_{11} & C_{12} & C_{13} & C_{14} & C_{15} & C_{16} \\ & C_{22} & C_{23} & C_{24} & C_{25} & C_{26} \\ & & C_{33} & C_{34} & C_{35} & C_{36} \\ & & & C_{44} & C_{45} & C_{46} \\ & \text{sym} & & & C_{55} & C_{56} \\ & & & & & C_{66} \end{bmatrix} \begin{bmatrix} \varepsilon_{xx} \\ \varepsilon_{yy} \\ \varepsilon_{zz} \\ 2\varepsilon_{yz} \\ 2\varepsilon_{xz} \\ 2\varepsilon_{xy} \end{bmatrix} \quad (2.29)$$

Isotropic materials

In case of an isotropic material – the highest possible symmetry – the number of independent components can be reduced down to 2: the shear modulus μ and Lamé's first parameter λ . The stiffness tensor is then:

$$C = \begin{bmatrix} \lambda + 2\mu & \lambda & \lambda & 0 & 0 & 0 \\ & \lambda + 2\mu & \lambda & 0 & 0 & 0 \\ & & \lambda + 2\mu & 0 & 0 & 0 \\ & & & \mu & 0 & 0 \\ & \text{sym} & & & \mu & 0 \\ & & & & & \mu \end{bmatrix} \quad (2.30)$$

and the stress-strain relation can be written

$$\sigma_{ij} = \lambda \delta_{ij} \varepsilon_{kk} + 2\mu \varepsilon_{ij} \quad (2.31)$$

The representation in terms of λ and μ is equivalent to using Young's modulus E and Poisson's ratio ν , and the two parametrization are related by:

$$\lambda = \frac{E\nu}{(1+\nu)(1-2\nu)}, \quad \mu = \frac{E}{2(1+\nu)} \quad (2.32)$$

Equations (2.26) to (2.28) can be combined into a single equation of motion expressed only in terms of the displacement vector \mathbf{u} . In the case of isotropic materials,

this equation is known as the Navier-Cauchy equation and takes the form:

$$\mu \nabla^2 \mathbf{u} + (\mu + \lambda) \nabla(\nabla \cdot \mathbf{u}) + \mathbf{f} = \rho \frac{\partial^2 \mathbf{u}}{\partial t^2}. \quad (2.33)$$

To solve the Navier-Cauchy equation, we can define a vector potential ψ and a scalar potential ϕ for the displacement field such that:

$$\mathbf{u} = \nabla\phi + \nabla \times \psi \quad (2.34)$$

The elastodynamic equation can then be separated in two decoupled wave equations:

$$\frac{\partial^2 \phi}{\partial t^2} = c_p^2 \nabla^2 \phi + \frac{\phi_f}{\rho}, \quad c_p = \sqrt{\frac{\lambda + 2\mu}{\rho}} \quad (2.35)$$

$$\frac{\partial^2 \psi}{\partial t^2} = c_s^2 \nabla^2 \psi + \frac{\psi_f}{\rho}, \quad c_s = \sqrt{\frac{\mu}{\rho}}, \quad (2.36)$$

where ϕ_f and ψ_f are the potentials associated with the volume force \mathbf{f} ($\mathbf{f} = \nabla\phi_f + \nabla \times \psi_f$).

Because of the elementary properties of the ∇ operator and of the wave equation, we can establish that the displacement field $u_p = \nabla\phi$ associated with the wave equation (2.35), describes a wave that is purely dilatational (zero curl) and that travels at velocity c_p . This wave is known as a compression wave or P-wave.

Equivalently, the displacement field $u_s = \nabla\psi$ associated with the wave equation (2.36), describes a wave that is purely distortional (zero divergence) and that travels at velocity c_s . This wave is known as a shear wave or S-wave.

An example of mechanical wave propagation in an infinite, linear elastic material is shown in Fig. 2-8. The response to a point-localized stimulus with a Gaussian temporal envelope was computed using the elastodynamic Green's function, which is obtained by solving equations (2.35)-(2.36). The details of this derivation can be found in chapter 4 of Aki's book [2]. Note that in order to enhance visualization, the ratio of S-wave to P-wave velocity was arbitrarily set to 2. In reality, P-waves can be more than 100 times faster than S-waves in soft biological tissues.

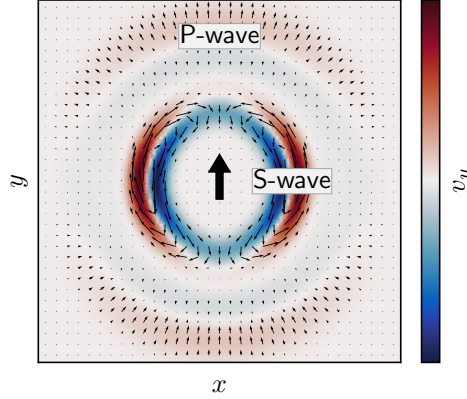


Figure 2-8: Mechanical wave propagation in an infinite, linear elastic medium, showing the axial velocity ($v_y = \partial u_y / \partial t$) in response to a point-localized force applied along the y axis (black arrow).

Anisotropic materials

If the material is anisotropic, equations (2.26) to (2.28) can still be combined into a single wave equation:

$$\rho \partial_{tt} u_i = C_{ijkl} u_{l,jk} \quad (2.37)$$

We consider solutions in the form of complex-valued plane waves

$$u_i = U_i e^{i(k_j x_j - \omega t)} = U_i e^{i(k \hat{k}_j x_j - \omega t)} \quad (2.38)$$

where k_i are the wavevector components, k is wavevector magnitude, \hat{k} is the unit-vector indicating the direction of propagation and ω is the angular frequency.²

$$\rho \omega^2 U_i = k^2 C_{ijkl} \hat{k}_j \hat{k}_l U_l \quad (2.39)$$

If we introduce the definition of phase velocity $c = \omega/k$, this equation can be rearranged as

$$(\Lambda_{il} - c^2 \delta_{il}) U_l = 0 \quad (2.40)$$

where $\Lambda_{il} = C_{ijkl} \hat{k}_j \hat{k}_k / \rho$. Equation (2.40) is the well known Christoffel equation,

²For lack of a cleaner notation, the upright i will be used throughout this section to denote the complex unit $i = \sqrt{-1}$, whereas the italic i will be used for the tensor index. This convention will be dropped in the other sections.

which describes the propagation of acoustic waves in anisotropic solids. It can be recognized as an eigenvalue problem where the phase velocity c is the eigenvalue and U_i is the eigenvector. Given that Λ_{il} is a 3×3 rank-2 tensor, this equation defines 3 modes of propagation with distinct wave velocities, each of which is a function of the propagation direction \hat{k}_j .

As should be expected, this result includes the isotropic case, where the 3 modes are simply the compression wave and two orthogonally polarized shear waves. In anisotropic materials, the modes are not purely dilatational (zero curl) or purely distortional (zero divergence), but they often closely resemble compression and shear waves. They are then known as quasi-compression-wave, and quasi-shear-waves.

2.2.2 Guided waves in plates

We now consider the problem of elastic wave propagation in plates, in particular when one side of the plate is bounded by fluid and the other one is free. The geometry of the problem is shown in Fig. 2-9. The solid plate has a finite thickness h along the z axis and is bounded by semi-infinite spaces at the bottom (fluid) and top (vacuum). The plate extends infinitely in the x and y directions.

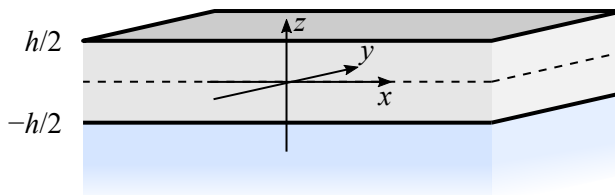


Figure 2-9: Geometry and variable definitions for the fluid-plate-vacuum system.

This problem is a classic boundary-conditions problem. The key solution steps are: (1) solving the equations of motion in each layer separately, (2) applying the appropriate boundary conditions at each interface, (3) solving the resulting system of equations. The theoretical developments and notations closely follow those used in Nayfeh's book [120].

Solution to the equations of motion in solids

We will seek solutions to the wave equation in the form of plane harmonic waves. Without loss of generality, we can choose our axes definitions such that the wave propagation directions are confined to the $x - z$ plane, and thus find solutions that are independent of y . These solution take the form

$$u_j = U_j e^{i\xi(x+\alpha z-ct)} \quad (2.41)$$

For convenience in the following developments, the wavevector components $\mathbf{k} = (k_x, k_y, k_z)$ are expressed in the alternate form $\mathbf{k} = (\xi, 0, \alpha\xi)$, such that ξ is the effective propagation constant of the waveguide (x component of the wavevector) and α is a the ratio of the x and z wavevectors components. The velocity c is the effective phase velocity of the wave traveling along x , and therefore ξ and c are related by $\omega = c\xi$. This leaves us with two unknowns to solve for: the phase velocity c and the normalized propagation constant α .

Substituting this form of solution in the stress-strain relation (2.28) and making use of the strain-displacement definition (2.27), we obtain the stresses associated with the assumed displacement:

$$\begin{aligned} \sigma_{xx} &= i\xi (U_x (\alpha C_{15} + C_{11}) + U_y (\alpha C_{14} + C_{16}) + U_z (\alpha C_{13} + C_{15})) e^{i\xi(x+\alpha z-ct)} \\ \sigma_{yy} &= i\xi (U_x (\alpha C_{25} + C_{12}) + U_y (\alpha C_{24} + C_{26}) + U_z (\alpha C_{23} + C_{25})) e^{i\xi(x+\alpha z-ct)} \\ \sigma_{zz} &= i\xi (U_x (\alpha C_{35} + C_{13}) + U_y (\alpha C_{34} + C_{36}) + U_z (\alpha C_{33} + C_{35})) e^{i\xi(x+\alpha z-ct)} \\ \sigma_{yz} &= i\xi (U_x (\alpha C_{45} + C_{14}) + U_y (\alpha C_{44} + C_{46}) + U_z (\alpha C_{34} + C_{45})) e^{i\xi(x+\alpha z-ct)} \\ \sigma_{xz} &= i\xi (U_x (\alpha C_{55} + C_{15}) + U_y (\alpha C_{45} + C_{56}) + U_z (\alpha C_{35} + C_{55})) e^{i\xi(x+\alpha z-ct)} \\ \sigma_{xy} &= i\xi (U_x (\alpha C_{56} + C_{16}) + U_y (\alpha C_{46} + C_{66}) + U_z (\alpha C_{36} + C_{56})) e^{i\xi(x+\alpha z-ct)} \end{aligned} \quad (2.42)$$

Note that because the boundaries are parallel to the x - y plane (their normal pointing in the z direction), only the stresses σ_{zz} , σ_{yz} and σ_{xz} are involved in the expression of the boundary conditions. It is therefore useful to reexpress the displacement-stress

equations (2.42) in the convenient format:

$$\begin{bmatrix} \sigma_{zz} \\ \sigma_{yz} \\ \sigma_{xz} \end{bmatrix} = i \xi \mathbf{P} \begin{bmatrix} U_x \\ U_y \\ U_z \end{bmatrix} e^{i\xi(x+\alpha z - ct)}, \quad (2.43)$$

$$\mathbf{P} = \begin{bmatrix} \alpha C_{35} + C_{13} & \alpha C_{34} + C_{36} & \alpha C_{33} + C_{35} \\ \alpha C_{45} + C_{14} & \alpha C_{44} + C_{46} & \alpha C_{34} + C_{45} \\ \alpha C_{55} + C_{15} & \alpha C_{45} + C_{56} & \alpha C_{35} + C_{55} \end{bmatrix} \quad (2.44)$$

Where the \mathbf{P} matrix and its inverse can be used to convert between stresses and displacements.

Substituting these expressions in the equation of motion (2.26) leads to an alternative form of Christoffel's equation:

$$K_{ij}(\alpha, c) U_j = 0 \quad (2.45)$$

where K_{ij} is symmetric and its components are:

$$\begin{aligned} K_{11} &= \alpha^2 C_{55} + 2\alpha C_{15} + C_{11} - \rho c^2 \\ K_{12} &= \alpha^2 C_{45} + \alpha(C_{14} + C_{56}) + C_{16} \\ K_{13} &= \alpha^2 C_{35} + \alpha(C_{13} + C_{55}) + C_{15} \\ K_{22} &= \alpha^2 C_{44} + 2\alpha C_{46} + C_{66} - \rho c^2 \\ K_{23} &= \alpha^2 C_{34} + \alpha(C_{36} + C_{45}) + C_{56} \\ K_{33} &= \alpha^2 C_{33} + 2\alpha C_{35} + C_{55} - \rho c^2 \end{aligned} \quad (2.46)$$

For non-trivial solutions to exist, the determinant of K_{ij} must be zero. This results in a polynomial of degree 6 that has 6 roots, each of which corresponds to a mode of propagation in the bulk medium. We will use the index $q = 1, 2, \dots, 6$ to label each of those modes. Note that plane wave form of solution gives rise to 6 instead of 3 modes, because it explicitly distinguishes upward traveling waves from downward

traveling waves, thus there is no contradiction with the 3 bulk modes encountered previously. Once the eigenvalues α_q are found, the eigenvectors U_{jq} can be found by direct substitution in Eq. (2.45). We express these solutions normalized to the x component of the displacement vector such that $\mathbf{U}_q = A_q(1, V_q, W_q)$:

$$A_q = U_{xq} \quad (2.47)$$

$$V_q = \frac{U_{yq}}{U_{xq}} = \frac{K_{12}(\alpha_q)K_{13}(\alpha_q) - K_{11}(\alpha_q)K_{23}(\alpha_q)}{K_{12}(\alpha_q)K_{23}(\alpha_q) - K_{13}(\alpha_q)K_{22}(\alpha_q)} \quad (2.48)$$

$$W_q = \frac{U_{zq}}{U_{xq}} = \frac{K_{12}(\alpha_q)K_{13}(\alpha_q) - K_{11}(\alpha_q)K_{23}(\alpha_q)}{K_{13}(\alpha_q)K_{23}(\alpha_q) - K_{12}(\alpha_q)K_{33}(\alpha_q)} \quad (2.49)$$

The coefficients A_q then represent the complex-valued amplitude of each mode. The complete plane-wave solution to the equation of motion is given by a superposition of these 6 modes. The formal solutions for the displacements and stresses are then given by

$$(u_x, u_y, u_z) = \sum_{q=1}^6 A_q(1, V_q, W_q) e^{i\xi(x + \alpha_q z - ct)} \quad (2.50)$$

$$(\sigma_{zz}, \sigma_{yz}, \sigma_{xz}) = \sum_{q=1}^6 i\xi A_q(D_{1q}, D_{2q}, D_{3q}) e^{i\xi(x + \alpha_q z - ct)} \quad (2.51)$$

where the displacement-stress conversion matrix \mathbf{P} defined in equation 2.44 is used to obtain the normalized stress components of each mode

$$\mathbf{D}_q = \mathbf{P}(1, V_q, W_q)^T \quad (2.52)$$

Note that at this point in the development, for a given α_q , the values of V_q , W_q , D_{1q} , D_{2q} , D_{3q} are fully defined. However each of the mode amplitudes A_q are unknowns to be found by applying the boundary conditions.

Solution to the equations of motion in liquids

The differential form of Newton's second law (2.26) is valid for any continuous material, including liquids. Non-viscous fluids do not support shear forces, and their constitutive

(stress-deformation) equation can be obtained from that of an isotropic solid where the shear modulus $\mu = 0$:

$$\boldsymbol{\sigma} = \lambda_f(\nabla \cdot \mathbf{u}) \boldsymbol{\delta} \quad \text{or} \quad \sigma_{ij} = \lambda_f u_{k,k} \delta_{ij} \quad (2.53)$$

where λ_f is the Lamé constant of the fluid and $\boldsymbol{\delta}$ is the identity tensor (Kronecker delta). The solution can be expressed in terms of potentials, where only the scalar potential ϕ is non-zero, resulting in a single, scalar wave equation. The bulk wave velocity is $c_f = \sqrt{\lambda_f/\rho_f}$ where ρ_f is the density of the fluid. Expressing the solution in the same form as (2.41), we get:

$$u_{f,jq} = U_{f,jq} e^{i\xi(x + \alpha_{f,q} z - ct)} \quad (2.54)$$

where $q = 1, 2$ are the only two valid modes (upward and downward compression wave), and where the α_q and amplitude coefficients can be found by substituting in the wave equation or by simple geometric arguments:

$$\alpha_{f,1}, \alpha_{f,2} = \pm \alpha_f = \pm \sqrt{c^2/c_f^2 - 1} \quad (2.55)$$

$$V_{f,q} = \frac{U_{f,yq}}{U_{f,xq}} = 0 \quad (2.56)$$

$$W_{f,q} = \frac{U_{f,zq}}{U_{f,xq}} = \alpha_{f,q} \quad (2.57)$$

Finally, the stress σ_{zz} can be found by substitution into (2.53) and using the definition of c_f :

$$\sigma_{f,zzq} = i\xi \rho_f c^2 U_{f,xq} \quad (2.58)$$

The formal solutions for the displacements and stresses in a fluid layer are given by:

$$(u_x, u_y, u_z)_f = \sum_{q=1}^2 A_{f,q}(1, 0, W_{f,q}) e^{i\xi(x + \alpha_{f,q} z - ct)} \quad (2.59)$$

$$(\sigma_{zz}, \sigma_{yz}, \sigma_{xz})_f = \sum_{q=1}^2 i\xi A_{f,q}(i\xi \rho_f c^2, 0, 0) e^{i\xi(x + \alpha_{f,q} z - ct)} \quad (2.60)$$

Boundary conditions

The boundary conditions depend on the nature of the media on each side of the interface. At a bonded solid-solid interface, the displacement vector and the stress components are continuous. At a solid-fluid interface, the normal displacement u_z and normal stress σ_{zz} must be continuous, but the tangential displacements u_x, u_y are unconstrained and the shear stresses σ_{zx}, σ_{zy} are zero. At a solid-vacuum interface, the displacements are free, and both shear and normal stresses must be zero. These boundary conditions are summarized in Table 2.1.

Table 2.1: Boundary conditions in linear elastodynamics for solid-solid, solid-fluid, and solid-vacuum interfaces.

Boundary type	Displacements			Stresses		
	u_x	u_y	u_z	σ_{zz}	σ_{yz}	σ_{xz}
Solid-vacuum	free	free	free	0	0	0
Solid-fluid	free	free	=	=	0	0
Solid-solid	=	=	=	=	=	=

We evaluate the displacement and stresses given by Eq. 2.50 and (2.51 at $z = h/2$ and $z = -h/2$ for the solid, and $z = -h/2$ for the fluid, and call upon the boundary conditions defined in Table 2.1. This defines a system of 7 equations and 8 unknowns: the amplitude coefficients A_q and $A_{f,q}$. In the semi-infinite spaces, only the wave components traveling away from the plate are allowed. This sets one of the coefficients in the fluid layer to zero, resulting in a homogeneous system of 7 equations and 7 unknowns:

$$\mathbf{M}\mathbf{A} = \mathbf{0} \quad (2.61)$$

where

$$\mathbf{A} = [A_1, A_2, A_3, A_4, A_5, A_6, A_{f,2}]^T \quad (2.62)$$

$$\mathbf{M} = \begin{bmatrix} g_1^* W_1 & g_2^* W_2 & g_3^* W_3 & g_4^* W_4 & g_5^* W_5 & g_6^* W_6 & g_f \alpha_F \\ i\xi g_1^* D_{11} & i\xi g_2^* D_{12} & i\xi g_3^* D_{13} & i\xi g_4^* D_{14} & i\xi g_5^* D_{15} & i\xi g_6^* D_{16} & -i\xi c^2 g_f \rho_F \\ i\xi g_1^* D_{21} & i\xi g_2^* D_{22} & i\xi g_3^* D_{23} & i\xi g_4^* D_{24} & i\xi g_5^* D_{25} & i\xi g_6^* D_{26} & 0 \\ i\xi g_1^* D_{31} & i\xi g_2^* D_{32} & i\xi g_3^* D_{33} & i\xi g_4^* D_{34} & i\xi g_5^* D_{35} & i\xi g_6^* D_{36} & 0 \\ i\xi g_1 D_{11} & i\xi g_2 D_{12} & i\xi g_3 D_{13} & i\xi g_4 D_{14} & i\xi g_5 D_{15} & i\xi g_6 D_{16} & 0 \\ i\xi g_1 D_{21} & i\xi g_2 D_{22} & i\xi g_3 D_{23} & i\xi g_4 D_{24} & i\xi g_5 D_{25} & i\xi g_6 D_{26} & 0 \\ i\xi g_1 D_{31} & i\xi g_2 D_{32} & i\xi g_3 D_{33} & i\xi g_4 D_{34} & i\xi g_5 D_{35} & i\xi g_6 D_{36} & 0 \end{bmatrix} \quad (2.63)$$

and where we used the shorthand notation $g_q = e^{\frac{1}{2}ih\xi\alpha_q}$, $g_q^* = e^{-\frac{1}{2}ih\xi\alpha_q}$, and $g_f = e^{\frac{1}{2}ih\xi\alpha_f}$.

The elements of D_{jq} are defined by Eq. (2.52).

For the homogeneous system (2.61) to allow for non-trivial solution, the determinant of \mathbf{M} must vanish, giving the characteristic equation:

$$|\mathbf{M}| = 0 \quad (2.64)$$

The independent variables of the characteristic equation can appear somewhat buried under abundant notation shortcuts, and it is worth pausing here to highlight its meaning. Equation (2.64) is an implicit equation defining a relationship between two variables: the effective phase velocity c and the propagation constant ξ . Since the propagation constant ξ and frequency f are related by $\omega = 2\pi f = c\xi$, it can equivalently be seen as an implicit relationship between frequency and phase velocity. All other parameters (D_{jq} , V_q , W_q , α_q , etc.) are ultimately functions of c and of the known material properties (stiffness tensor C_{ijkl} , densities ρ , etc.). The solution strategy is then to fix either c or f (typically f) and vary the other (typically c) to make $|\mathbf{M}| = 0$. Note that for a given f , there may be multiple solutions: the modes of the plate.

Special case: transversely isotropic plate

Equation 2.64 derived in the previous section can be used to calculate the modes of propagation in linear elastic plates of arbitrary class of anisotropy. Transversely isotropic materials are commonly used in modeling layered fibrous composite materials, can represent the cornea and other collagen-rich biomaterials to a good level of accuracy. It is therefore worth further developing the model for this class of materials. The solution developed here will also fully encompass that of higher symmetry materials, such as isotropic.

The stiffness tensor for transversely isotropic media is fully defined by 5 independent parameters and is given by:

$$\mathbf{C} = \begin{bmatrix} C_{11} & C_{11} - 2C_{66} & C_{13} & 0 & 0 & 0 \\ C_{11} - 2C_{66} & C_{11} & C_{13} & 0 & 0 & 0 \\ C_{13} & C_{13} & C_{33} & 0 & 0 & 0 \\ 0 & 0 & 0 & C_{44} & 0 & 0 \\ 0 & 0 & 0 & 0 & C_{44} & 0 \\ 0 & 0 & 0 & 0 & 0 & C_{66} \end{bmatrix} \quad (2.65)$$

It can be shown that the equation of motion for such material can be separated into two independent components. If we still consider the wave direction propagation to be in the x - z plane, waves that have their displacement vectors purely along the y axis are known as shear-horizontal (SH) waves, and waves that have their displacement vector in the sagittal x - z plane are a combination of shear-vertical (SV) and compression (P) waves.

We will focus our attention on sagittal-plane motion which represents the propagation of flexural waves that can be excited by a transverse loading force. In this case,

the formal solutions for displacements and stresses take the form:

$$(u_x, u_y, u_z) = \sum_{q=1}^4 A_q(1, 0, W_q) e^{i\xi(x + \alpha_q z - ct)} \quad (2.66)$$

$$(\sigma_{zz}, \sigma_{yz}, \sigma_{xz}) = \sum_{q=1}^4 i\xi A_q(D_{1q}, 0, D_{3q}) e^{i\xi(x + \alpha_q z - ct)} \quad (2.67)$$

And the normalized displacements and stresses are:

$$W_q = \frac{\rho c^2 - C_{11} - C_{44}\alpha_q^2}{(C_{13} + C_{44})\alpha_q} \quad (2.68)$$

$$D_{1q} = C_{13} + C_{33}W_q\alpha_q \quad (2.69)$$

$$D_{3q} = C_{44}(\alpha_q + W_q) \quad (2.70)$$

The normalized propagation constant α_q now satisfies a quadratic equation in α^2 ($a\alpha^4 + b\alpha^2 + c = 0$) which, contrarily to the arbitrary polynomial of degree 6 encountered earlier, can be solved analytically. The solutions are:

$$\alpha_1 = -\alpha_2 = \sqrt{\frac{-b + \sqrt{b^2 - 4ac}}{2a}} \quad (2.71)$$

$$\alpha_3 = -\alpha_4 = \sqrt{\frac{-b - \sqrt{b^2 - 4ac}}{2a}} \quad (2.72)$$

where the polynomial coefficients are given by:

$$a = C_{33}C_{44} \quad (2.73)$$

$$b = -\rho c^2 C_{44} + C_{33} (C_{11} - \rho c^2) - C_{13}^2 - 2C_{13}C_{44} \quad (2.74)$$

$$c = (\rho c^2 - C_{11}) (\rho c^2 - C_{44}) \quad (2.75)$$

The system matrix \mathbf{M} is obtained by rejecting the rows and columns associated with

y-axis motion:

$$\mathbf{A} = [A_1, A_2, A_3, A_4, A_{f,2}]^T \quad (2.76)$$

$$\mathbf{M} = \begin{bmatrix} g_1^*W_1 & g_2^*W_2 & g_3^*W_3 & g_4^*W_4 & g_f\alpha_F \\ i\xi g_1^*D_{11} & i\xi g_2^*D_{12} & i\xi g_3^*D_{13} & i\xi g_4^*D_{14} & -i\xi c^2 g_f \rho_F \\ i\xi g_1^*D_{31} & i\xi g_2^*D_{32} & i\xi g_3^*D_{33} & i\xi g_4^*D_{34} & 0 \\ i\xi g_1 D_{11} & i\xi g_2 D_{12} & i\xi g_3 D_{13} & i\xi g_4 D_{14} & 0 \\ i\xi g_1 D_{31} & i\xi g_2 D_{32} & i\xi g_3 D_{33} & i\xi g_4 D_{34} & 0 \end{bmatrix} \quad (2.77)$$

Given the simplified definition of α_q , the determinant of \mathbf{M} can be expressed in closed form by using a series of row and column operations (not shown here). The characteristic equation is then written as:

$$AS + iY(A - S)/2 = 0 \quad (2.78)$$

The coefficients A, S, Y are implicit functions of c and $\gamma = \xi h/2 = \pi f h/c$, thereby defining an implicit relationship between c and f , just as in the general solution. They are defined by

$$S = D_{11}D_{33} \cot(\gamma\alpha_1) - D_{13}D_{31} \cot(\gamma\alpha_3) \quad (2.79)$$

$$A = D_{11}D_{33} \tan(\gamma\alpha_1) - D_{13}D_{31} \tan(\gamma\alpha_3) \quad (2.80)$$

$$Y = \frac{\rho_f c^2}{\alpha_f} (W_3 D_{31} - W_1 D_{33}) \quad (2.81)$$

The functions A and S sub-determinants arising in the traditional study of elastic waves in a free plate (not supported by fluid), and which, when set to zero, give rise to purely symmetric (S) and antisymmetric (A) modes known as Lamb waves. The effect of fluid is entirely contained in the variable Y . We can note that the portion of equation (2.78) describing fluid-loading effect is imaginary. This implies that the modes of the plate will either be lossy (energy is lost into traveling waves in the fluid) or that the wave in the fluid will be evanescent.

Importantly, note that wave propagation in the sagittal plane is independent of

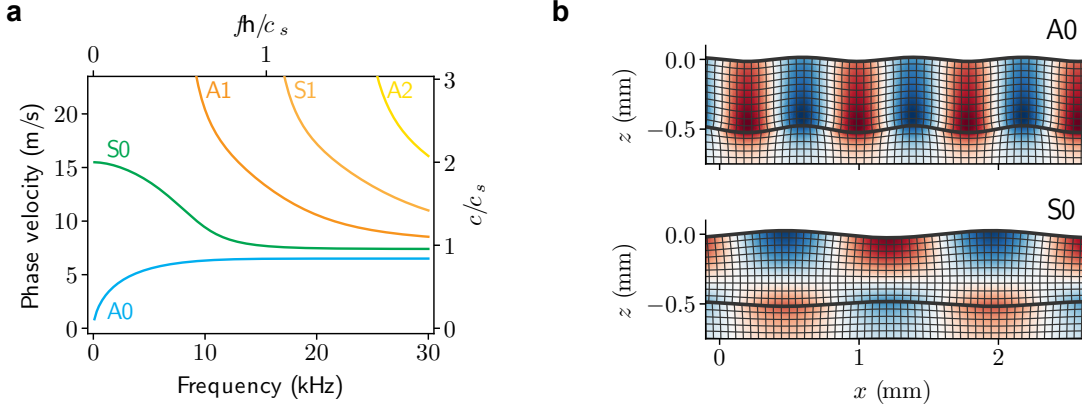


Figure 2-10: Example wave velocities (a) and mode shapes (b) for a plate with $C_{44} = 60 \text{ kPa}$, $C_{13} = 2 \text{ GPa}$, and $C_{11} = C_{33} = 2.0002 \text{ GPa}$.

the modulus C_{66} , which governs the propagation of SH waves and is related to the in-plane tensile stiffness.

Also note that although we have succeeded in expressing the characteristic equation in terms of elementary and trigonometric functions, it is still a transcendental equation that cannot be solved by purely analytical means. Roots of Eq. (2.78) must still ultimately be found using a computerized root-finding algorithm. A good approach is to use the slow but robust bisection method to find the first few roots, and then use them as initial guesses for a faster but less stable gradient-based solver, as has been described in Ref. [98].

Figure 2-10 illustrates a typical spectrum and mode shapes for a transversely isotropic plate between fluid and vacuum. For representation purposes, we have used elastic modulus values close to those expected in a human cornea. The spectrum exhibits the characteristic features of classical Lamb waves. It is composed of a discrete infinity of modes, which are classified as either quasi-symmetric (S_n modes) or quasi anti-symmetric (A_n modes), by analogy to the free plate problem. The deformation in the plate and fluid associated with the A_0 and S_0 modes are shown in Fig. 2-10.b for a frequency of $f = c_s/2h$ where c_s is the speed of pure SV shear waves. It is evident from this representation the when the plate is bounded by fluid, the modes are not purely symmetric or antisymmetric, but they retain the overall expected shape. Also note that zero-order modes are always present regardless of the frequency, and higher

order modes cut off around integer multiples of $fh/2c_s$

2.3 Middle ear imaging and vibrometry

The basic anatomy of the ear is shown in Fig. 2-11. Soundwaves first enter the ear through the auditory canal, at the end of which lies the tympanic membrane (TM), or eardrum. The varying sound pressure applies a force on the TM, setting it into motion. A series of small bones, the ossicles, are located behind the eardrum, in a space called the middle ear cavity. They form a chain that transmits the vibration from the eardrum to the cochlea, a fluid-filled, spiral-shaped organ where mechanical vibrations are converted into nervous impulse.

There are 3 ossicles: malleus, incus and stapes. They play an important role in hearing by maximizing the amount of acoustic energy that can be transmitted from the air-filled ear canal and the fluid-filled inner ear. In other words, they form an acoustic impedance-matching system [118].

Because the intrinsic function of the middle ear is to conduct sound vibrations, there is a natural interest in measuring and quantifying its vibratory behavior. As such, OCT vibrography has the potential to become an important tool in the field of otology and hearing research, because it provides the means to simultaneously

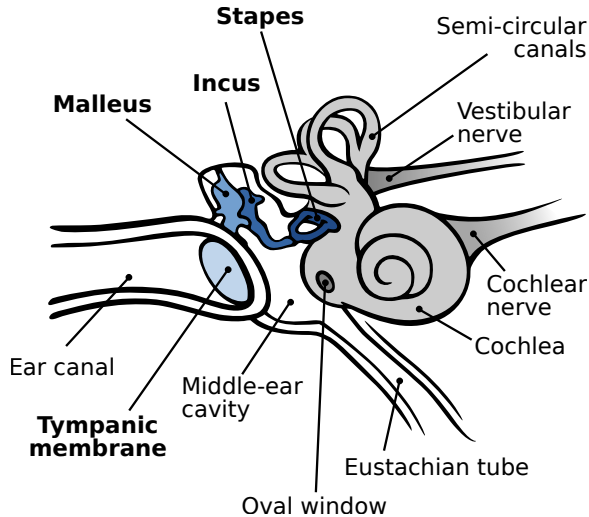


Figure 2-11: Anatomy of the middle and inner ear.

measure the structure and function of the hearing organ. Moreover, it can do so with a combination of resolution and sensitivity that is unmatched by existing technologies. The remainder of this section will review the existing literature on OCT imaging of the middle ear. We will then focus specifically on vibration measurements.

2.3.1 Imaging the middle ear with OCT

Pitris and coworkers were among the first who proposed OCT for middle ear imaging in 2001 [135], using time-domain OCT to image the middle ear cavity through intact tympanic membrane in human temporal bones. Other groups have followed-up with explorations of potential intraoperative applications, such as evaluating stapes fixation and determining the appropriate geometry of middle-ear prostheses [63, 72–74]. A number of the early studies have also been interested in the diagnosis potential of OCT for middle ear disorders. Prospective studies identified features of pathological conditions such as dimeric tympanic membrane, tympanosclerosis, cholesteatoma, granulation tissue from a perforation and hyperkeratosis [33, 34]. However, these initial explorations did not establish a clear clinical benefit from the information provided by OCT, and there has only been minimal follow-up on these application candidates.

More recent work has focused on otitis media diagnosis, characterization and management. Handheld otoscope-style probes were developed to be deployed in a primary care setting [195], and used to detect and quantify tympanic membrane biofilm [122]. These studies showed significant differences between healthy, chronic and acute otitis media cases [117], and an interesting potential to quantify the viscosity of middle ear effusions [116]. This application is in its early stage of commercialization (TOMiTM, PhotoniCare Inc.), but is still generally considered experimental and investigational.

From a technologist's perspective, OCT systems used for middle ear imaging were generally conventional spectral domain and time domain OCT systems, with the exception of a Burkhardt and co-workers who reported the use of a high-resolution, dual-band spectral-domain OCT [19]. In general, technological innovations for middle ear

imaging focused on the imaging arm optics. Several groups developed otoscopic handheld systems [132, 195], or mounted the OCT system on surgical microscope [71, 100]. Narrow endoscopic probes based on GRIN optics were also reported [20, 133].

2.3.2 Vibrometry of the auditory system

Traditional methods to measure middle and inner ear vibrations include stroboscopic microscopy, capacitive probes and the Mössbauer technique [70, 126, 158, 188]. Over the last decades, these methods have been largely superseded in terms of sensitivity, speed and convenience by optical interferometric approaches, particularly laser Doppler vibrometry [29, 78, 148, 183]. However, LDV and the other approaches are limited to surface measurements, and typically require the positioning of exogenous probes on the structure to be measured. Interferometric methods are also subject to artefacts caused by other vibrating structures located below the tissue of interest if those lower tissues are sufficiently reflective [30]. Consequently, all methods require invasive, artifact-inducing surgery to access structures deeper than the tympanic membrane or beneath the cochlear bone [125, 153, 157].

Phase-sensitive optical coherence tomography (PhS-OCT) can solve the limitations of existing methods, because it acts simultaneously a vibrometer with sub-nanometer sensitivity [23, 189] and a high-speed, high-resolution imaging modality that penetrates a few millimeters deep inside biological tissues [38]. The proposition of using OCT for measuring vibrations of the tympanic membrane and ossicular chain is relatively recent. Applegate measured the mouse tympanic membrane vibrations in 2011, but the demonstration was mostly as a proof of concept for a technological innovation (coherent interleaving) [11]. Burkhardt and coworkers realized a more detailed study of tympanic membrane motion at different location and frequencies [18], their findings matching those obtained by holography [25]. In 2012, Subhash performed the first OCT vibrometry measurements on the ossicular chain [181]. Measurements were made on ex-vivo human temporal bone, and the malleus, incus and stapes footplate were clearly visible even when imaging through the tympanic membrane, which resulted in vibrational images of good quality.

Our group performed 3D vibrometric measurements of the middle ear ossicles in a chinchilla model [22]. This study conducted by Chang *et al.* measured the motion of the a large part of middle ear cavity at different frequencies. Visualization of the results was enhanced by 3D animations of the segmented ossicular chain with magnified motion. The researchers also found characteristic phase and amplitude response of the ossicles in simulated pathological conditions (stapes fixation and incus-stapes joint interruption), suggesting interesting potential for clinical diagnosis and management of ossicular disorders.

Possible clinical applications of middle ear vibrometry have also been investigated in a number of studies. Kirsten observed the motion of the tympanic membrane during a simulated Eustachian catarrh [81]. The study performed on human temporal bones revealed variations in the spatial profile of vibration amplitude. The same group used structural and vibrometric OCT to detect fluid in the middle ear, with the intention of characterizing middle ear effusions in the setting of otitis media [80]. Structural OCT images were sufficient to identify scattering fluids, whereas reduced vibration amplitude helped detect the presence non-scattering fluids.

Recent work by Park *et al.* [132] and MacDougall *et al.* [100] have started to address the engineering challenges of performing similar vibrometric measurements in live patients. Both teams designed imaging probes suitable for clinical measurements (hand-held or mounted on a surgical microscope) and demonstrated their devices on ex-vivo samples. The team led by MacDougall has now performed *in vivo* OCT vibrometry measurements in humans, and started studying the diagnosis potential for ossicular disorders [101].

2.4 Cornea biomechanics

The cornea is the dome-shaped, transparent window that forms the most anterior part of the eye (Fig. 2-12.a). It is the point of entry of light into the eyeglobe, and as such, plays a critical role in visual acuity. Due to the high contrast of refractive index between air and tissues, the cornea is responsible for the largest part of the eye's total

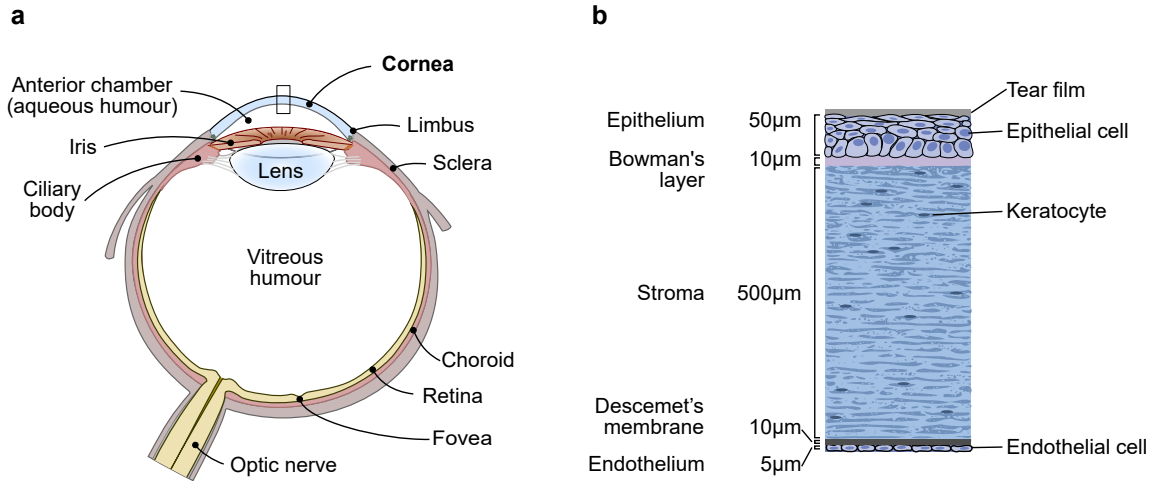


Figure 2-12: Corneal anatomy and histology. (a) Main anatomical structure of the eye globe. (b) Cross-sectional view of the cornea, showing the main layers, their approximate thickness in an adult human, and their main cellular components.

refractive power – about 70 %, the remainder being provided by the crystalline lens.

In order to focus a sharp image on the retina, the cornea must maintain a smooth surface, which is accomplished in part by maintaining the eyeglobe at positive pressure with respect to the atmosphere (the intraocular pressure or IOP) by about 15 mmHg. The cornea must then maintain a precise aspherical shape within tight geometric tolerances, a tour de force that relies largely on the mechanical properties of the corneal tissues. The cornea must be flexible enough to bulge out from IOP, but also sufficiently tough to sustain the load over time, and provide a mechanical protection against injuries. The study of corneal biomechanics therefore holds great promise to improve our understanding of corneal physiology and pathology, and could open up new avenues for diagnosis and therapies.

2.4.1 Corneal anatomy and histology

A typical human cornea is about 550 µm thick and is comprised of 5 layers: the epithelium, Bowman's layer, the corneal stroma, Descemet's membrane, and the endothelium, which are illustrated in Fig. 2-12.b. Its main cellular components are the epithelial cells, stromal keratocytes, and endothelial cells. It is also a densely innervated tissue, and immune cells such as dendritic cells and macrophages sparsely

populate the corneal stroma and epithelium.

The cornea anterior surface is covered by a stratified squamous non-keratinizing epithelium, about 50 µm thick and composed of about 4 to 6 layers of cells. It mainly functions as a low-permeability barrier that prevents the loss of fluids and protects against pathogens.

Bowman's layer is an acellular region composed of interwoven, randomly oriented collagen fibers. It is not consistently present across mammalian species, and its exact role remains uncertain, but it is thought to play a biomechanical role in maintaining the corneal shape by providing attachment points for collagen fibers of the stroma [108].

The corneal stroma, occupying about 90 % of the total thickness, is the structure that gives the cornea the bulk of its mechanical strength. It is composed of about 250 layers (lamellae) of a dense and highly structured network of collagen fibers (predominantly type I and V), which bathe in a gel-like matrix of water, proteoglycans and other molecules. Keratocytes, a specialized form of fibroblasts, sparsely populate the interlamellar space and are responsible for maintaining the extracellular matrix by producing collagen molecules and proteoglycans. They also play important roles in tissue repair and wound healing. The relative weights of the different constituents are summarized in Table 2.2.

Table 2.2: Relative weight of the different cornea components [92].

Component	Wet weight (%)	Dry weight (%)
Water	78	—
Matrix	66	
Intracellular	12	
Dry components	22	
Collagen	15	71
Proteoglycans	1	9
Keratocytes	1	10
Other	5	10

Descemet's membrane is the basement membrane of the corneal endothelium. It forms a 5-15 µm thick layer, rich in collagen (types IV and VIII) and proteoglycans. It is arranged in an hexagonal lattice, and is mechanically extensible and tough. It

serves mostly as an attachment layer between the endothelial cells and the posterior stroma.

Finally, the endothelium forms the posterior layer of the cornea. Its core function is the active and passive transport of water, ions and nutrients between the cornea and the aqueous humor. It maintains the cornea in a slightly hyperosmotic state which is important for corneal transparency.

2.4.2 Collagen structure and organization

Collagen is the most abundant protein in mammals. It is the biomechanical workhorse of multiple types of connective and supportive tissues including skin, tendon, ligaments, bone, and indeed the cornea [51]. There are 28 known types of collagen, about half of which are present in the human cornea, although type I (58 %), type V (15 %) and type VI (24 %) are by far the most common [92, 109, 151].

Single collagen molecules, or tropocollagen, are a combination of 3 α -peptides assembled in a triple helix, stabilized by numerous hydrogen bonds (Fig. 2-13.A). Tropocollagen molecules measure about 300 nm in length and 1.5 nm in diameter. The half-life of type I collagen in human cornea is not known, but in other tissues it varies between 45 and 244 days [108]. It is thus slowly resynthesized by keratocytes.

Tropocollagen assembles in the form of fibrils (Fig. 2-13.B). Fibrils are about 30 to 35 nm in diameter³, with about 250 molecules per cross-section [110]. Molecules are assembled in a staggered way, with an axial periodicity of 65 nm. An enzyme called lysyl oxidase catalyzes the formation of covalent bonds between and within collagen molecules. Those cross-links are initially divalent, and later spontaneously transform to a trivalent (mature) bond. The concentration of mature cross-link is stable with age. However, spontaneous, non-enzymatic cross-links (intramolecular, intermolecular and interfibrillar) tend to accumulate over time, resulting in stiffer, stronger, although less extensible fibrils (Fig. 2-13.C) [92].

³On Fig. 2-14, collagen fibrils are shown to have a diameter of 25 nm. This value is based on TEM measurements, which suffer from shrinkage due to preprocessing. The value of 31 nm obtained from x-ray diffraction is generally considered more representative of the *in vivo* arrangement.

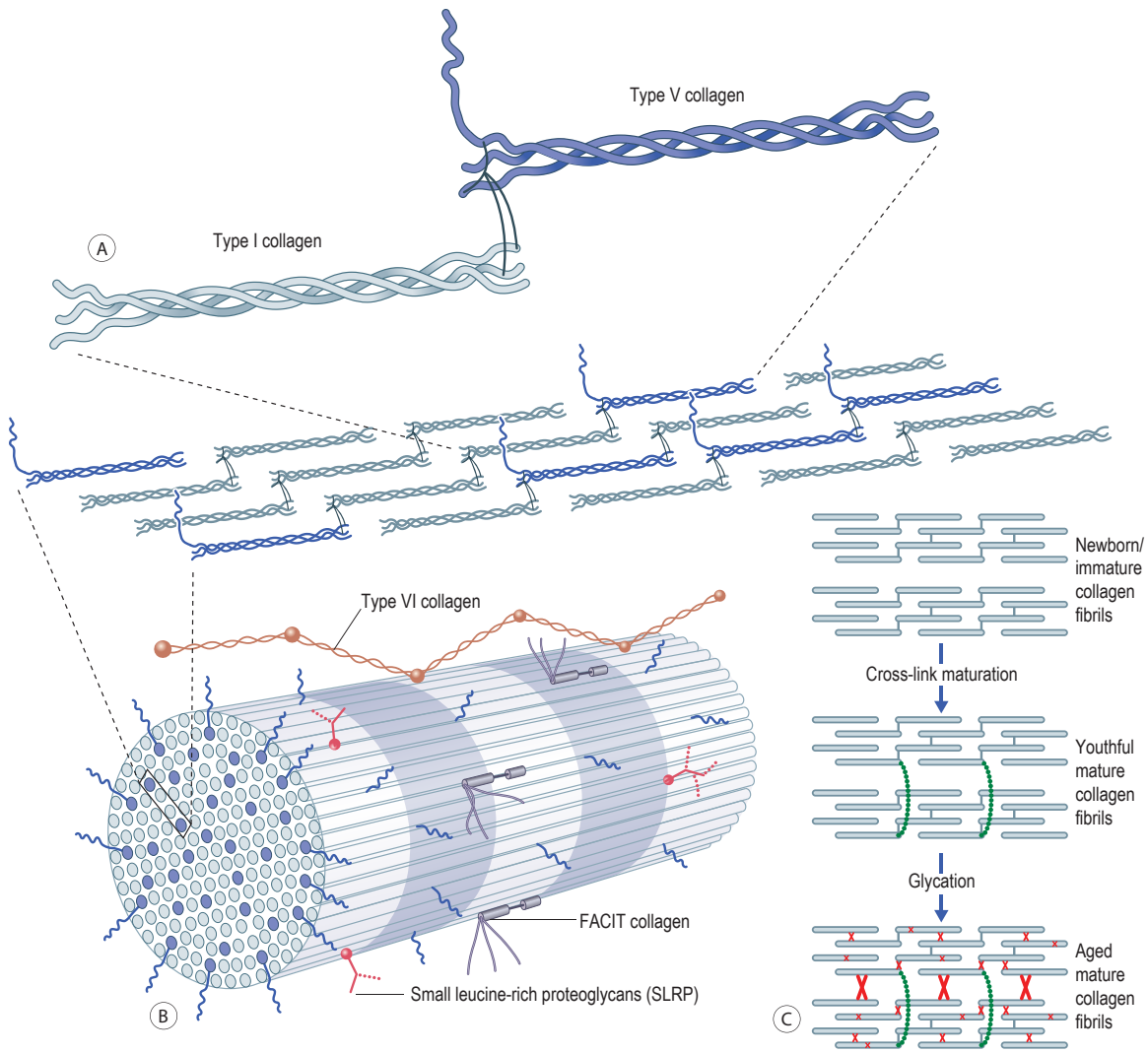


Figure 2-13: Molecular structure of collagen fibrils. (A) Collagen molecules (tropocollagen) of types I and V, which are triple helices of α -peptides. (B) Fiber-forming tropocollagens (I and V) are assembled into fibrils. (C) Maturation of intramolecular, intermolecular and interfibrillar cross-links. Reproduced from Alder's physiology of the eye [92].

In the corneal stroma, fibrils are further assembled into layers (lamellae) that run from limbus to limbus, roughly parallel to the surface of the cornea. Within a lamella, fibrils run parallel to each other and to the corneal surface. There are approximately 300 lamellae through the depth of the cornea near the center, and about 500 at the thicker periphery, near the scleral junction [110].

The organization of the lamellae varies with depth within the stroma and is illustrated in Fig. 2-14. In the anterior third of the cornea, lamellae are relatively thin

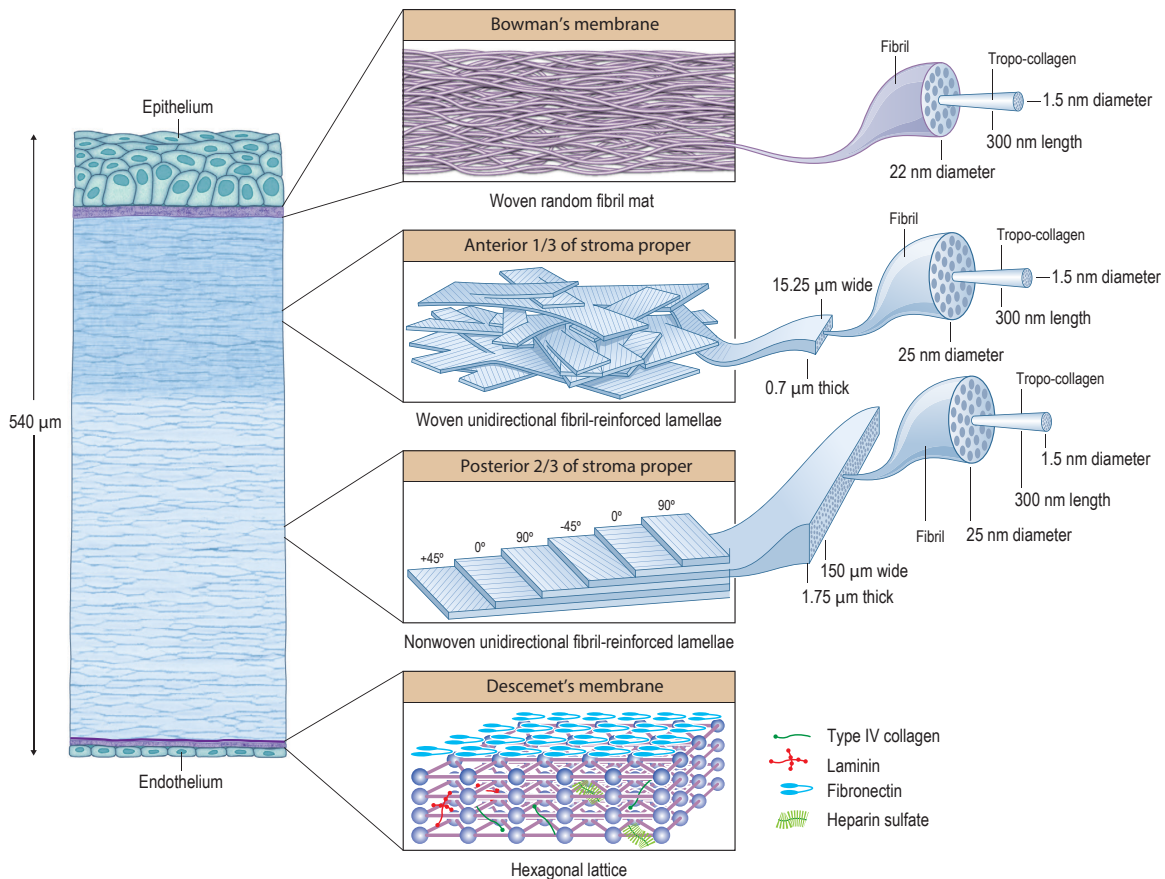


Figure 2-14: Hierarchical arrangement of collagen cornea. Reproduced from Alder's physiology of the eye [92].

(0.2–1.2 μm thick) and narrow (0.5–30 μm wide), and their angle with respect to the corneal surface varies widely (0 to 36 degrees), thus forming a complex interwoven nest of fibers. In the posterior two thirds, the fibers are thicker (1–2.5 μm thick) and wider (100–200 μm wide), are parallel to the corneal surface, and have only minimum interweaving [92]. For completeness, let's mention that in Bowman's layer, collagen fibrils are randomly interwoven and do not form lamellar structure. X-Ray diffraction studies have shown that lamellae are not randomly oriented, but rather have preferential orientations [111]. In the central part of the cornea, lamellae run mostly along the naso-temporal or the superior-inferior axis, adjacent layers crossing at 90 degrees. Closer to the limbus, they run circumferentially, forming an annulus of collagen that holds the cornea near the sclera junction where curvature changes rapidly.

Within a lamella, fibrils run parallel to each other, organized in a hexagonal lattice. They bathe in an aqueous matrix predominantly composed of water and proteoglycans, and other components such as free (non fibril-forming) collagens, glycoproteins, etc [111]. An important role of the proteoglycan matrix is to maintain fibrils separated by a constant distance (57 nm from fibril center to fibril center). The high level of order of collagen fibrils is thought to be an important factor of corneal transparency.

2.4.3 Complex mechanical behavior of the cornea

The cornea is a complex biocomposite material, and its mechanical properties arise from the collagen microarchitecture and the extrafibrillar matrix described in the previous section. In this regard, we are now in position to appreciate that many of the classic assumptions made in analyzing mechanical behavior of materials (homogeneity, elasticity, linearity and isotropy) do not hold for the cornea.

Because the collagen microstructure varies as a function of depth and location on the cornea, the material properties are position-dependent, or inhomogeneous. This property has been observed experimentally on many occasions, with the anterior part of the stroma being consistently found to be stiffer than the posterior due to the higher number of cross-links and interweaving [144, 165, 174].

Cornea, similarly to most soft biological tissues, also displays viscoelasticity. This property indicates that the force required to deform a material depends on the rate at which the deformation occurs. It originates from the dissipation of energy during deformation, caused by friction between fibrils and the surrounding matrix gel.

Mechanical studies conducted on corneal explants have shown significant nonlinearity of the stress-strain response [44, 194]. This behavior is thought to originate from the arrangement of collagen fibers, which are initially wavy and easily extensible, but progressively align along the stress direction, making them harder to deform.

Individual fibrils are very resistant to loads applied along the fiber axis, whereas the cohesion forces between fibrils are much weaker. Lamellae of bundled fibrils therefore display significant mechanical anisotropy: they are highly resistant to tensile

loads, but bend and shear readily. The superposition and interweaving of multiple layers that are oriented in orthogonal directions, with a wide distribution of angles within the cornea plane, results in a structure that has high rigidity to pressurization on the posterior side (such as IOP). However, it is relatively weak to in-plane shear stresses, such as those induced by frequent and intense eye rubbing. Indeed, these are known to be significant risk factors for developing corneal ectatic disorders such as keratoconus [106, 107].

2.4.4 Measuring cornea biomechanical properties

As a result of its elaborate microarchitecture and complex mechanical behavior, it is difficult to quantify and even describe mathematically the mechanical properties of the cornea. Measuring such properties in live humans is even more challenging. A wide array of experimental techniques have been necessary to construct our current understanding of cornea biomechanics, which have been summarized in Table 2.3. It is important to note that these different approaches tend to measure different types of tissue properties, and at different length scales, resulting in widely different values of the reported elastic constants.

Standard mechanical measurements

A large part of what we know about cornea mechanical properties was obtained using standard mechanical testing conducted *ex vivo*. Extensiometry is a standard approach in engineering for measuring Young's modulus of materials. Narrow strips of cornea and sclera are typically cut by a scalpel or fixed parallel razor blades. The strip ends are clamped to an instrument that measures the applied force and elongation while the ends of the strips are progressively pulled apart. For a known strip cross-section,

Table 2.3: Overview of methods used for biomechanical measurements of the cornea.

Method	Measured property	In vivo	Refs.
Standard mechanical tests			
Strip extensiometry	Tensile Young's modulus	No	[24, 55, 119, 127]
Inflation testing	Tensile Young's modulus	No	[21, 44]
Shear rheometry	In-plane shear modulus	No	[174]
Atomic force microscopy (AFM)	Elastic modulus (nanoscale)	No	[197]
Clinical instruments			
Ocular Response Analyzer (ORA)	Empirical parameters	Yes	[128]
Corvis ST	Empirical parameters	Yes	[4]
Novel techniques			
Compression OCE	Empirical parameters	Yes	[32, 49]
Traveling wave OCE	Shear modulus	Possible	[7, 190]
Phase-decorellation OCT	Diffusion coefficient	Yes	[14]
Ultrasond elastography	Shear modulus	Possible	[66, 182]
Acoustic radiation force	Elastic modulus (microscale)	No	[114, 115]
Brillouin microscopy	Longitudinal (bulk) modulus	Yes	[162, 168]

the stress σ and strain ε can be computed, and Young's modulus E is calculated from:

$$E_x = \frac{\sigma_{xx}}{\varepsilon_{xx}} \quad (\text{Linear material}) \quad (2.82)$$

$$E_x = \frac{\partial \sigma_{xx}}{\partial \varepsilon_{xx}} \quad (\text{Tangential modulus}) \quad (2.83)$$

$$E_x = \frac{\Delta \sigma_{xx}}{\Delta \varepsilon_{xx}} \quad (\text{Secant modulus}) \quad (2.84)$$

where the subscripts indicate that Young's modulus in the x direction is obtained from applying a tensile load along x on a face of the strip that has its normal along x (xx subscript of the stress and strain tensors). Note that in nonlinear materials, it is not possible to define a unique elasticity modulus. It must rather be defined as the local slope (computed as a tangent or secant) of the stress-strain curve around a specific load.

Strip extensiometry has been adopted early [55, 127], and is still commonly used in the study of cornea biomechanics [24]. However, it was recognized that extensiometry tests could induce important artifacts by cutting some of the collagen fibrils and due to the high level of inhomogeneity and anisotropy in the cornea. In an attempt to reproduce more faithfully the loading conditions created by intraocular pressure, some authors have preferred to use inflation tests [44, 194]. In this case, a corneal button is cut and tightly clamped on a pressurization chamber. The deformation of the cornea is measured while the pressure is increased. Pressurization induces tensile stress in the corneal wall according to Young-Laplace's principle:

$$\sigma_{rr} = \frac{PR}{2h} \quad (2.85)$$

where σ_{rr} is the in-plane radial stress, P is the intraocular pressure, R is the radius of curvature of the cornea and h is the corneal thickness. Detailed calculations used in practice to extract the elastic modulus are slightly more elaborate and will not be reproduced here, but essentially involve correcting the above formula for non-uniform thickness and calculating the apical displacement. The elastic modulus measured by this technique, as in strip extensiometry, is the in-plane Young's modulus that

represents the resistance of collagen fibers to axial loading, although in inflation tests this value is averaged over the whole corneal surface and along all fibril orientations.

Other standard material characterization techniques worth mentioning here include shear rheometry, and atomic force microscopy (AFM). Shear rheometry [134, 174, 176] measures the resistance to deformation induced by a load applied along the face over which it is applied. It probes the cohesion forces between lamellae and between fibrils, rather than the tensile rigidity of the fibrils themselves. AFM probes the material using a nanometric probe tip, which measures the stiffness of fibrils or of the extrafibrillar matrix separately at the nanoscale, rather than the effective material properties of the bulk cornea [197].

Commercial clinical instruments

Standard mechanical techniques can be used to improve our basic understanding of corneal biomechanics, but they cannot be applied on live humans. There is a clinical need for patient-specific measurements of biomechanical properties, which are involved in keratoconus and post-lasik ectasia [5, 56, 152, 187]. Early detection and screening is increasingly recognized as important in management of keratoconus [107], and biomechanics holds great promise to open up new avenues for diagnosis and management.

There is no clinically available instrument that can directly quantify the elastic modulus of corneal tissues, but it is possible to probe biomechanics indirectly using two clinically available instruments: the ocular response analyzer (ORA) and the Corvis ST. Both devices measure the response of the cornea to air-puff stimulus, either using scattered light intensity (ORA) or high-speed scheimpflug imaging (Corvis).

ORA measures the corneal hysteresis, which is defined as the pressure difference between the forward and backward applanation. This parameter was found to vary significantly in normal VS keratoconic eyes [99, 128, 167].

The ORA measures light scattered from a single point on the cornea, and therefore the information that can be obtained from such measurements is limited. Measuring two-dimensional profiles of the cornea as it deforms under air-puff stimulus can

provide more rich information, and has been performed using the Corvis ST as well as OCT [37, 62]. By combining multiple parameters derived from Scheimpflug imaging into regression and classification models, along with other information obtained from topography and tomography, recent studies have shown enhanced detection of corneal ectasia [4, 46].

While the important progress realized using those clinical instruments strongly supports the idea that *in vivo* biomechanical measurements can have clinical applications, these approaches have two important limitations. First, they lack spatial resolution, which might be important because biomechanical changes and tissue deformations observed in ectasia are focal in nature. Second, they do not directly quantify the elastic modulus, making the data interpretation difficult and limiting the use of the measured output in analytical and numerical models of corneal behavior.

OCT Elastography

The basic concepts of OCT elastography (OCE) have previously been described in section 2.1.2. For the specific context of cornea imaging, OCE has numerous potential benefits. The parent technology (OCT) is one of the most powerful techniques for imaging the eye, with a good balance of resolution, penetration and imaging speed. It is widely used clinically and therefore OCE could potentially have a low barrier to adoption. OCE can be made non-invasive [7, 185] or minimally invasive for cornea measurements [32]. OCE has the potential to provide spatially-resolved measurement, which is important for diseases like keratoconus where biomechanical changes are localized. It can also analyze the frequency-dependent behavior of materials, which is important due to the inherent viscoelasticity of the cornea. Finally, with an appropriate mechanical model, OCE can provide quantitative measurements of the elastic moduli, which could be used in simulation-based, patient-specific models to predict disease progression or reaction to a specific treatment.

Note that there are usually compromises to make between spatial resolution, frequency resolution and quantitative mapping, and it is not clear at this moment if all can be achieved simultaneously. However, different imaging protocols could in

principle be used depending on the specific clinical or experimental context.

Other novel technologies

We briefly discuss here some other novel technologies that have been proposed for measuring corneal biomechanics. One technique that has attracted a significant amount of attention is Brillouin microscopy [161, 162]. This technique is based on inelastic scattering of light by the ambient background of acoustic waves present due to thermal agitation. The optical frequency shift $\Delta\nu_B$ associated with this exchange of energy between photons and phonons can be expressed as

$$\Delta\nu_B = \frac{2n}{\lambda_0} \sqrt{\frac{M}{\rho}} \cos(\theta/2) \quad (2.86)$$

where n is the refractive index of corneal tissue, λ_0 is the free-space wavelength of the probing light, M is the longitudinal compression modulus, ρ is the density and θ is the cone angle between the incident and detected light beam. Note that the factor $\sqrt{M/\rho}$ is in fact equal to the velocity of compression waves (P-waves) in the tissue. It is important to note that the longitudinal modulus is essentially a measure of the compressibility of a material. In soft tissues, it is generally orders of magnitude higher than Young's modulus and the shear modulus, which are measures of how a material can be deformed. Another particularity of Brillouin imaging is the spatiotemporal regime in which it probes tissue mechanics (multiple GHz frequency band, and micron-scale spatial regime). Because of these properties, Brillouin measurements are not directly equivalent to the more generally used Young's modulus. Nevertheless, Brillouin imaging can probe biomechanics with exquisite spatial resolution, and studies have shown promise for the evaluation of keratoconus [159, 168], collagen cross-linking [160] as well as hydration-related disorders [169].

Other recently developed technologies include acoustic radiation elastic force microscopy (ARFEM) and phase-decorrelation OCT (PhD-OCT). In ARFEM, a femtosecond laser is used to generate a microcavitation bubble inside corneal tissues, which is then actuated using acoustic radiation force [114, 115]. The bubble displacement δx

is tracked using ultrasonic imaging, and Young's modulus can be calculated for a given bubble radius a and ultrasound wave velocity c_p and intensity I from the equation:

$$E = \frac{Ia}{2c_p\delta x} \quad (2.87)$$

PhD-OCT measures dynamic light scattering from the particles and structures inside the stroma matrix which undergo Brownian motion [114, 115]. The technique is based on measuring the decorrelation time of OCT-measured speckle pattern, which is related to Einstein's diffusion coefficient D , defined as

$$D = \frac{k_B T}{6\pi\eta R} \quad (2.88)$$

where k_B is Boltzkan's constant, T is the temperature, η is the matrix viscosity and R is the radius of the particle undergoing Brownian motion. From this definition, it appears that this technique does not quantify the corneal stiffness, but rather the viscosity of the interfibrillar matrix.

Chapter 3

Middle-ear vibrography

The original version of this chapter was published in :

Antoine Ramier, Jeffrey Tao Cheng, Michael E. Ravicz, John J. Rosowski, and Seok-Hyun Yun. Mapping the phase and amplitude of ossicular chain motion using sound-synchronous optical coherence vibrography. *Biomedical Optics Express*, 9(11):5489, nov 2018

Abstract

The sound-driven vibration of the tympanic membrane and ossicular chain of middle-ear bones is fundamental to hearing. Here we show that optical coherence tomography in phase synchrony with a sound stimulus is well suited for volumetric, vibrational imaging of the ossicles and tympanic membrane. This imaging tool — OCT vibrography — provides intuitive motion pictures of the ossicular chain and how they vary with frequency. Using the chinchilla ear as a model, we investigated the vibrational snapshots and phase delays of the manubrium, incus, and stapes over 100 Hz to 15 kHz. The vibrography images reveal a previously undescribed mode of motion of the chinchilla ossicles at high frequencies.

3.1 Introduction

The tympanic membrane (TM) and ossicular chain play a central role in hearing by providing acoustic impedance matching between the air-filled ear canal and the fluid-filled inner ear. The incoming sound energy is collected by the TM, transmitted through the ossicles to the cochlear fluid, and detected and transformed to neural signals in the inner ear. A dysfunction or damage in the middle ear results in hearing impairment.

Vibrometric measurement of the ossicles and TM has been critical for advancing our understanding of the hearing mechanics and improving treatments such as middle-ear prosthetics. Vibro-acoustic analysis of the middle ear and TM has also been proposed for diagnosis of ossicular disorders and planning surgical interventions [68, 155, 201]. In the past, stroboscopic microscopy, capacitive probes, and the Mössbauer effect were used to measure the sound-induced vibrations at specific locations in the middle ear [158, 188]. Modern investigations are generally conducted using more sensitive optical interferometric techniques, particularly laser Doppler vibrometry (LDV) and holography [78, 148, 183]. LDV and holography are surface measurement techniques and, therefore, require surgical preparation to access structures beyond the TM [153]. They are also subject to artefacts caused by other vibrating structures located behind the tissue of interest if those structures are sufficiently reflective [30].

Optical coherence tomography (OCT) is a cross-sectional imaging modality and its potential for structural imaging of the middle ear has been previously explored [135], primarily for assessing pathologies, such as otitis media [117], middle ear effusions [116], and cholesteatoma [34], in diagnostic and intraoperative settings [63, 74]. Beyond anatomical imaging, phase-sensitive OCT has shown a promising potential for vibration measurements in hearing research [28, 90, 129, 149, 150, 189, 192]. Subhash et al. made one of the first demonstrations of depth-resolved OCT vibrometry at a sound frequency of 500 Hz using a spectrometer-based OCT system [181]. Several groups demonstrated OCT vibrometry of the TM [18, 26, 80, 131] and ossicles [100, 132] with improved imaging and processing speeds, as well as interfaces suitable for live

patient imaging. Up to now, the demonstrations of OCT-based middle ear vibrometry have been largely focused on vibration magnitude, and vibration phase has been generally overlooked. Measuring the phase of vibration with respect to sound stimuli allows the acoustic phase and group delays to be determined along different middle ear components. Accurate measurements of the relative phase of motion along the ossicular chain can help determine modes of motion and identify differences between normal and pathologic states. We have previously developed a technique, called OCT vibrography, to acquire the magnitude and phase of vibration at each location through successive vibrational cycles and reconstruct effective snapshot images of the TM and ossicular motion. However, the system had a limited frequency range below 3 kHz and suffered from random phase noise drift with respect to the sound source, making it difficult to measure phase delays through the ossicular chain reliably and accurately [22].

In this article, we present an improved OCT system that has overcome these two limitations and demonstrates considerably more precise measurement of the phase delay along the ossicular chain. In chinchilla ears, our results revealed a new mode of vibration, involving twist and bending of the ossicular structure, for acoustic transduction at frequencies above 10 kHz.

3.2 OCT vibrography system

3.2.1 Optical system, sound stimulus, and time synchronization

The imaging system (Fig. 3-1) uses a wavelength-swept laser based on a rotating polygon mirror [23, 199, 200]. The laser output has a center wavelength of 1280 nm and a 3-dB bandwidth of 80 nm at a sweep rate of 45 kHz. The corresponding axial resolution is 15 μm . A fiber-based Mach-Zehnder interferometer (MZI) (Thorlabs INT-MZI-1300) is employed to provide reference interference fringes for clock jitter compensation. In the sample arm, the laser beam is scanned by a pair of galvanometer

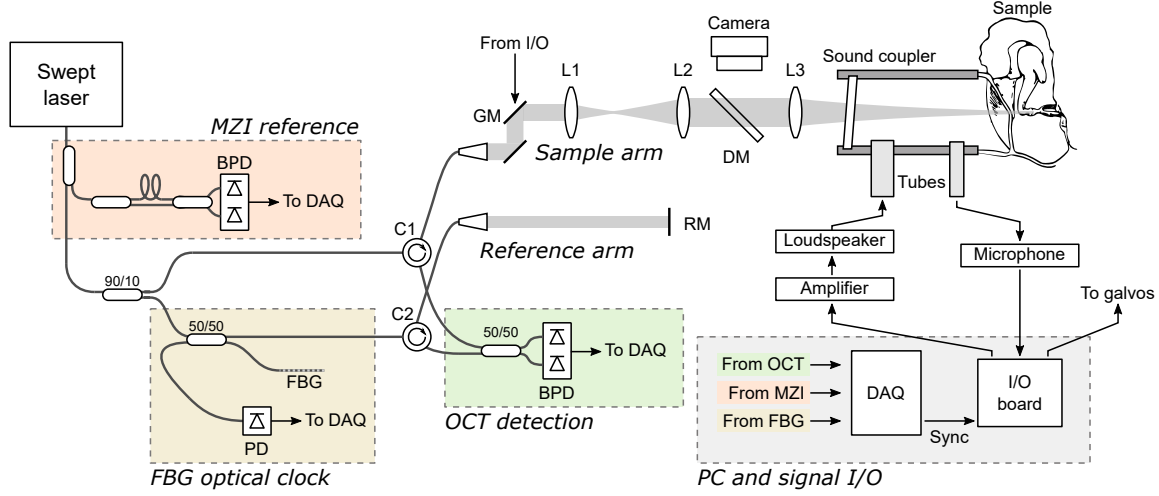


Figure 3-1: Schematic of the optical system and signal generation and acquisition. Abbreviations used: Mach-Zehnder interferometer (MZI), photodiode (PD), balanced photodiode (BPD), data acquisition (DAQ) system, fiber Bragg grating (FBG), circulators (C1, C2), galvanometer mirrors (GM), lenses (L1-L3), reference mirror (RM), dichroic mirror (DM).

mirror scanners (Cambridge Technology, 6210H), expanded by lenses L1 (50 mm) and L2 (75 mm) and focused by an objective lens L3 (100 mm) to a spot size (lateral resolution) of 30 μm (full width at half maxima) at the focus. The total optical power incident on the sample is 10 mW. Additionally, a long-pass dichroic mirror with a cutoff wavelength of 950 nm is employed and directs room light reflected from the sample to a CCD camera (Allied Vision, Mako G) to provide an otoscopic view of the sample, facilitating sample alignment.

An all-purpose input/output (I/O) board (National Instrument, USB-6353) is used to generate electrical waveforms to drive a compression speaker (Peavey RX22) via a 300 W power amplifier (Crown Audio, XLI). The output face of the speaker is directly coupled to a latex tube connected to a custom-built sound coupling tube made of brass. One side of the brass tube has a transparent, tilted glass window to transmit the optical imaging beam. The other side of the tube is coupled to the auditory canal of the specimen. A low-noise microphone (Etymotic ER-7C) in the coupler records the stimulus sound pressure in situ within 5 mm of the center of the TM.

A fiber Bragg grating (FBG) and photodiode (PD) provide a pulse signal synched to each wavelength sweep of the laser output (“FBG optical clock”). This signal triggers

a high-speed data acquisition (DAQ) card for digitizing interferometric signals from dual balanced photodetectors (BPD) in the OCT interferometer and the reference MZI. The output trigger of the DAQ card is then used as the clock “Sync” signal for the I/O board that generates the sound stimulus, controls the galvanometer scanners, and acquires the microphone signal. This arrangement ensures time synchronization for the measurement of OCT interference signals, beam scanning, and the generation and recording of sound waves. The timing jitter measured using a digital oscilloscope (Keysight DSO1024A, 200 MHz, 2 GS/s) between the I/O board output and the FBG clock was 5.7 ns, which provides a phase uncertainty of less than 9×10^{-5} cycles with stimuli of 15 000 Hz.

3.2.2 Data acquisition in synchrony with sound frequency

Each complete wavelength (λ) sweep of the laser yields an individual axial scan (A-line) along the depth (z) axis. The optical beam is scanned in the transverse directions (x and y) to form a complete volume image. The A-line rate (f_A) is the same as the wavelength-sweep repetition rate. The digitization rate of the DAQ is set to 99 MHz so that 2,048 samples of the dual-balanced detector signal are acquired during each A-line. For phase synchrony, the acoustic frequency f_s is restricted to be an integer fraction of the A-line rate; that is, $f_s = f_A n / m$, where n and m are integers. The data acquisition and beam scanning are arranged such that m A-lines are acquired at every transverse location (an M-scan) during n cycles of the sound wave (Fig. 3-2). Typically, we set m to be a rather large, even number in a range of 180 to 250, and n is variable from the minimum of 1 for low sound frequencies, up to 100 for high frequencies within the Nyquist criterion. With $m = 200$, for example, for a wavelength sweep rate of 45 kHz, the allowed f_s ranges from 225 Hz ($n = 1$) to 22.5 kHz ($n = 100$) at an interval of 225 Hz. A different m value yields a different set of f_s . This allows a wide range of sound frequencies to be tested. For $f_A = 45$ kHz and $m = 200$, the acquisition of a single M-scan at each transverse location takes 4.44 ms, regardless of the sound frequency. Data acquisition over an entire frame (128 M-scans) or volume (128×128 M-Scans) takes 0.57 s and 72.7 s, respectively. Such sampling produces a

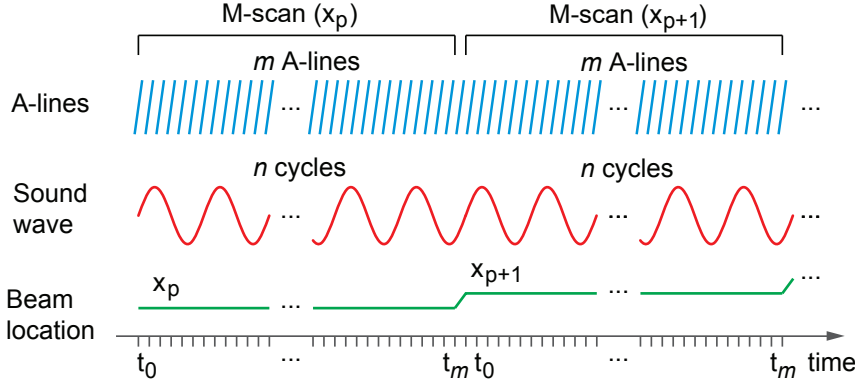


Figure 3-2: Timing diagrams of data acquisition, sound wave, and beam position scan.

3D data set of vibrography images at one sound frequency of $1024 (z) \times 128 (x) \times 128 (y)$ voxels. Such a measurement set is repeated for each sound stimulus frequency.

3.2.3 Data processing to determine the amplitude and phase of vibration

For each A-line, the wavelength-domain interferogram is corrected for a background offset and resampled linearly in wavenumber (k) based on the MZI reference data [17]. This step also reduces timing jitter between the data acquisition clock and wavelength sweep [186]. The resampled interferogram is multiplied by an apodization window function and further corrected for chromatic dispersion in the interferometer. The corrected interference fringes $a(k, t, x, y)$ are Fourier transformed (k to z) to produce an A-line profile, $A(z, t, x, y)$. The magnitude of the complex A-line represents optical reflectance and is displayed (in log scale) to show the structure of the sample. The phase $\phi(z, t, x, y)$ of the A-line contains the z-axis coordinates of the structure within a sub-wavelength range. It should be noted that the phase ϕ represents the phase of the optical interference signal and should not be confused with a “vibration phase” denoted φ , which refers to the phase of the mechanical motion of the structure. The sinusoidal displacement of each voxel at (z, x, y) at time t , $u_z(z, t, x, y) = |u|e^{i(2\pi f_s t + \varphi)}$

is linked to the interference phase OCT via:

$$u_z(z, t, x, y) = \frac{\lambda_0}{4\pi n_0} \phi(z, t, x, y) \quad (3.1)$$

where λ_0 is the center wavelength of the swept source in vacuum, and n_0 is the refractive index of the medium. The optical phase difference $\Delta\phi$ between adjacent A-lines at each spatial location is computed with [75]:

$$\Delta\phi(t, \text{ROI}) = \arg \left(\sum_{\text{ROI}} A^*(z, t_{i-1}, y) A(z, t_i, x, y) \right) \quad (3.2)$$

where A^* denotes the complex conjugate of $A(z, t, x, y)$, and the summation is carried over a region of interest (ROI) for averaging motion within the region. The ROI may be a short axial segment or small volume. The averaging enhances the effective sensitivity of phase measurement without affecting spatial resolution because phase does not change significantly over multiple imaging voxels. The ROI-averaged displacement function is given by: $u_z(t_k, \text{ROI}) = \frac{\lambda_0}{4\pi n_0} \sum_{i=1}^k \Delta\phi(t_i, \text{ROI})$, where the summation integrates the phase differences to obtain accumulated absolute phase from t_0 , the beginning of each sound wave cycle.

The time series of displacement functions $u_z(t, \text{ROI})$ contains all the information about the axial component of the sound-driven vibration. The magnitude and phase of the mechanical vibration at the sound frequency can be readily obtained by a Fourier transform of the displacement with respect to the time coordinate:

$$U_z(f, \text{ROI}) = \mathcal{F} \{ u_z(t, \text{ROI}) \} \quad (3.3)$$

The amplitude and phase of $U_z(fs, x, y, z)$ at the applied sound frequency f_s gives the magnitude and phase of vibration in response to the stimulus. The acoustic transfer function is obtained by normalizing the measured signal with respect to the input sound stimulus recorded with the microphone. Axial velocity v_z ($\equiv du_z/dt$) is computed from $(i2\pi f_s)U_z(f_s)$.

The smallest vibration that can be measured is ultimately limited by the optical

signal-to-noise ratio (SNR), defined as the power ratio of the amplitude (reflectivity) to the noise floor of $|A(z, x, y)|$. To a first-order approximation, the theoretical limit of vibration sensitivity σ_u is given by [27, 186, 198]:

$$\sigma_u = \frac{\lambda_0}{4\pi n_0} \frac{1}{\sqrt{\text{SNR}}} \quad (3.4)$$

Upon taking the Fourier transform (t to f), the M-scan is effectively averaged m times, such that the frequency-domain amplitude sensitivity is $\sigma_{|U|} = \sigma_u / \sqrt{m}$. The theoretical sensitivity can be further improved with ROI averaging (described above) by a factor of \sqrt{N} when the ROI consists of N samples with an equal SNR.

The SNR-limited vibration phase noise is linked to the amplitude noise and given by:

$$\sigma_\varphi = \frac{\sigma_{|U|}}{|U|} \quad (3.5)$$

The phase noise is also reduced by a factor of \sqrt{N} when the data are averaged over N samples.

At stimulus levels above ~ 100 dB SPL, the TM can move more than $\lambda_0/2$ between two consecutive A-line scans, making $|\Delta\phi| > \pi$. This can cause a phase wrapping artifact in the phase-sensitive measurement because the phase difference $\Delta\phi$ has 2π ambiguity. In addition, the TM motion can generate erroneous optical phase readings when the amplitude of motion becomes larger than the axial resolution of the OCT system. To avoid these artifacts, we limited the stimulus to levels where these artifacts did not occur. When we concentrate on ossicular motion, the SPL level is varied to produce a full-range of ossicular motion, and care is taken to segment out the TM region causing artifacts.

3.2.4 System performance measurement: Phase sensitivity and stability

To characterize the sensitivity of our OCT vibrography system, we measured the vibration signal from a stationary object (2.8-kg block of aluminum) while varying the

SNR by adjusting the optical power in the sample arm using a variable attenuator. First, the galvanometer scanner was turned off, and a 1 s M-scan was acquired for each level of attenuation. Then, another set of M-scans was acquired while the galvanometer scanner was turned on and a constant voltage was applied so that the probe beam was held at a fixed location on the object. The optical SNR, motion amplitude sensitivity, and noise spectra were computed from the data set.

The sensitivity measured with the scanner off was in good agreement with the theoretical limitation (Fig. 3-3(a)). However, when the scanner was on, we found an excess amplitude noise with an amplitude of 4 nm, which is presumably due to mechanical jitter of the galvanometer mirror coupled with the feedback control of the driver. At relatively high SNR levels above 30 dB, the system's sensitivity was limited by this scanner noise. In most parts of the middle ear structure, the optical SNR tends to be below 30 dB, in which the measurement is SNR-limited. The noise floor without the scanner noise was flat in the frequency domain (Fig. 3-3(b)) as expected from a purely SNR-limited case. When the scanner was on and the SNR was > 35 dB, the mechanical scanner noise described a broad envelope centered around 8 kHz. The noise spectrum without the scanner noise revealed sharp noise peaks with an equal spacing of 625 Hz, which correspond to the 72 facets of the rotating polygon filter in the wavelength-swept laser source. We avoided these fixed noise frequencies when setting the sound stimulus frequency.

Next, to measure vibration phase noise we placed a piezoelectric transducer (PZT) in the sample stage. The transducer was driven to oscillate with an amplitude of ~ 5 nm at a constant frequency of 9 kHz. Figure 3-3(c) shows the variation of measured vibration phase relative to the phase of the stimulus over a duration of 1 s, measured synchronized to the stimulus generation as described above (“Sync”). Each data point represents an average of 225 A-lines, a simulation of ROI averaging with $N = 225$ that was used in some middle-ear imaging experiments described later. Apart from some random fluctuation, the measured phase was stable over time. However, when the PZT was driven by a function generator with an independent clock (“Sync Off”), we measured large, random phase drift, confirming the benefit to phase stability of

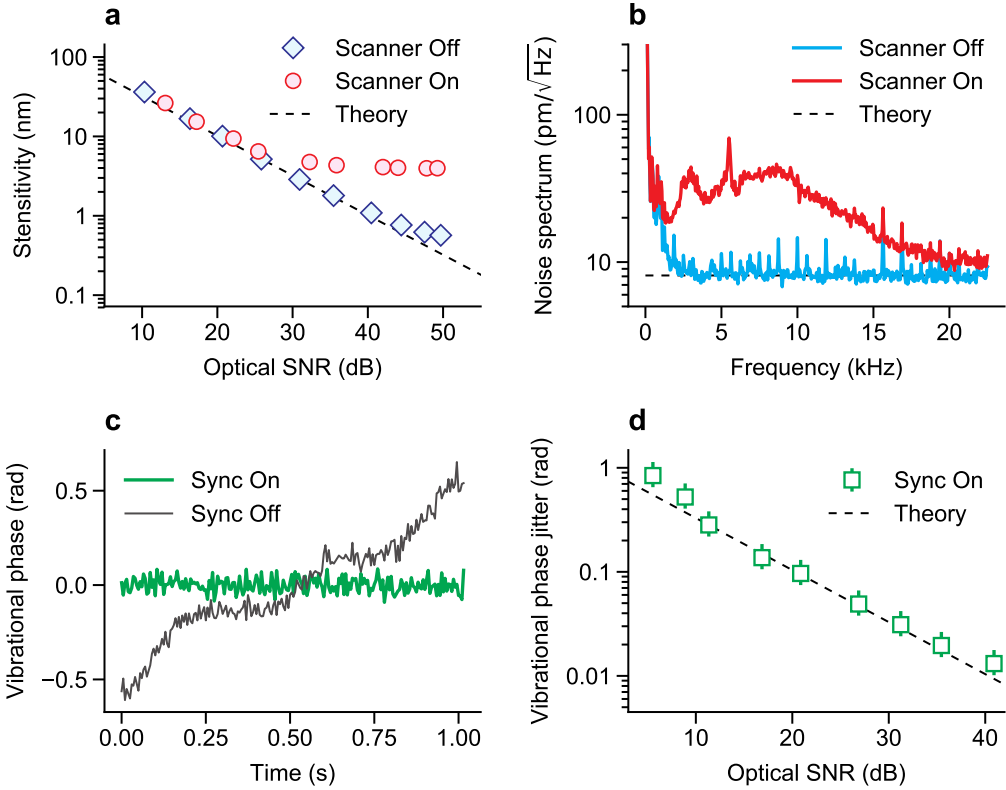


Figure 3-3: Measured SNR and sensitivity. (a) The noise-equivalent displacement measured as a function of the SNR when the 2-axis galvanometer scanner was powered ON (red circles) or OFF (cyan circles), in comparison to the SNR-limited theoretical curve (dashed line). (b) Power spectra of the vibrational signal at a SNR of 35 dB, when the scanner was powered off or on. (c) Measured vibration phases of the piezoelectric transducer showing the elimination of phase drift by synchronizing the phase of the stimulus signal to the acquisition board. (d) The standard deviation of the vibrational phase measured as a function of the SNR, which agrees well with the theoretical prediction (dashed line). Error bars represent 99% confidence intervals.

timing synchronization.

To characterize the phase noise, we varied the optical SNR using a variable attenuator in the sample arm of the OCT interferometer. The scanner was turned off to remove the effect of the mechanical noise. The result agreed well with the theoretical line for a SNR-limited case with $N = 225$ (Fig. 3-3(d)).

3.3 Results of chinchilla ear measurements

3.3.1 Vibrography imaging of the chinchilla middle ear

Vibrography experiments were performed on two cadaver chinchilla heads less than 2 weeks after sacrifice of animals. The specimens were kept frozen, and thawed a day before experiments. The head was mounted on a brass rod held in a multi-axis micro-positioner. The pinna, cartilaginous ear canal and much of the boney ear canal were removed to expose the central and superior areas of the TM. The thin dermal outer layer of the TM was removed to increase the transparency of the TM, and because the freeze thaw cycle had already loosened this layer over part of the TM surface. Laser-Doppler measurements have demonstrated that removing this layer has little effect on TM or ossicular motion. The specimen was positioned with a slight tilt around the long axis of the head to better view the incus and stapes. During each experiment, the remnant auditory canal was sealed to the sound coupling chamber using silicone molding material [154].

Prior to vibrography measurements, we scanned the OCT probe beam over the entire TM to acquire a 3D anatomical image of the middle ear. A representative cross-section and 3D rendered image are shown in Figs. 3-4(a) and 3-4(b). A large part of the ossicular chain could be observed, including the manubrium of the malleus underneath the TM, the long process of the incus, the anterior crus of the stapes, and the anterior stapes footplate. The head of the malleus and body of the incus are not visible because they are located behind the thick ear canal bone. Figure 3-4(c)-3-4(e) show the reflectivity and axial velocity magnitude and phase (φ) maps

of the cross-sectional plane, and clearly show all 3 ossicles: malleus, incus, and stapes. A $3 \times 3 \times 3$ Gaussian filter was applied to the reflectivity and vibrometry maps to reduce speckle noise (Figs. 3-44(c)-3-44(e)). The velocity and phase data were encoded in the structural image with color in a Hue-Saturation-Value (HSV) scheme using hue corresponding to the velocity or phase and color value being proportional to the reflectivity in log scale. The velocity was normalized to the sound pressure near the TM (in Pa) measured in real time using the microphone. The illustrated vibration phase is relative to the vibration of the umbo (rather than the speaker) so the phase at the umbo is always 0. The in-phase movement of much of the TM and three ossicles is clearly seen, whereas the vibration of the parts of the auditory canal and the wall and floor of the middle-ear cavity are of varied phase and of much smaller amplitude.

3.3.2 Acoustic transfer function of the middle ear

To measure the acoustic transfer function of the middle ear, we used two different methods. First, we fixed the probe beam at the umbo and used a Schroeder frequency comb [164] to obtain the complete frequency response of the umbo over a frequency range of 100 Hz to 5 kHz. The broadband stimuli did not have sufficient acoustic power to produce sufficient SNR (> 10 dB) at frequencies above 5 kHz, although longer integration time could increase SNR. It was repeated for the probe beam fixed at the incus tip to measure the acoustic transfer function near the head of the stapes. This method is commonly used in conventional LDV measurements. The main difference is that the OCT measurement is performed through the intact TM, whereas LDV require the TM above the incus to be removed. The broadband results are presented as solid lines in Fig. 3-5(a).

In the second method, we acquired volumetric vibrography data at a specific monotonous sound stimulus and repeated the measurement for different sound frequencies, typically, at 0.36, 0.5, 1.0, 2.0, 3.0, 4.5, 6.4, 9.0, 11.3, and 15.0 kHz. The SPL was set to a range between 80 and 100 dB. The axial velocity and phase of the umbo, incus and stapes were obtained by manually selecting ROI's in the volumetric dataset. The umbo ROI was defined as a 0.5mm diameter circle at the tip of the manubrium, and

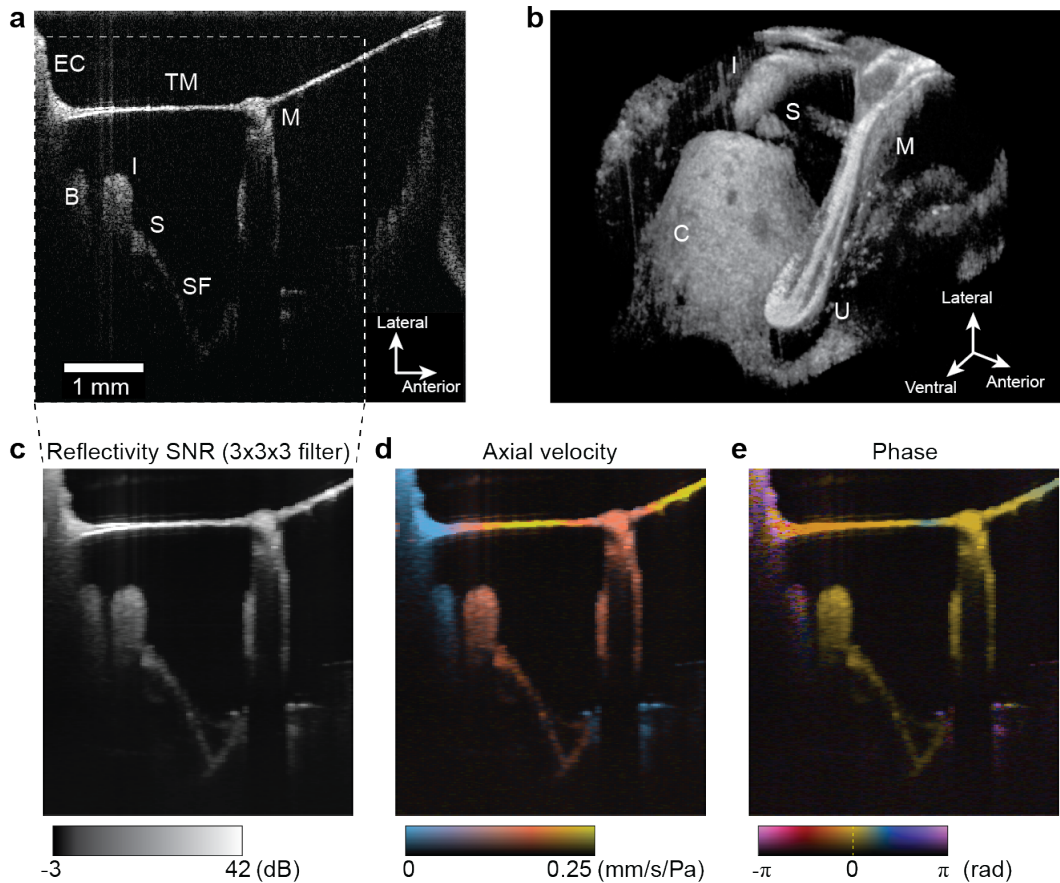


Figure 3-4: OCT images of the chinchilla middle ear. (a) Representative cross-sectional image of a plane orthogonal to the manubrium (long handle of the malleus). (b) Orthographic 3D reconstruction with the TM digitally removed. (c-e) Cross-sectional vibrography images measured with SPL of 100 dB at 500 Hz after averaging over a $3 \times 3 \times 3$ kernel of voxels. (c) standard reflectivity image in units of dB above the noise floor, (d) magnitude, and (e) phase maps. Labels: ear canal (EC), bone (B), manubrium (M), umbo (U), incus (I), stapes (S), stapes footplate (SF) and cochlear promontory (C).

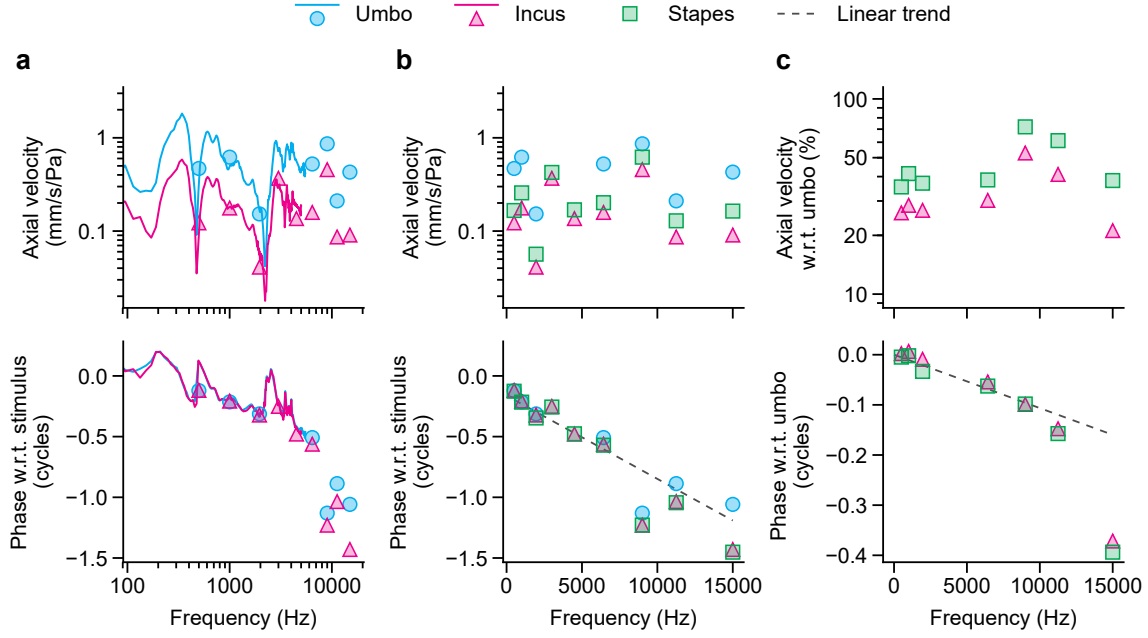


Figure 3-5: Acoustic transfer function of the ossicular chain. (a) The axial velocity magnitude and phase φ at the umbo and incus as a function of sound frequency (log scale). Lines: data obtained with broadband sound stimulus; markers: data obtained at discrete frequencies. (b) The data of the umbo (cyan), incus (magenta), and stapes (green) over frequency (linear scale). (c) The axial velocity and phase of the incus and stapes with respect to the umbo.

the incus and stapes ROI's were the entire visible portion of these ossicles. The data are shown in Fig. 5a-c as circle, triangle and square markers, respectively. The data obtained with the two distinct stimuli up to 5 kHz are in good agreement with each other. From 5 to 15 kHz, only results from monotonous stimulation are shown.

From the volumetric dataset, the acoustic transfer function at any location can be obtained. Figure 5b plots the velocity and phase transfer function of the stapes together with the data from the umbo and incus (in linear frequency scale). The phase of the umbo with respect to the sound stimulus varies with the frequency. A linear frequency dependence arises simply from wave propagation delay ($\partial\varphi/\partial f_a = 2\pi \times$ group delay time [146]. The observed linear slope (dashed line) corresponds to an average delay time of $\sim 67 \mu\text{s}$. The distance of $\sim 5 \text{ mm}$ between the microphone and the TM accounts for $15 \mu\text{s}$ (sound speed: 340 m/s); the rest of the delay may be attributed to the phase delay in the acoustic coupling from air to the TM, and

from the TM to the manubrium [136, 146]. Figure 3-5(c) highlights the magnitude and phase of incus and stapes motion relative to that of the umbo. The vibration amplitude of the stapes (green squares) is larger than that of the incus (magenta triangles), but both move less (35–75%) than the umbo over the entire frequency range. As frequency increases, the phase of the incus and stapes deviate from that of the umbo. The negative phase slope in (c) indicates an additional delay in the motion of the stapes and incus relative to the umbo. At frequencies less than ~ 8 kHz, the phase follows a nearly linear trend (dashed line), indicating a simple group delay of the mechanical wave. Above that frequency there is a sudden increase in the phase difference between the umbo and the other two ossicles; as will be described later, this increase can be explained by the onset of a new mode of ossicular motion. These measurements of the relative sound-induced motion of the umbo, incus and stapes are consistent with past measurements in the same species performed using Mössbauer and LDV [153, 158].

3.3.3 Projected and volumetric vibrography images of the TM and ossicular chain

Figure 3-6 show vibrography images of the TM in a top projection view at three different sound frequencies: 360 Hz, 4.5 kHz, and 9.0 kHz. At 360 Hz, the surface of the TM moves in phase with the stimulus. With increasing sound frequencies, the TM exhibits more complex vibration patterns with increasing numbers of maxima and minima in the velocity maps. The phase maps show complex patterns mixed with π phase shifts over a small distance, indicating standing waves, and more gradual phase gradients, indicating traveling waves. The presence of both standing and traveling components are consistent with previous measurements of sound-induced motion of the chinchilla TM using laser holography [154].

Figure 3-7 shows constructed vibrography maps of the ossicular chain in a projection view at 500 Hz, 6.4 kHz, and 15.0 kHz. The most prominent structure is the manubrium of the malleus (M), and to its left, the inferior part of the long process of the incus (I)

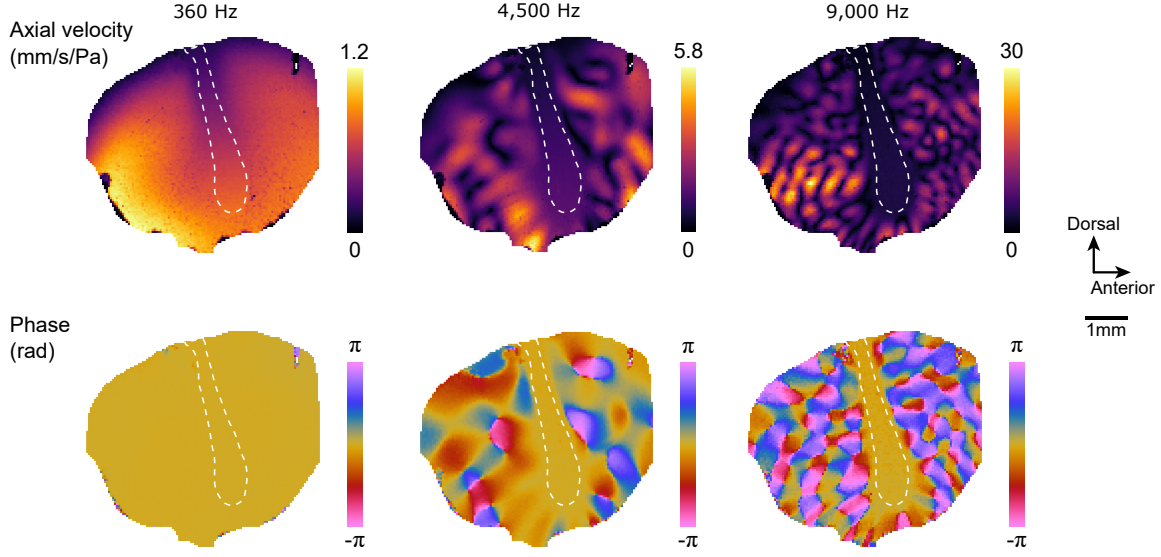


Figure 3-6: Projection view of the TM vibration at 360 Hz (107 dB SPL), 4.5 kHz (100 dB SPL) and 9.0 kHz (84 dB SPL). The dotted lines show the outline of the manubrium. The phases are scaled relative to the phase of motion of the umbo.

and the stapes (S) are seen. The head of the malleus and the body of the incus are behind the ear canal bone and so are not visible. At 500 Hz, the axial velocity increases along the manubrium from the lateral process (LP) to the umbo (U) (Fig. 3-7(a)), and the ossicles move all in phase (Fig. 3-7(d)). This motion is consistent with a lever-like rotation around the malleus-incus joint. At higher frequencies, the velocity gradient along the manubrium is increasingly nonlinear (Figs. 3-7(b) and 3-7(c)), and the phase of the upper most portion of the malleus (the lateral process), incus, and stapes lag from that of the umbo (Figs. 3-7(e) and 3-7(f)).

Phase gradients along the manubrium can be appreciated more easily with a reduced phase range for the color-coded display, shown in Figs. 3-7(g)-3-7(i). At 6.4 kHz, the phase gradient along the manubrium indicates a flexural motion of the ossicle (Fig. 3-7(h)). At 15 kHz, while the axial flex is present, most interestingly, a lateral phase gradient appears (Fig. 3-7(i)), suggesting a twist motion around the axis.

From the volumetric dataset, we constructed 3-dimensional rendering of the ossicular motion with exaggerated vibration amplitude. The movies taken at 500 Hz and 15 kHz clearly show the differences in the ossicular motion, particularly of the manubrium (Fig. 3-8(a)). At the low frequency, the in-phase rotational motion of

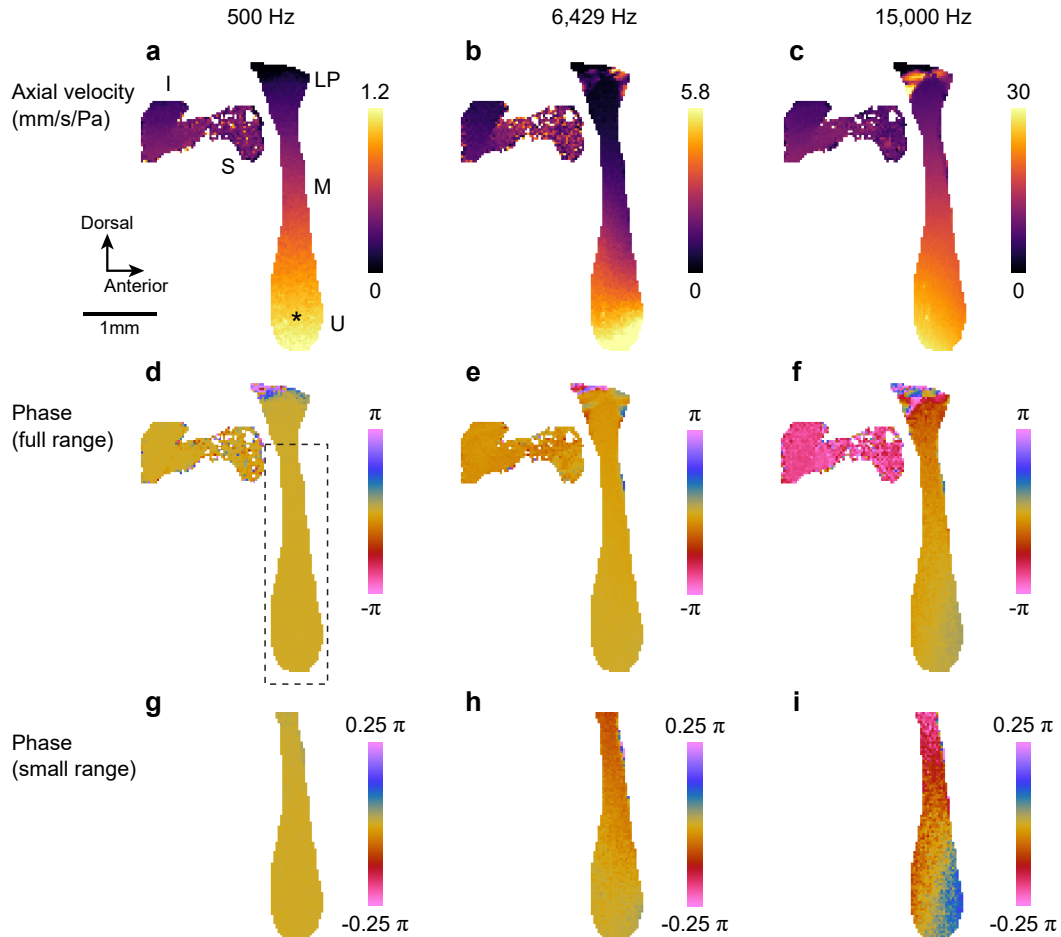


Figure 3-7: Projection view of the ossicular chain at 500 Hz (100 dB SPL), 6.4 kHz (108 dB SPL), and 15 kHz (103 dB SPL). (a-c) Axial velocity maps. (d-e) Phase maps relative to the umbo. (g-i) Phase maps of the manubrium (dashed box in d) relative to the umbo. The range of the colormap is reduced to help visualize phase gradients along the manubrium. Labels: manubrium (M), incus (I), stapes (S), lateral process (LP), umbo (U); * shows the umbo location used as phase reference.

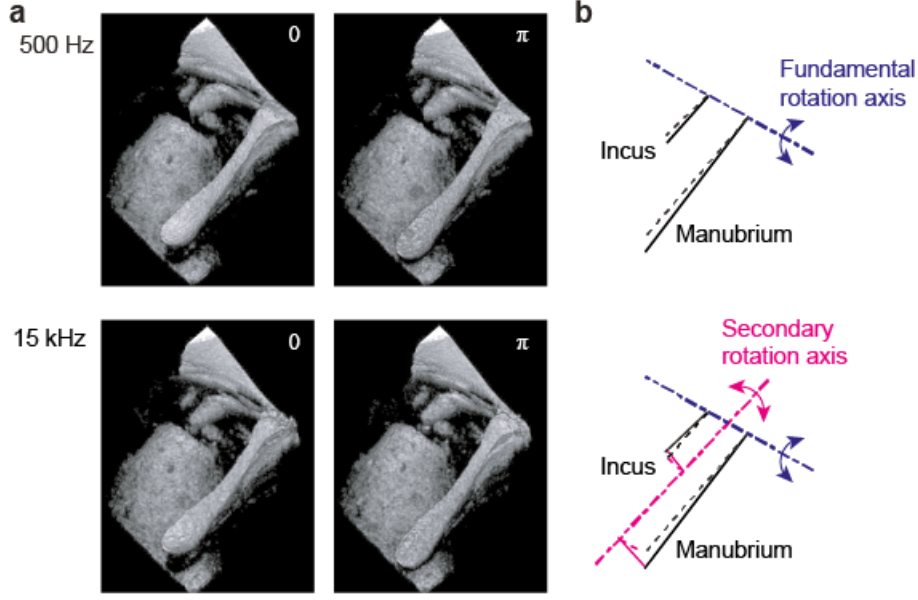


Figure 3-8: Reconstructed ossicular motion at 500 Hz and 15.0 kHz. (a) Motion-exaggerated animations and representative snapshots at $\varphi = 0$ and π . See Supplementary Visualization 1 for 500 Hz and Supplementary Visualization 2 for 15 kHz. (b) Schematics of the two rotational modes of ossicular motion. The fundamental mode is predominant at frequencies below 5 kHz. Above 9 kHz, the secondary rotational motion becomes evident.

the manubrium, incus and stapes around the malleus-incus axis is predominant. At 15 kHz, this fundamental rotational mode is accompanied by the second rotational motion around a new axis parallel to the manubrium. In addition, the twist motion and flexural bending of the manubrium are noticeable. Figure 3-8(b) illustrates the two modes of ossicular motion.

3.4 Discussion

The acoustic transfer function, projection phase maps, and reconstructed 3D rendered animations provide comprehensive and quantitative information and clear insights about the sound-driven motion of the ossicular chain. The near-half-cycle difference between the umbo and the incus-stapes at 15 kHz is consistent with the second ossicular rotational axis that is parallel to the manubrium and positioned between the manubrium and the incus. Such rotational modes have been hypothesized for small

mammals by Fleischer [47]. This additional rotational mode of the ossicular chain can function to increase the motion of the incus and stapes at higher frequencies and may contribute critically to the efficient acoustic conduction of the ossicular chain over 10 octaves of sound frequency [137].

OCT shows promise as a tool to aid the diagnosis of middle ear pathology, by allowing visualization of middle-ear structure behind the TM, and quantification of sound-induced ossicular motion that can help distinguish abnormal function and its causes [22]. The maximum sound frequency in the current OCT system is limited to the Nyquist frequency of 22.5 kHz. This frequency range is adequate for hearing research in humans (20 Hz to 20 kHz hearing range), and covers most of the chinchilla hearing range (50 Hz to 33 kHz) [64]. The total duration of a volumetric measurement, on the order of a minute, is a challenge for live patient or animal imaging due to motion artifacts. One possible approach, explored by MacDougall and colleagues [100], is to use standard anatomic OCT imaging to target a single location at which vibrometry can rapidly be performed. OCT systems with higher A-line rates of up to several MHz have been reported [83, 170] and may enable considerable reduction of the total measurement time by allowing data acquisition in the B-M mode (comparing phases between successive B-scans [179]) instead of the M-B mode (comparing phases between successive A-lines) used in this study.

In conclusion, we have described OCT vibrography for measuring and visualizing the sound-induced motion of the ossicles and TM and demonstrated its usefulness through the measurement of the chinchilla ear. The acoustic transfer functions we recorded are consistent with previous measurements obtained by LDVs and holography measurements. However, the unique ability of OCT vibrography to acquire volumetric data in conjunction with 3D structural images enabled us to appreciate the greater details of the ossicular motion, including the fundamental rotation around the malleus-incus axis and, importantly, to identify a second rotational mode of ossicular motion at high frequencies. Our results demonstrate OCT vibrography as a powerful tool in hearing research.

Funding

This work was funded by the National Institutes of Health through grants P41-EB015903 (to S.Y.) and R01-DC000194 (to J.R.) and doctoral fellowship from Fonds de Recherche du Québec (to A.R.)

Acknowledgements

We thank Brian Battersby for his help with software development.

Disclosures

The authors declare that there are no conflicts of interest related to this article.

Chapter 4

Measuring cornea mechanical properties using optical coherence elastography

The original version of this chapter was published in :

Antoine Ramier, Behrouz Tavakol, and Seok-Hyun Yun. Measuring mechanical wave speed, dispersion, and viscoelastic modulus of the cornea using optical coherence elastography. *Optics Express*, 27(12):16635, jun 2019

Abstract

Acoustic wave velocity measurement based on optical coherence tomography (OCT) is a promising approach to assess the mechanical properties of biological tissues and soft materials. While studies to date have demonstrated proof of concept of different ways to excite and detect mechanical waves, the quantitative performance of this modality as mechanical measurement has been underdeveloped. Here, we investigate the frequency dependent measurement of the wave propagation in viscoelastic tissues, using a piezoelectric point-contact probe driven with various waveforms. We found that a frequency range of 2-10 kHz is a good window for corneal elastography, in which the lowest-order flexural waves can be identified in post processing. We tested

our system on tissue-simulating phantoms and *ex vivo* porcine eyes, and demonstrate reproducibility and inter-sample variability. Using the Kelvin-Voigt model of viscoelasticity, we extracted the shear-elastic modulus and viscosity of the cornea and their correlation with the corneal thickness, curvature, and eyeball mass. Our results show that our method can be a quantitative, useful tool for the mechanical analysis of the cornea.

4.1 Introduction

Changes in mechanical properties of corneal tissues have been linked to structural and geometrical changes clinically observed in corneal degenerative diseases, such as keratoconus [8, 40, 119]. Measurement of corneal biomechanics offers opportunities for improving diagnosis and treatment of the diseases. Biomechanical characterization also has the potential to improve the accuracy of routine screening intraocular pressure (IOP) measurements by reducing errors due to variations in corneal mechanical properties [96]. Furthermore, quantitative measurement of corneal tissue stiffness could potentially improve refractive surgeries [39, 69, 86].

However, it remains challenging to measure the mechanical properties of corneal tissues quantitatively. Mechanical measurement techniques, such as strip extensometry and eye inflation tests, have been used extensively in laboratory settings, but are destructive and can not easily be applied *in vivo* [8, 41, 44, 166]. Analyzing corneal responses to air puff tonometers, such as the ocular response analyzer (Reichert) and Corvis ST (Oculus), can probe biomechanical changes in normal and pathologic eyes of live patients [77, 85, 88, 99, 128, 167], but does not provide a direct, quantitative readout of elastic modulus [31]. Ultrasound elastography has been proposed to map the stiffness of the cornea, but it has relatively low spatial resolution [66, 182]. Brillouin microscopy can map the mechanical properties of tissues with high spatial resolution [159, 162, 169], but it measures longitudinal modulus rather than shear modulus that is more directly related to tissue deformation and stiffness.

Optical coherence elastography (OCE) is an emerging technique for localized

measurements of shear elastic modulus [79, 89, 104]. Traveling-wave OCE is one embodiment of OCE, in which the propagation of mechanical waves in tissues is visualized by OCT. This is particularly well suited for the cornea with well-defined geometry and structure [7, 61, 103, 140, 190]. There is a direct theoretical relationship between complex shear wave velocity c_s and shear modulus μ :

$$\mu = \rho c_s^2 \quad (4.1)$$

where ρ is material density. Like other soft materials, the corneal tissue is viscoelastic, described by complex-valued, frequency-dependent shear modulus. As a result, c_s has frequency dependence (dispersion), and measurement of c_s at a single frequency is insufficient to describe the viscoelastic properties. Furthermore, the speed of waves propagating in the cornea is influenced by the interfaces of the cornea with the air at the anterior surface and with the aqueous humor at posterior surface. The mechanical waves traveling along the cornea are described as guided (Lamb) waves [59]. OCE described in this paper measures the phase velocity of the guided waves c . To compute c and ultimately complex-valued μ from c , it is essential to consider the geometrical effect or waveguide dispersion of the waves, together with material dispersion.

A few recent studies have reported measurements of wave dispersion in the cornea using OCE [7, 59, 61]. However, there are noticeable discrepancies among the results between different groups and different approaches. The focus of our work described here is to characterize the frequency dependence of wave velocity and its impact on elastic modulus estimation. The following sections describe experimental and analytical methods to generate, measure and analyze the mechanical wave propagation in the cornea, and to measure wave velocity over a frequency range from 0 to 10 kHz.

4.2 OCE system

Elastography measurements were performed using a home-built, swept-source OCT system previously described [142]. Briefly, this system has an A-line rate of 45 kHz,

axial resolution of 15 μm and transverse resolution of 30 μm (full width at half maximum in air) using a polygon swept laser with a tuning range of 80 nm and a center wavelength of 1280 nm. The acquisition of OCT interference fringes is phase-stabilized using the reference signal of an external Mach-Zehnder interferometer [17]. The optical beam is scanned using a two-axis galvanometer scanner (Cambridge Technology, 6210H). The noise-limited sensitivity of the system to vibration is approximately 4 nm [142].

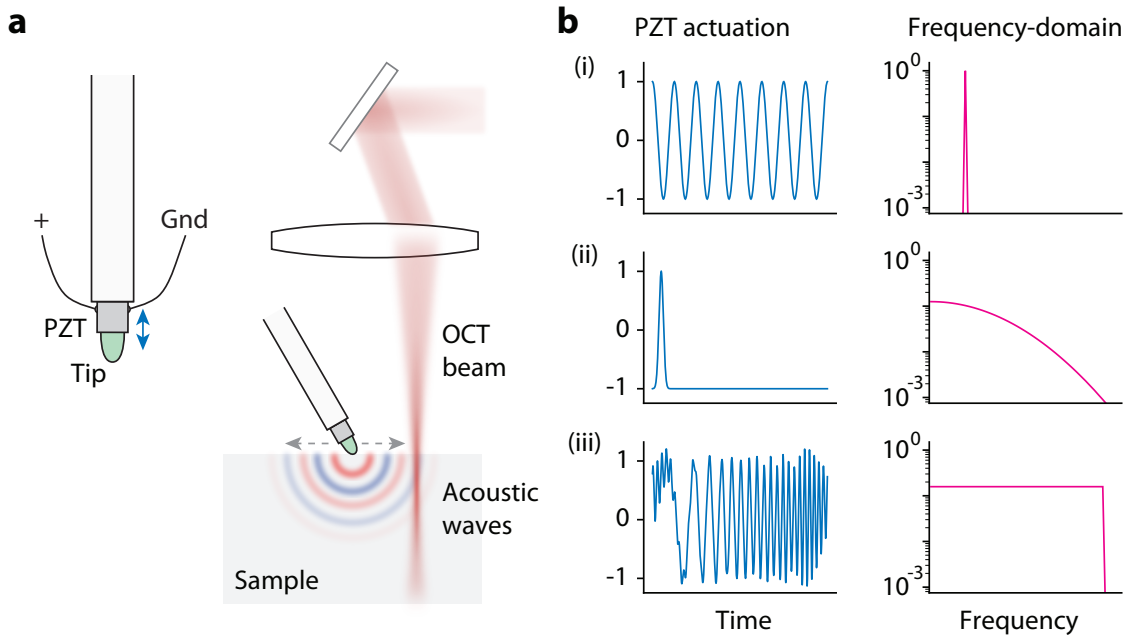


Figure 4-1: (a) Schematic of the contact probe and measurement setup. (b) Representative stimulus waveforms used in this study (left) and their frequency contents.

Mechanical stimulation was achieved using a home-built piezoelectric probe (Fig. 4-1(a)). It consists of a hemispheric ceramic tip with a diameter of 2 mm (Thorlabs, PKCESP) glued on a piezoelectric transducer (PZT) (Thorlabs, PA4CEW). The probe is mounted on a translation stage and brought to a physical contact with a sample. The broadband piezoelectric probe allows to use virtually any stimulus waveform to generate mechanical waves. Three representative waveforms are shown in Fig. 4-1(b). For a given peak-to-peak ratio, pure tones (first row) provide the maximum amount of power in an individual frequency. An impulse waveform (second row) allows broadband measurement in the frequency domain. A chirped signal (third row) provides nearly uniform, maximum power density over a broad frequency range

for a fixed peak-to-peak amplitude [123, 124, 164]. Among the three types of stimulus, the most straightforward approach is using pure tones at discrete, selected frequencies, whereas the chirp stimulus is particularly useful to obtain a continuous dispersion curve over frequency.

To utilize the full Nyquist bandwidth (22.5 kHz), the OCT system was operated in the M-B mode: m consecutive A-lines are acquired at any specific transverse location (x coordinate). Each line is formed of 1024 pixels along the z axis. At each location along the x axis, a complete time series (M-scan) is acquired for a single or repeated mechanical stimulus. Typically, each individual stimulus was 5 ms long (225 lines) and repeated 64 times to improve measurement sensitivity through averaging. After the M-scan, the OCT beam is moved to the next location along the x axis, and the measurement is repeated. A single-line scan typically comprises 96 transverse positions over a range of 10 mm. The complete resulting measurement is thus comprised of 1024 pixels along the z axis, 64 repetitions of a 5 ms stimulus, and 96 pixels along the x axis, which yields a total measurement time of approximately 30 s. The galvanometer scanners have a finite stabilization time of approximately 200 μ s, during which the mechanical jitter of the scan mirror causes spurious phase fluctuations in the OCT signal. To circumvent this problem, A-lines obtained during this transient period were simply ignored in post-processing.

4.3 Data processing and validation using an elastomer

4.3.1 Displacement field

A Fourier transform of raw OCT interferometric data from the optical wavenumber domain to axial position (z), repeated for each time (t) of A-line and lateral (x, y) point, produces a complex OCT tomogram $A(\mathbf{r}, t)$, where $\mathbf{r} = (x, y, z)$. The magnitude of this multidimensional array, typically in log scale, produces structural OCT images. The phase $\phi(\mathbf{r}, t)$ of the complex $A(\mathbf{r}, t)$ is used to compute the axial component of

the displacement field $u_z(\mathbf{r}, t)$ using the following set of equations:

$$\Delta\phi(\mathbf{r}, t_i) = \arg \left(\sum_{\mathbf{r} \in \text{ROI}} A^*(\mathbf{r}, t_{i-1}) A(\mathbf{r}, t_i) \right) \quad (4.2)$$

$$\phi(\mathbf{r}, t_k) = \sum_{i=1}^k \Delta\phi(\mathbf{r}, t_i) \quad (4.3)$$

$$u_z(\mathbf{r}, t_k) = \frac{\lambda_0}{4\pi n_m} \left(\phi(\mathbf{r}, t_k) + \phi(\mathbf{r}_{\text{surf}}, t_k) \frac{n_m - n_0}{n_0} \right) \quad (4.4)$$

where ROI is a small neighborhood around \mathbf{r} , λ_0 is the average free-space wavelength of the OCT beam, n_m and n_0 are the refractive indices of the sample medium and the air above the sample, respectively, and $\phi(\mathbf{r}_{\text{surf}}, t)$ is the phase at the air-sample boundary. Note that although the displacement field $\mathbf{u}(\mathbf{r}, t)$ is a vector quantity, phase-sensitive OCT can only detect its component along the optical beam $u_z(\mathbf{r}, t)$.

To visualize wave propagation along the transverse coordinates, a z -projection of the displacement field was used. First, the top sample surface is identified using an automatic segmentation algorithm (or manually when the algorithm failed in low SNR portions of the images). Then, a ± 5 pixels window around the top surface is defined and the signal in the region is summed (Eq. (4.2)). This step acts as brightness-weighted averaging of the displacement field.

Figure 4-2 shows the projected displacement field measured in an elastomer sample obtained with three different stimulus waveforms. The tissue-simulating silicone rubber phantom was prepared by mixing part A and part B precursors (Smooth-On Inc., EcoFlexTM 00-10) with a 1:1 volume ratio and casting the mixture onto a cylindrical container with a diameter of 10 cm and a height of 5 cm. The sample was removed from the mold after curing overnight. Mechanical waves are launched at the contact with the PZT probe and propagate radially in the surface of the homogeneous medium. The magnitude of the displacement is about 100 nm at the origin and decreases with r . It is clearly seen from the single-tone profiles that, as the frequency increases, the attenuation increases and the wavelength decreases. As a result, the number of detectable wavelengths is nearly constant (about 2-3 full cycles).

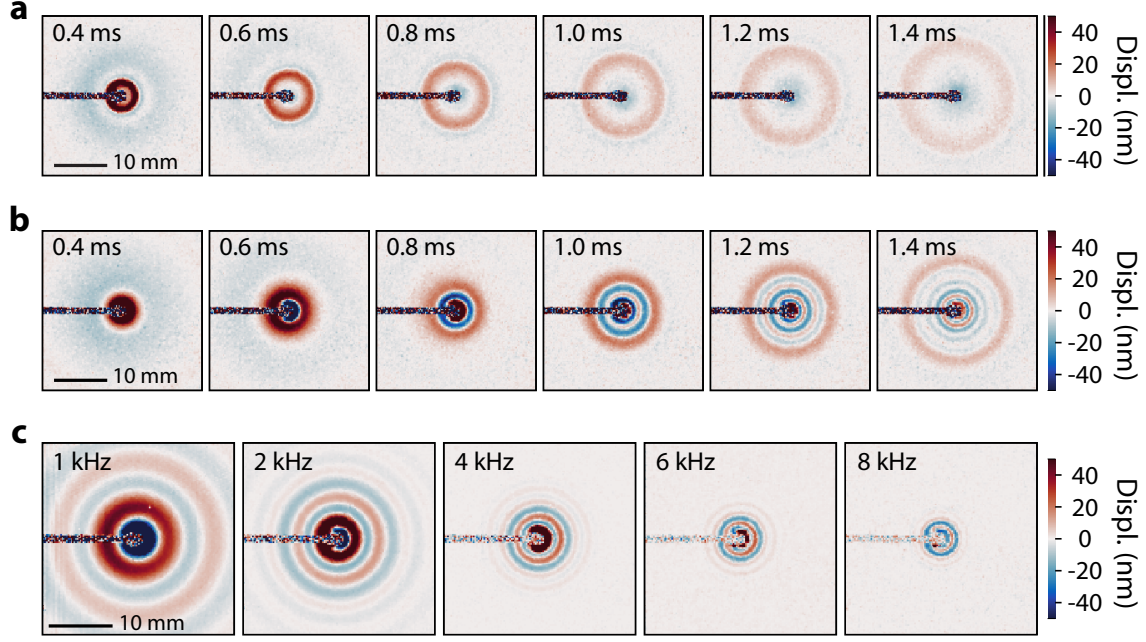


Figure 4-2: Displacement field of elastic waves at the surface of an elastomer phantom for different waveforms. (a) Several time frames selected from a full data set for single 100 μ s-long Gaussian impulse stimulus. (b) Corresponding time frames for a Schroeder-type chirp [164]. (c) Snapshots for pure tones at 1, 2, 4, 6, and 8 kHz, respectively.

4.3.2 Dispersion measurement

From the measured displacement field, the wave velocity is calculated via a couple of Fourier transform steps. Briefly, a two-dimensional (2D) Fourier transform of the displacement field (time t to frequency f and distance r to wavenumber k) produces a dispersion relation $k(f)$ in the f - k plane. The phase velocity c is obtained from $c = 2\pi f/k$. For a chirped tone or any arbitrary stimulus waveform, the processing is identical to an impulse stimulus except that an additional step is needed to compute a cross-correlation function.

In Figure 4-3, we illustrate more detail of the data processing using actual experimental data acquired with a chirp stimulus (0-10 kHz bandwidth) on the isotropic, semi-infinite elastomer sample. We show intermediate steps in Figs. 4-3(b)-4-3(d) to illustrate the principle of data processing. However, in practice, one can skip these steps and move directly to the f - k domain (Fig. 4-3(e)) using a 2D Fourier transform

of the raw data in the t - x domain (Fig. 4-3(a)).

Figure 4-3(a) displays the measured displacement field at the top surface of the sample (e.g. Fig. 4-2(b)) in the t - r space: $u_z(r, t)$, where r denotes the propagation distance from the center of the vibrating tip along the surface. In this experiment, the data was obtained using a line scan along the x axis, so $r = x$. For the cornea, we note that r would be defined along the curved surface.

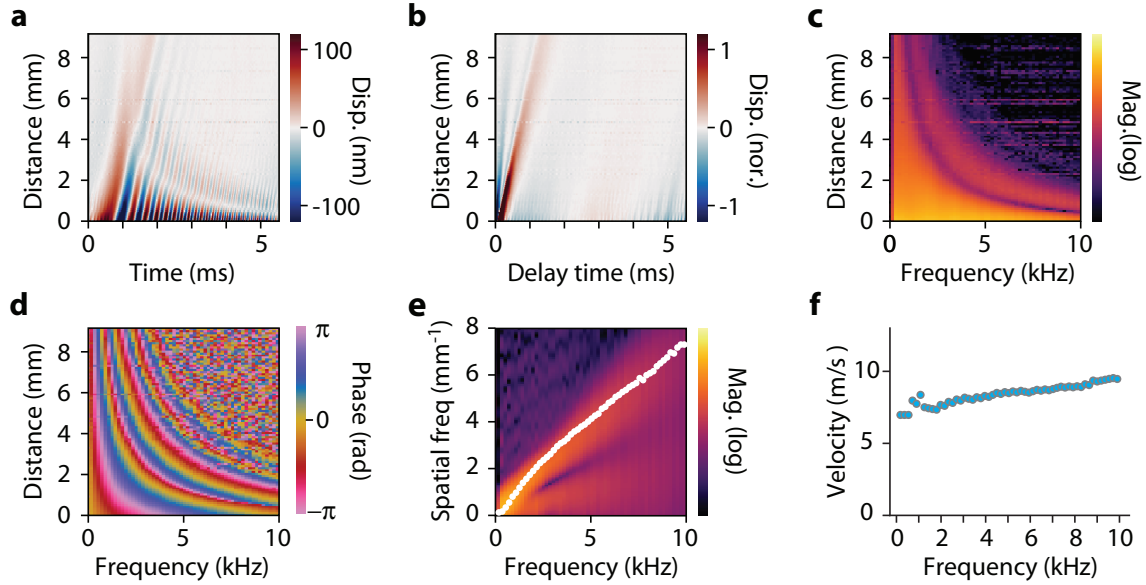


Figure 4-3: Processing steps to compute the mechanical wave dispersion of a sample applied to a tissue-simulating phantom. (a) Displacement field as a function of the time and transverse propagation distance (t - r plane). (b) Impulse response calculated from cross-correlation with the stimulus waveform. (c-d) A Fourier transform of the cross-correlation function over time, showing the magnitude, (c), and phase, (d), in the f - r plane. (e) Magnitude of the Fourier transform of the Fourier-domain cross-correlation function over space, revealing the dispersion curve of the lowest-order guided wave (bright curve). (f) Phase velocity obtained from the dispersion map as a function of frequency.

The chirped displacement signal can be compressed to an impulse-like waveform using a cross-correlation operation:

$$\gamma_{u,s}(r, \tau) = u_z(r, t) \star s(t), \quad (4.5)$$

where τ is a time delay variable, \star denotes the correlation operation, $s(t)$ is the

stimulus waveform, and $\gamma_{u,s}$, is the cross-correlation between u and s . This step makes the chirp approach equivalent to the impulse response measurement, but offers an advantage of enhanced signal-to-noise ratio (for a given peak mechanical displacement) because the power in the chirp is distributed over a longer period of time. This strategy is commonly used in radar imaging [82], and was recently proposed in the context of traveling-wave OCE [124]. There are several options to use as the reference waveform $s(t)$. It can be either the displacement of the unloaded vibrating probe tip measured using the OCT, the displacement field measured at some reference point in the sample (alternatively, other reference material), or simply the voltage waveform applied to the probe if the frequency response of the device is sufficiently flat. We have found that these three options yielded identical results in practice. Figure 4-3(b) shows the calculated cross-correlation $\gamma_{u,s}(r, \tau)$, illustrating the equivalence between the chirp and impulse stimuli.

The Fourier-domain function of the cross-correlation field (or the displacement field for the case of impulse stimulus) is given by

$$\Gamma_{u,s}(r, f) = U_z(r, f) S^*(f), \quad (4.6)$$

where $\Gamma_{u,s}$, U_z , and S are the Fourier transformations of $\gamma_{u,s}$, u_z , and s , respectively, and $*$ denotes complex conjugation. The magnitude and phase of the cross-spectrum $\Gamma_{u,s}(r, f)$ are plotted in Figs. 4-3(c) and 4-3(d). We highlight that, in practice, we performed the correlation operation in the frequency domain using Eq. (4.6), which implicitly enforces the periodicity of each time series and naturally describes the repeated stimulus of our M-B scan acquisition configuration.

The patterns in the $f\text{-}r$ plane appear to follow hyperbolic curves suggesting that $\Gamma_{u,s}$ is a function of $\sim fr$. In other words, the magnitude and phase are approximately constant for a given $f \cdot r$ product. This behavior is expected for the phase considering that the equi-phase contours of a non-dispersive plane wave $u_z \sim e^{ikr}$ would be given by $\varphi = kr = (2\pi/c)fr$. Any deviation from the hyperbolic relation is due to dispersion. The hyperbolic relation of magnitude indicates the frequency dependence

in attenuation. In fact, the attenuation coefficients of compression and shear waves in soft viscoelastic materials, including tissues, have been measured to increase nearly linearly with frequency in the ultrasonic frequency range [102, 193].

Careful inspection of the impulse response plot (Fig. 4-3(b)) reveals that the mechanical stimulus excites not only the main Rayleigh-type wave (red), but also a weaker, faster-traveling wave (blue) that is out of phase with the main wave. A detailed investigation of the origin of the fast waves is outside the scope of this article. It is important to notice that the interference of the fast wave with the main wave shows up in the amplitude and phase of the Fourier-domain correlation function (Figs. 4-3(c) and 4-3(d)). In previous studies, the frequency-dependence of corneal wave velocity was calculated using the slope of the phase profile over distance [7, 61, 190]. However, we found that this method becomes unreliable, particularly at frequencies above 5 kHz because the interference causes the phase profile over distance to become nonlinear. The nonlinear slope yields position-dependent velocities even in homogeneous materials. When the amplitude of the fast wave is comparable with or greater than that of the main wave, the wave velocity can be greatly overestimated.

Our solution to this problem is to perform a second Fourier transform along the spatial axis (transforming distance r to spatial frequency or wavenumber k). The result is shown in Fig. 4-3(e). The magnitude of the Fourier transform in the f - k plane reveal the dispersion curves $k(f)$ of all wave components. The main wave component can be tracked using a simple bounded max search at every frequency and separated from other waves. Zero-padding by a factor 8 was used in the Fourier transform so that the maxima could be found with greater accuracy.

Finally, the phase velocity $c = 2\pi f/k$ is obtained from the dispersion curve. The result is plotted in Fig. 4-3(f). In principle, the group velocity can also be obtained from the local slope of the dispersion curve. Again, we note that the dispersion curve (Fig. 4-3(e)) can be directly computed as

$$\Gamma_{u,s}(f, k) = U(f, k) S^*(f), \quad (4.7)$$

where $U(f, k)$ is the 2D Fourier transform of the displacement, and $S^*(f)$ is the complex-conjugate Fourier transform of the reference stimulus waveform.

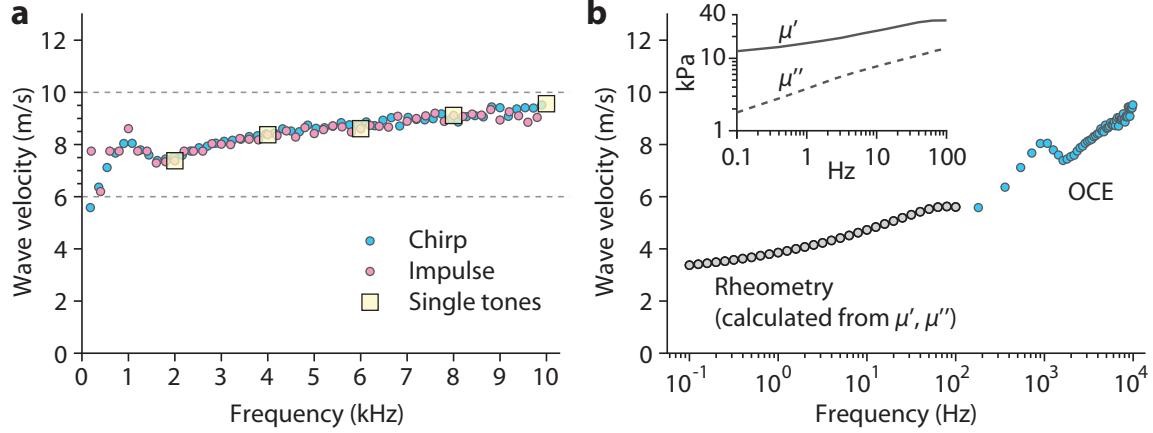


Figure 4-4: (a) Measured phase velocity of silicone rubber using three different stimulus waveforms: chirp (Schroeder-type [164], with frequency components between 0 and 10 kHz by steps of 180 Hz), impulse (Gaussian-shaped with a 4σ pulse length of 100 μ s), and single tones at frequencies 2, 4, 6, 8 and 10 kHz. (b) Comparison to wave speeds measured by rheometry in a low frequency range of 0.1-100 Hz. Inset, complex shear modulus measured using a commercial shear rheometer.

To evaluate the fidelity of the measurement, we measured the wave velocity using an impulse stimulus and pure tones at several discrete frequencies. All the results are plotted in Fig. 4-4(a). We can see that the data obtained with the chirp (cyan circles) are consistent with those obtained using a short 100 μ s Gaussian pulse (magenta circles). The chirp stimulus tends to allow slightly less noisy readings due to the improved signal to noise ratio. We also verified that both approaches based on broadband stimuli produce the same results with pure tones (yellow squares). This equivalence is expected for linear materials, which is a reasonable assumption for low amplitude waves traveling in viscoelastic materials. The measurement data at frequencies below 2 kHz have some apparent noise or artifact mainly due to the fast waves that were not well separated in the f - k plane and therefore not completely removed. The data in 2-10 kHz show high fidelity. In this high frequency range, the measured velocities increase from ~ 7.4 to 9.6 m/s. The frequency dependence is attributed to the material dispersion of the elastomer. The waveguide dispersion is negligible because the 5 cm thickness of the sample is much greater than the wavelength in the frequency range

(3.7 mm at 2 kHz to 0.96 mm at 10 kHz). In this regime, the lowest-order Lamb waves propagate along the surface, known as the Rayleigh surface wave.

Standard mechanical test equipment is operated at lower frequencies below 100 Hz. Therefore, validation of our measurement is not straightforward. As indirect assessment, we measured the shear storage modulus (μ') and loss modulus (μ'') of the elastomer material using a commercial shear rheometer (AR-G2, TA Instruments) in the frequency range of 0.1 Hz and 100 Hz. The data is shown in Fig. 4-4(b). Using the measured complex shear modulus, $\mu = \mu' + i\mu''$ and Eq. (4.1), we obtain the complex bulk shear speed. The real-part phase velocity is given by $c = 1/\text{Re}(c_s^{-1})$ [79], which can be expressed as:

$$c = \sqrt{\frac{|\mu|}{\rho}} \sqrt{\frac{2}{1 + \cos \delta}}, \quad (4.8)$$

where $|\mu| = \sqrt{\mu'^2 + \mu''^2}$ and $\tan \delta = \mu''/\mu'$. The Rayleigh surface wave in incompressible materials has a velocity $c_R \approx 0.955 c_s$. We calculated the Rayleigh wave phase velocity from the rheometer data and plot the result in Fig. 4-4(b), along with the OCE data. The two sets of data are connected remarkably well, indirectly supporting the accuracy of our OCE measurement. As described above, the rapid frequency dependence in the OCE data at 0.2-2 kHz is likely an artifact due to fast-traveling waves.

4.4 Elastography of the cornea

4.4.1 Displacement field and dispersion

Figure 4-5(a) shows a schematic of the setup for corneal elastography. Porcine eyes (10 pairs) were obtained less than 8 h postmortem, and connective tissues such as fat, muscles and the optic nerve were dissected out for consistent boundary conditions and weight measurements. After placing an eye in a custom-made holder mounted on a manual 3-axis positioning stage, the IOP is set to 15 mmHg using a water column. When the IOP is stabilized, the eye is aligned with the OCT beam, and the PZT probe is brought to the eye about 4 mm away from the corneal apex. After the probe

tip makes a contact with the corneal epithelium, it was gently advanced by $\sim 100\text{ }\mu\text{m}$ further to ensure the mechanical contact to be maintained during stimulus actuation. Experiments were performed on a total of 20 eyes (10 pairs).

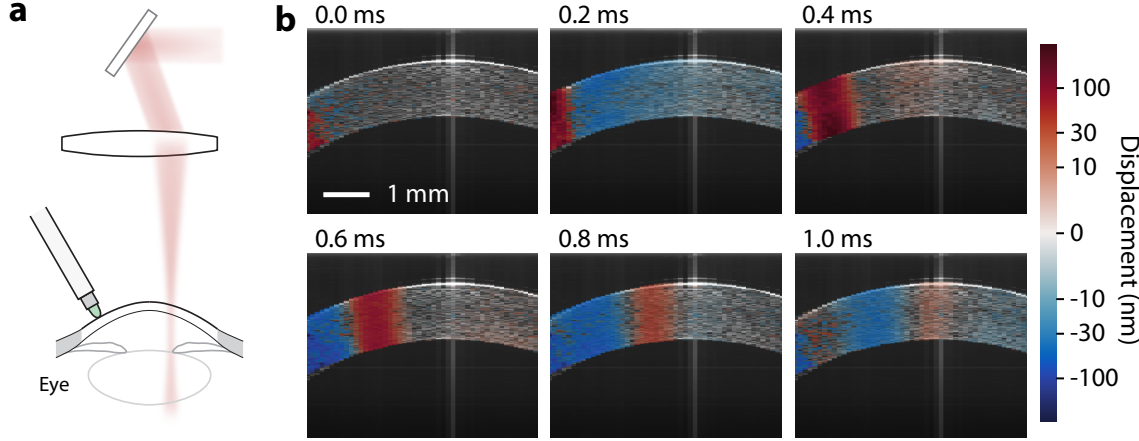


Figure 4-5: (a) Schematic of elastography experiment performed on a porcine eye. (b) Time-dependent displacement field in the cornea from an impulse stimulus. The displacement field is overlaid over the standard OCT intensity image.

Figure 4-5(b) shows the vibrography images of the cornea in response to an 0.1-ms-long impulse stimulus. At the onset (0 ms), the downward (positive displacement) movement initiates from the point of contact and propagates along the corneal tissue. The displacement field is quite uniform across the depth of the cornea, indicating the guided wave is predominantly the lowest-order, anti-symmetric (flexural) Lamb wave. At 1 ms, the leading edge (red region) of the wave reaches the corneal apex 4 mm away from the probe tip (i.e. $c \approx 4\text{ m/s}$).

We acquired OCE dataset using the same chirp waveform and processing steps described in Section 4.3. Figure 4-6 shows the measured displacement field in the $t-r$ domain, the magnitude of the cross-correlation function in the $f-r$ domain, and the dispersion map in the $f-k$ domain. Two dispersive branches are apparent in Figs. 4-6(a) and 4-6(c), corresponding to the lowest-order Lamb wave and a fast wave, respectively. The resulting interference patterns are visible in Fig. 4-6(b). The identity of the fast wave(s) is not well understood but is thought to come from the excitation of compression waves, which have bulk velocities of $\sim 1620\text{ m/s}$ in the cornea [169] and $\sim 1540\text{ m/s}$ in the aqueous humor, and possibly also from high-order guided

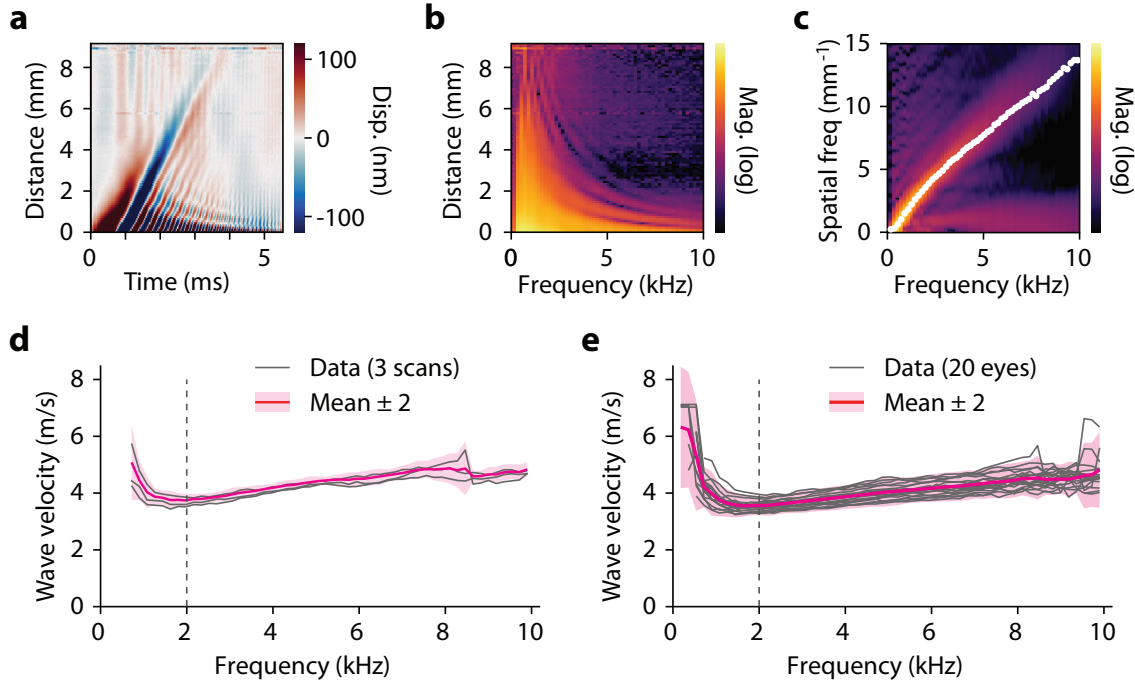


Figure 4-6: Phase velocity measurement of porcine corneas at the same IOP level of 15 mmHg. (a) Displacement field. (b) Cross-spectrum magnitude. (c) Dispersion map obtained by a 2D Fourier transform of the displacement field. (d) Frequency-dependent phase velocity of the same porcine cornea measured 3 times. (e) Frequency-dependent phase velocity of 20 different porcine eye samples.

waves. The dispersion curve of the dominant Lamb wave (bright curve) was isolated and used to compute the phase velocity dispersion of the cornea.

Figure 4-6(d) shows the velocity dispersion data obtained from a single eye, measured 3 times. Between each measurement, the eye was removed from the holder and put back in place, and the contact of the PZT probe was re-established, introducing substantial difference in the contact position and OCT scan line. The result demonstrates a good repeatability of measurement with a standard deviation of $\pm 3.9\%$.

Figure 4-6(e) shows the velocity dispersion curves for all of the 20 measured eyeballs. The data show an inter-sample variation of $\pm 7.2\%$ in wave velocity for the porcine eyes at a constant IOP. Besides the small quantitative differences, all the curves show common features. At low frequencies below 1.5 kHz, the velocity increases with decreasing frequency. We believe this is an artifact due to the finite size of the

cornea. We will discuss it more later. At higher frequencies above 2 kHz, the velocity linearly increases with frequency. In the following section, we analyze this frequency range to extract viscoelastic properties of the corneal tissue.

4.4.2 Viscoelasticity

One promising approach to extract the biomechanical parameters of corneal tissue is to fit the phase velocity dispersion curves with those predicted by a Lamb-wave waveguide model, such as the modified Rayleigh-Lamb model combined with a viscoelastic material model such as the Kelvin-Voigt (KV) model [61, 121]. This approach has been applied to data obtained with air puff stimuli with narrowband frequency contents below 1 kHz [61]. To good approximation, the cornea can be modeled as an infinite, flat plate with a thickness h and density ρ , bounded by the air (or vacuum) on the top surface and water at the bottom surface. The material properties are assumed to be isotropic and homogeneous. The shear modulus in the Kelvin-Voigt model is described as [113]:

$$\mu(f) = \mu_0 + i(2\pi f)\eta, \quad (4.9)$$

where the real part μ_0 corresponds to shear modulus at zero frequency ($\mu = \mu_0$ at $f = 0$), and the imaginary part originates from shear viscosity η . The bulk shear wave phase velocity is given by [79]:

$$c = \sqrt{\frac{\mu_0}{\rho}} \sqrt{\frac{2\zeta^2}{\zeta + 1}}, \quad (4.10)$$

where $\zeta = \sqrt{1 + (2\pi f \eta / \mu_0)^2}$.

The traveling-wave analysis in OCE described here measures the complex wavenumber k of the wave, whose real part defines the wave velocity c and imaginary part describes the wave attenuation α . Applying the surface boundary conditions to the elastodynamic wave equation yields a 5 by 5 matrix equation whose determinant must be zero for guided waves (see equation 17 of reference [61]). In Fig. 4-7(a), we

show a computational result of this model for $h = 0.8$ mm, $\rho = 1$ g/cm³, $\mu_0 = 25$ kPa, $\eta = 0$, and $\lambda = 2.2$ GPa. By taking $\eta = 0$, the result is consistent with the well-known dispersion curves of various Lamb modes in isotropic, elastic plates. The modes are labeled as either quasi-antisymmetric (A_n) or quasi-symmetric (S_n), where the index n indicates the order of the mode. Due to the presence of different media at the top and bottom boundaries, the modes do not have pure odd or even symmetry. At low frequencies, the fundamental branch A_0 represents the flexural plate wave. At high frequencies, it asymptotically transforms to become the Scholte wave with a velocity $c_{\text{Sch}} \approx 0.846 c_s$, which is a surface wave traveling at the cornea-fluid interface [79]. The S_0 branch becomes the Rayleigh surface wave traveling the cornea-air boundary at a velocity $c_{\text{Ray}} \approx 0.955 c_s$ at high frequencies, whereas the other branches tend towards the bulk shear wave velocity.

We fitted the A_0 -mode wave solution to the average phase velocity curve in the 2-10 kHz range obtained from the 20 porcine cornea samples, using μ_0 and η as the only two free parameters and the trust-region-reflective least-square algorithm. The result is shown in Fig. 4-7(b), where the best fit was obtained with $\mu_0 = 20.5$ kPa and $\eta = 0.28$ Pas. We found that the model and the data agree well over the fitting range. The positive slope in phase velocity is accounted for by viscous damping.

To determine the precision of μ_0 and η values, we have run the fitting calculation 100 times using different initial guess values of μ_0 randomly chosen between 10 and 50 kPa and of η between 0.05 and 0.45 Pas. The fitting algorithm converges to a slightly different solution depending on the initial guess. The distribution of solutions in the μ_0 - η space is shown in Fig. 4-7(c). When the entire data set in the 2-10 kHz range was used, the analysis yields a narrow distribution with standard deviations of <10% for both μ_0 and η . However, partial data for narrower frequency ranges produce more inaccurate estimation, especially for η . Note that the distributions of μ_0 and η are not independent. This result highlights that broadband excitation stimulus is necessary for measuring both the stiffness and viscosity from velocity dispersion.

The wave attenuation coefficient α can also be obtained from the KV model using

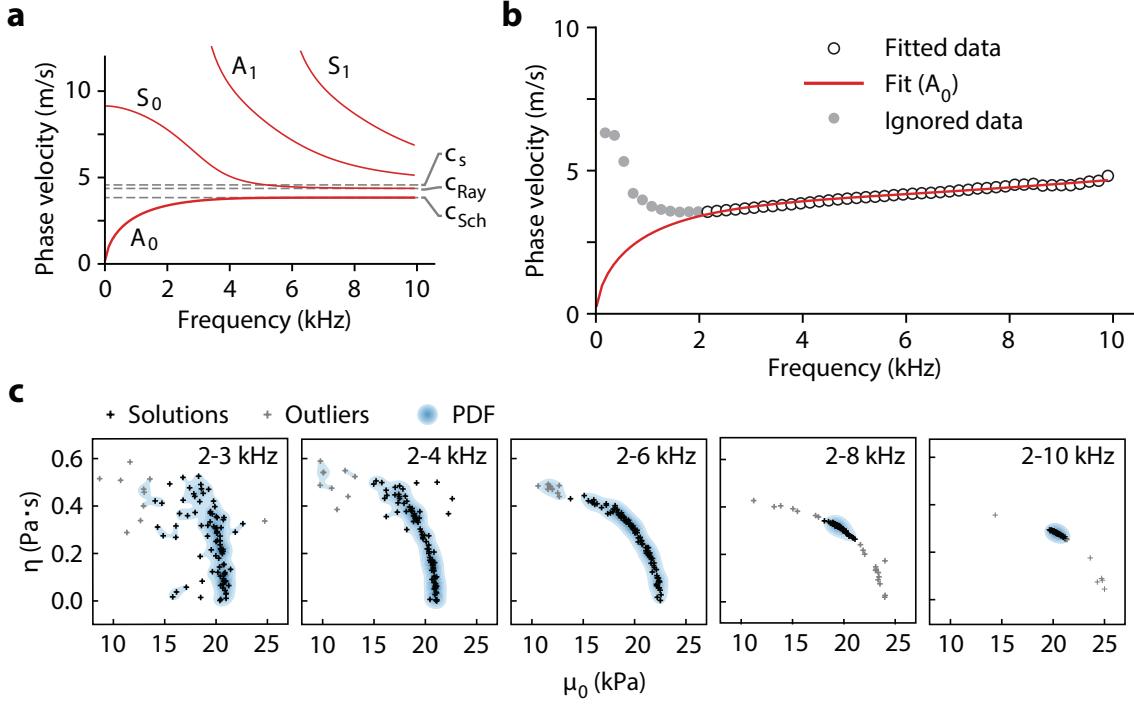


Figure 4-7: Parameter estimation using the Lamb wave model. (a) Example Lamb wave spectrum for typical porcine cornea properties, neglecting viscosity. (b) Lamb wave model fitted to the measured porcine cornea phase velocities. (c) Fit error estimation using the initial guess variation method. Each marker represents the fit results for a different set of initial guess parameters. Probability density function (PDF) contours are also shown to help visualization. Each panel uses a different frequency ranges for fitting.

the following equation [79]:

$$\alpha = 2\pi f \sqrt{\frac{\rho}{\mu_0}} \sqrt{\frac{\zeta - 1}{2\zeta^2}} \quad (4.11)$$

We measured the attenuation of the displacement field at each frequency by fitting a decaying exponential to the magnitude expressed as a function of r . The $1/r$ -type diffraction loss was taken into account by scaling the amplitude by \sqrt{r} prior to fitting. The attenuation value obtained is shown in Fig. 4-8 for each of the 20 porcine corneas as grey lines and with the mean and 2-standard-deviation statistics shown in green. The measured attenuation in the range of 0-4 kHz compares well with the near-quadratic frequency-dependence predicted by Eq. (4.11) for $\mu_0 = 20.5$ kPa

and $\eta = 0.28 \text{ Pas}$ (dotted red line in Fig. 4-8). To account for waveguide loss, we solved the Lamb wave characteristic equation using the KV-model material property and calculated attenuation from the complex propagation constant (solid red line in Fig. 4-8). The reasonably good correspondence in the 0-3.5 kHz range supports the validity of our analysis based on the KV and Lamb wave model. There is a small offset of $\sim 0.15 \text{ mm}^{-1}$ between the data and theory, which may be attributed to the deviations of the cornea from the KV and Lamb models. Note that because the attenuation was measured in the f - r , rather than f - k , domain, the interference of the fast waves was not filtered out, resulting in unreliable attenuation measurement in 4-10 kHz.

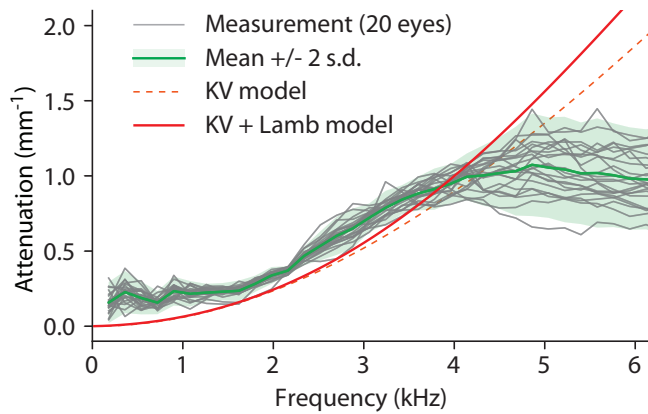


Figure 4-8: Wave attenuation measurement of porcine corneas as a function of frequency. Gray lines represent the measured wave attenuation data for each of the 20 porcine eyes at an IOP of 15 mmHg, measured by fitting an exponential decay function to the wave magnitude at each frequency. Green line and shaded region represent the mean and 2 standard deviation error. The solid red curve represents the attenuation predicted by the KV and Lamb models with $\mu_0 = 20.5 \text{ kPa}$ and $\eta = 0.28 \text{ Pas}$ previously obtained. The dotted line represents the attenuation in the absence of waveguiding as predicted by Eq. (4.11).

4.4.3 Correlation of wave velocity with anatomical parameters

Figure 4-9 shows the distribution of shear modulus across the 20 eyes, plotted as a function of the eyeball weight, central corneal thickness, and central anterior radius of curvature. Left and right eyes of the same animal are represented with left- and

right-pointing triangles of matching color in Figs. 4-9(a)-4-9(c), and are plotted against each other in Fig. 4-9(d). We found rather strong negative correlation with the weight (Pearson's $r^2 = 0.56$) and mild to weak correlation with the curvature ($r^2 = 0.11$). The origin of the clear weight dependence could be physiological, but other weight-dependent geometrical effect might have contributed via waveguide dispersion [60]. We found no correlation between shear modulus and corneal thickness ($r^2 = 0.048$), which is expected given that the Rayleigh-Lamb model takes into account the effects of thickness on wave velocity. Other parameters influencing thickness, such as corneal swelling, could potentially be appreciated, but the relatively narrow range of corneal thicknesses and the absence of significant correlation suggests that this parameter was adequately controlled during our experiments. Comparison between the left and right eye showed a moderately strong correlation ($r^2 = 0.29$) with a slope close to unity (dotted black line, Fig. 4-9d).

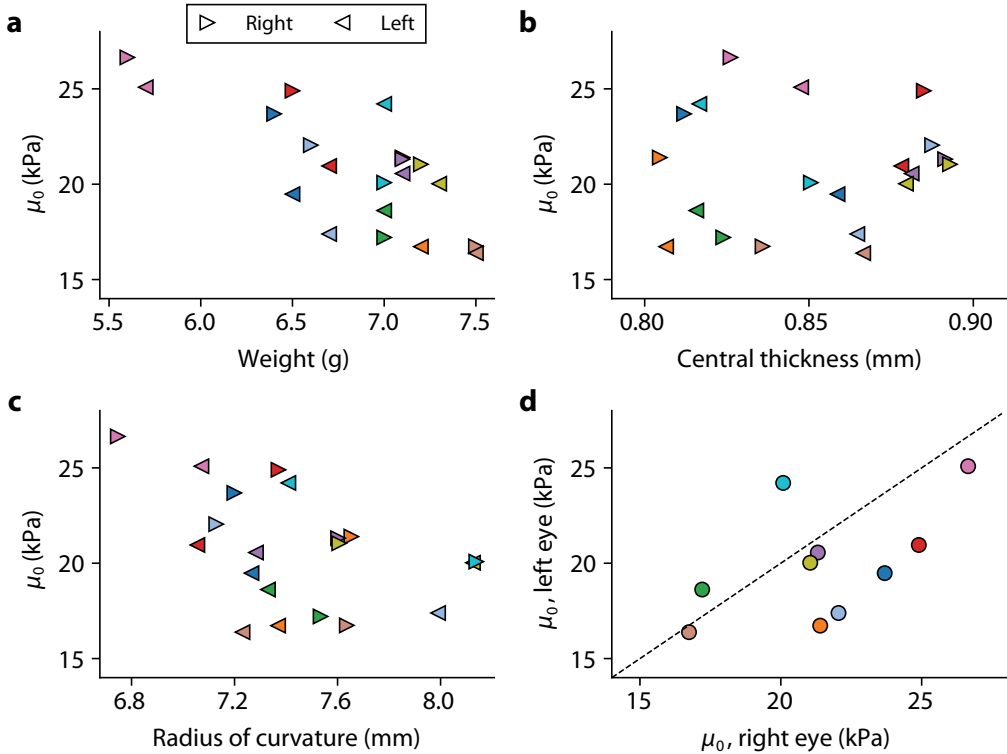


Figure 4-9: Measured static shear modulus, μ_0 of 10 pairs of porcine eyes (20 eyes) as a function of (a) weight, (b) central corneal thickness (CCT), and (c) anterior corneal radius of curvature. (d) Comparison between the left and right eyes of matching pairs.

4.5 Discussion and conclusion

We found that PZT-based OCE is well suited to generate and measure the propagation of broadband mechanical waves in samples, with advantages of the wide bandwidth, flat frequency response, and low-cost of piezoelectric actuators. Using this technique, we have measured the phase velocity dispersion, stiffness, and viscosity of porcine corneas with high fidelity, although we do not have alternative, gold-standard values to validate the data quantitatively. For clinical applications, non-contact approaches such as air puffs and acoustic radiation force [6, 191] are appealing. However, using local anesthetics, contact with the cornea is a well tolerated medical procedure used in tonometry, pachymetry, and some embodiments of OCE [32]. The PZT-based contact probe may also be a useful tool for other potential applications of OCE in dermatology and other medical areas, as well as laboratory measurement.

Our result indicate that 2-10 kHz is a suitable frequency window for traveling-wave OCE for the cornea. Below 2 kHz, the data deviates strongly from the A_0 branch of the theoretical model, as previously observed [7]. It appears unlikely that this is the signature of the S_0 mode, because the velocity dispersion and the spatial pattern of displacement field deviate from those of the symmetric mode. One possible explanation is that low frequency excitation is susceptible to excite resonance modes of the cornea or the whole eyeball [1]. Resonance modes are standing waves, making them appear to have infinite wave velocity. These fast waves interfere in the phase velocity analysis, causing overestimation of the shear wave velocity. While the f - k domain processing approach proposed here is designed to reject these waves, it is less effective when multiple branches overlap at low frequency below 2 kHz for the cornea. Another explanation is that at frequencies below 1 kHz, the wavelength becomes comparable with the size of the cornea. The wave propagation could therefore be more influenced by any inhomogeneity in the mechanical properties of the cornea and reflection from the cornea-sclera interface.

Fitting the velocity dispersion with the A_0 wave is only an approximation. In principle, the contact stimulus on the surface could excite a combination of multiple

modes including the S_0 and higher order A and S modes in the far field if the excitation frequency is above their cutoffs. In the near field, an infinity of complex modes are also required to fully describe the wave field in the vicinity of the source, where the bulk shear and compression waves have not yet developed into true guided waves. Our f - k domain approach can separate the different wave components if the propagation distance is long enough, but this is often not the case due to viscous damping and the finite extent of the cornea itself. Furthermore, the wave velocity is similar between the A_0 and S_0 modes above 5 kHz. The Lamb wave model also neglects the effects of IOP-induced stress, corneal curvature, anisotropy, and inhomogeneity of the material properties, resulting in biased estimations of shear modulus and viscosity [60].

In the KV model, we calculate a 10-dB attenuation distance of the shear wave, L , defined as the propagation distance over which the displacement decreases to 10%:

$$L = \frac{\ln 10}{\alpha}, \quad (4.12)$$

The ratio of L to the wavelength $\lambda = c/f$, or the number of wave cycles ($N = L/\lambda$) within the effective propagation distance is:

$$N = \frac{\ln 10}{2\pi} \sqrt{\frac{\zeta + 1}{\zeta - 1}}, \quad (4.13)$$

If we impose $N > 1$ as a necessary condition for reliable measurement, we get $\zeta < 1.31$, which is $(2\pi f \eta) < 0.85\mu_0$. For porcine corneas, using our measurement data of $\mu_0 = 20.5$ kPa and $\eta = 0.28$ Pa s, we find the high-frequency limit to be 9.9 kHz. Although the 10-dB attenuation distance is somewhat arbitrary and will depend on the sensitivity of the instrument and the magnitudes of spurious fast waves, our empirical experience suggests that this condition is reasonable. Another difficulty encountered at higher frequencies above 10 kHz is low displacement amplitude, which for a fixed power, decreases with frequency.

The above criteria for optimal frequency ranges imply an important condition for samples. For highly viscous samples, the high-frequency limit would come down to a

lower value. When this value is lower than the low-frequency limit imposed by the size of the sample, the traveling-wave analysis would not yield reliable measurement, and different algorithms may be needed to extract both the elastic and viscous properties.

The shear modulus values of porcine corneas we measured are comparable with previous values measured by other OCE techniques using air puff [59, 61] and acoustic radiation force [7], as well as ultrasound elastography [182]. There are discrepancies of up to a factor of two among reported values, part of which could be attributed to differences in wave frequency, IOP, processing algorithm, and tissue models (e.g. linear elastic).

In summary, this study describes the generation and measurement of broadband mechanical waves in the cornea to characterize the phase velocity dispersion in the cornea and estimate its viscoelastic material parameters. Our results suggest that a wide frequency band improves the accuracy of elasticity and viscosity estimation by fitting the phase velocity with a Lamb wave model. This research shows that the combination of phase-sensitive OCT vibration sensing with a piezoelectric actuator is a promising approach to measure the mechanical properties of the cornea and other samples.

Funding

National Institutes of Health (NIH) (P41-EB015903, R01-EY025454); National Science Foundation (NSF) (CMMI-1562863)

Acknowledgments

The authors wish to thank Dr. Zeinab Hajjarian for her help with rheometry measurements and Prof. Laurent Demanet for helpful discussions.

Disclosures

The authors declare that there are no conflicts of interest related to this article.

Chapter 5

Mechanical characterization of the human cornea *in vivo* using optical coherence elastography

Abstract

We demonstrate the use of optical coherence tomography (OCT) to perform quantitative measurements of the in-plane shear-elastic modulus of the human cornea *in vivo*. The proposed approach is based on measuring the velocity of mechanical waves in the upper range of the audio frequency band. The acoustic waves are generated using a custom-designed vibrating probe, and wave propagation is then tracked using phase-stabilized swept-source OCT. We conducted a pilot study on 13 healthy volunteers aged between 25 and 67. Wave velocity across subjects ranged between 6.6 and 8.9 m/s, with an average of 7.85 m/s, corresponding to an in-plane shear modulus of 68 kPa. No significant correlation was found between wave velocity and intraocular pressure (IOP) and central corneal thickness (CCT) within normal range. We found a small but statistically significant decrease in wave velocity as a function of age (-3.2 ± 1.7 m/s/100 years). Our experimental results and our analysis of the cornea microstructure suggest that the in-plane tensile stiffness and in-plane shear stiffness

are dominated by different components of the stiffness tensor, which are governed by different physiological processes. We propose that in-plane shear rigidity is mostly controlled by the mechanical properties of the interlamellar and interfibrillar matrix, whereas tensile strength is dominated by the properties of the fibrils themselves.

5.1 Introduction

The cornea is the anterior part of the eye and is responsible for about two thirds of its total refractive power. The ability of the cornea to focus light and form a sharp image on the retina requires it to precisely maintain a nearly spherical shape, which is achieved by maintaining the cornea under tensile stress from the presence of intraocular pressure (IOP). The effectiveness of this mechanism relies on a fine balance in the corneal mechanical properties, which must be flexible enough to form a smooth curved surface, resistant enough to protect from external trauma, and highly stable to maintain its shape under IOP load.

As a consequence, corneal biomechanics plays important roles in many physiological processes of clinical significance. It is now widely accepted that corneal biomechanics are involved in corneal ectatic disorders such as keratoconus and post-lasik ectasia [5, 56, 152, 187]. Early detection and screening is increasingly recognized as important in the management of keratoconus [107]. Biomechanical measurement could open up new avenues for diagnosis and help assess the probability of ectasia progression. Finally, such measurements could help improve the accuracy of routine IOP measurements [96], and reduce the incidence of residual refractive errors after keratorefractive surgeries [39, 156].

Standard mechanical characterization techniques, such as strip extensiometry, compression and inflation tests, have provided some important basic understanding of cornea biomechanics, but they are not applicable for *in vivo* measurements [9, 44, 166]. A variety of non-destructive approaches are currently under active development. Corneal response to air-puff stimuli, characterized by light scattering, Scheimpflug imaging, or optical coherence tomography (OCT), can provide empirical metrics of the

mechanical properties, which have been found to correlate with clinical conditions [4, 37, 46, 128]. However, these approaches do not provide a direct readout of the elastic modulus, and are unsuited for making localized elasticity measurements[31]. Brillouin microscopy can map the mechanical properties of tissues with high spatial resolution, but it measures longitudinal modulus rather than shear modulus that is more directly related to tissue deformation and stiffness [159, 162, 168].

Optical coherence tomography (OCT) is uniquely well suited for ophthalmic imaging due to its balance of spatial resolution, field of view and imaging speed [10, 38]. It can also quantify tissue displacement and deformations with nanometer-level sensitivity [23], making it an ideal candidate for mechanical characterization. OCT-based methods to measure tissue elasticity are known as OCT elastography (OCE) and hold great promise for quantifying the shear-elastic properties of the cornea [79, 89].

Most of the previous OCE research has focused on developing novel mechanical stimulation approaches and physical models of tissue response [7, 59, 191]. Attempts to translate this technology for human *in vivo* imaging has comparatively received only limited attention. One group of researchers has developed a compression-based approach which was demonstrated in a cohort of 10 subjects [32, 49]. However, compression OCE currently lacks the capability to directly quantify the elastic modulus. Traveling wave elastography, another embodiment of OCE, can provide such information, and this approach has been widely studied in previous phantom, *ex vivo*, and live animal studies [7, 61, 94, 143, 147, 177], but was not yet been demonstrated in live humans.

This study presents the measurement of the corneal elastic modulus *in vivo*. Our approach is based on a simple vibrating probe actuated electrodynamically that generate mechanical waves in the cornea by direct contact. The elastic wave velocity and attenuation are measured using phase-sensitive OCT at discrete stimulation frequencies between 2 and 16kHz. The elastic modulus is then quantified using the Rayleigh wave model from high frequency data.

5.2 Results

5.2.1 Mechanical model of wave propagation in the cornea

The mechanical behavior of the cornea is dictated by the properties of its constituents as well as their microscale arrangement. The corneal stroma is a collagen and proteoglycan-rich connective tissue that occupies about 90 % of the total thickness and provide the largest part of its mechanical strength. Collagen molecules are arranged in fibrils with a diameter of about 30 nm, which themselves assemble in lamellae of parallel fibrils [110]. Within a lamella, fibrils run parallel to each other, organized in a hexagonal lattice. They bathe in a gel-like matrix predominantly composed of water, proteoglycans, non-fibril-forming collagens, and glycoproteins [111]. Lamellae run mostly parallel to the corneal surface. They are stacked on top of each other, with fibril orientation of adjacent layers crossing at large angles. The preferential orientation of lamellae and their degree of interweaving vary with depth and location in the stroma. This complex microarchitecture gives rise to complex mechanical properties, and the cornea is known to be nonlinear, viscoelastic, anisotropic and inhomogeneous [15, 84].

A reasonable assumption to model wave propagation in the cornea is to consider a transverse isotropic symmetry. The properties in a plane tangential to the cornea (xy plane) are approximately equal in every direction because of the large variation in lamellar orientation, but the axis perpendicular to the cornea (z axis) is distinct. The fourth order elastic tensor C_{ijkl} of such a material has 5 independent elastic constants, comparatively with 2 elastic constants for isotropic elastic materials. Expressed in matrix form using Voigt's notation $(xx, yy, zz, yz, xz, xy) \rightarrow (1, 2, 3, 4, 5, 6)$, it can be

written as:

$$C = \begin{bmatrix} C_{11} & C_{11} - 2C_{66} & C_{13} & 0 & 0 & 0 \\ C_{11} - 2C_{66} & C_{11} & C_{13} & 0 & 0 & 0 \\ C_{13} & C_{13} & C_{33} & 0 & 0 & 0 \\ 0 & 0 & 0 & C_{44} & 0 & 0 \\ 0 & 0 & 0 & 0 & C_{44} & 0 \\ 0 & 0 & 0 & 0 & 0 & C_{66} \end{bmatrix} \quad (5.1)$$

Note that the tensor will vary with pre-strain due to nonlinearity, but the behavior is approximately linear around its point of equilibrium for small deformations such as those encountered in acoustic wave propagations. The components of the stiffness tensor should therefore be interpreted as tangential moduli. Viscoelasticity can be considered by allowing the elastic constants to be complex.

In such a material, within a neighborhood where properties are approximately homogeneous, wave velocities along different axes are given by [180]:

$$c_{p,z}^2 = C_{33}/\rho, \quad (\text{Compression wave, } z \text{ propagation}) \quad (5.2)$$

$$c_{s,z}^2 = C_{44}/\rho, \quad (\text{Shear wave, } z \text{ propagation}) \quad (5.3)$$

$$c_{p,x}^2 = C_{11}/\rho, \quad (\text{Compression wave, } x \text{ or } y \text{ propagation}) \quad (5.4)$$

$$c_{s,xz}^2 = C_{44}/\rho, \quad (\text{Shear wave, } x \text{ or } y \text{ propagation, } z \text{ polarized}) \quad (5.5)$$

$$c_{s,xy}^2 = C_{66}/\rho, \quad (\text{Shear wave, } x \text{ or } y \text{ propagation, } y \text{ or } x \text{ polarized}) \quad (5.6)$$

The flexural waves generated by a force normal to the cornea, as those described later in this article, travels and deforms tissues in the zx plane and is composed of z and xz shear wave components. The shear wave velocity for both these waves is given by the elastic modulus C_{44} , which describes the resistance to a shear force applied on the top face of the cornea.

We immediately highlight the fact that inflation and extension tests, which have been extensively used to characterize the corneal mechanical properties [21, 44, 55, 119], measure the in-plane tensile modulus E_x , which is dominated by the component C_{66} .

This result can be obtained by calculating the compliance tensor $S = C^{-1}$ and computing the ratio between stress and strain for a pure in-plane tensile stress σ_{xx} . The result is:

$$E_x = 2(1 + \nu_{xy})C_{66}, \quad \nu_{xy} = \frac{C_{12}C_{33} - C_{13}^2}{C_{11}C_{33} - C_{13}^2} \quad (5.7)$$

Where ν_{xy} is analogous to Poisson's ratio in the xy plane. In nearly incompressible materials, such as biological tissues, $\nu_{xy} \approx 0.5$, and therefore $E_x \approx 3C_{66}$, a result analogous to the isotropic case where $E \approx 3\mu$.

Having established that OCE and classical mechanical tests probe different components of the anisotropic corneal stiffness, we now examine the question of which mechanisms at the microscopic level dictate the values of C_{44} and C_{66} . We consider a simple constitutive model where the cornea is modeled as a stack of thinly sliced isotropic layers (Backus's model) [13]. For layers much thinner than the acoustic wavelength (a reasonable assumption), the combination of layers behaves as an effective material that is transversely isotropic. Even though this is not a completely realistic model for the corneal stroma, it is simple enough to draw valuable intuition.¹ In that model, the coefficients C_{66} and C_{44} , which are of interest for our problem, can be calculated as:

$$C_{44} = \langle \mu^{-1} \rangle^{-1}, \quad C_{66} = \langle \mu \rangle \quad (5.8)$$

where $\langle \cdot \rangle$ represents a volume-weighted average of the different sublayers. We note that the expression for C_{66} is analogous to the additions of springs in parallel (direct sum), while the expression for C_{44} is analogous to the addition of springs in series (inverse sum of inverses). This analogy is illustrated in Fig. 5-1 for a system composed of 2 types of layers.

One important consequence of equations (5.8) is that C_{66} , and thus the tensile modulus, is dominated by the stiffest constituents: the collagen fibers. The tensor component C_{44} , which determines the shear wave velocity, is dominated by the softest mechanical elements: the interfibrillar and interlamellar matrix. This conclusion can

¹A more realistic mechanical description down to the collagen fibril level is still under active development and shall not be included in this thesis.

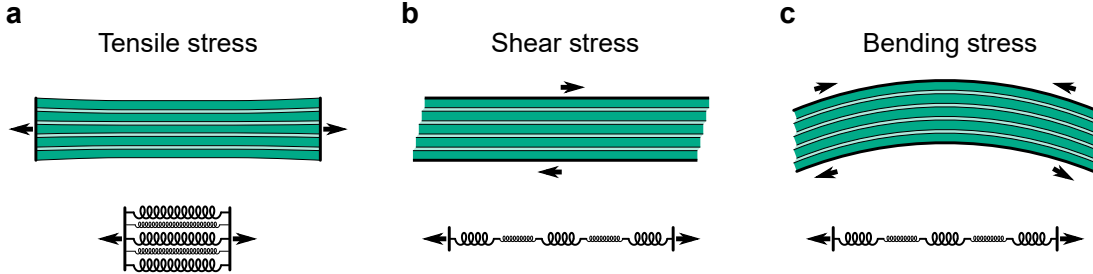


Figure 5-1: Multilayer model of the cornea. (a) Tensile stress. (b) Shear stress. (c) Bending load, which is equivalent to a shear load.

be understood from the spring analogy, but is also well supported from an empirical standpoint: the cornea is very resistant to in-plane tension, but bends readily.

The next step in our development is to model acoustic wave propagation in anisotropic media of finite thickness. Previous studies have used a Lamb wave model [61], which is valid for isotropic materials. A more general solution that accounts for anisotropy can be found in ref. [120] and was presented in detail in section 2.2.2.

The Lamb wave velocities associated with different modes are shown in Fig. 5-2(a) using typical parameters for a human cornea ($C_{44} = 60 \text{ kPa}$, $C_{13} = 2 \text{ GPa}$, $C_{11} = C_{33} \approx C_{13} + 2C_{44}$). The modes are labeled as either quasi-antisymmetric (A_n) or quasi-symmetric (S_n), where the index n indicates the order of the mode. The displacement field associated with the two first modes is also shown in Fig. 5-2(b), for a frequency of 10 kHz.

In principle, the A_0 , S_0 , and A_1 modes could be excited in the 2 to 16 kHz frequency band considered later in this study. Using coupled modes theory, we can estimate the amplitude coefficients a_n as an overlap integral:

$$a_n = \int \mathbf{u}_0^*(z) \cdot \mathbf{u}_n(z) dz \quad (5.9)$$

where $n = \{A_0, S_0, S_1, \dots\}$ is an index representing the mode, $\mathbf{u}_n(z)$ is the normalized displacement field associated with each mode, $\mathbf{u}_0(z) = \mathbf{u}(z, x = 0)$ is the observed displacement field at the point of excitation. Based on our observations of the displacement field profile in porcine corneas [143] and those presented later in this

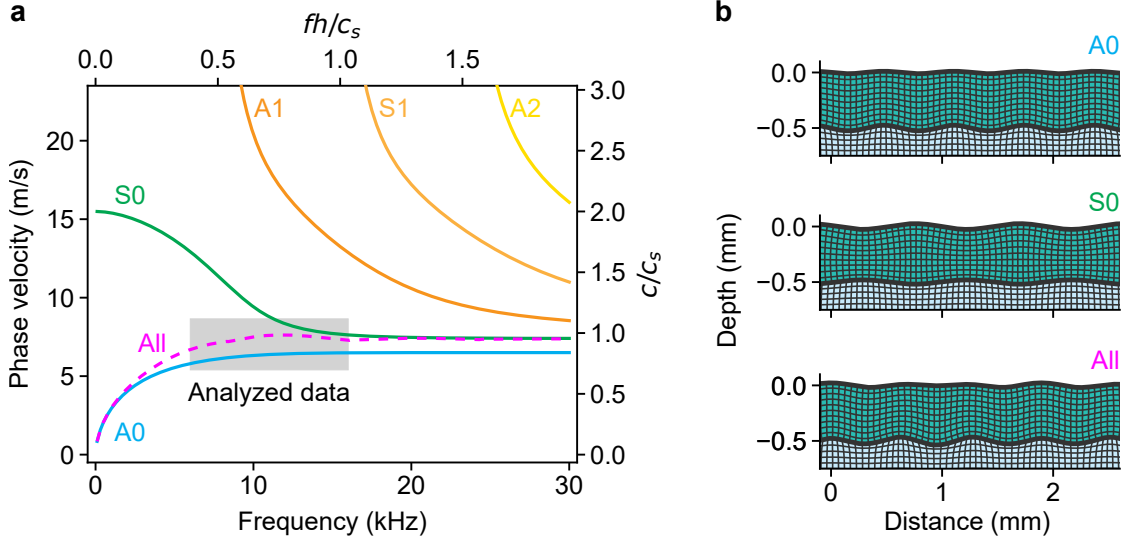


Figure 5-2: Simulated Lamb wave spectrum (a) and mode shapes (b) for a typical human cornea (thickness of 500 μm , density of 1 g/cm^3 and in-plane shear modulus of 60 kPa).

study, the displacement profile near the source is nearly uniform with depth. From the result of the overlap integral, we calculated the phase velocity on the top (air-cornea) surface, close to the point of excitation, shown as a magenta dotted line in Fig. 5-2(a). The combined displacement field is also shown as the bottom panel of Fig. 5-2(b).

At frequencies above 6 kHz, the phase velocity converges rapidly towards the asymptotic value of the S_0 mode, which corresponds to that of a Rayleigh surface wave $c_{\text{Ray}} \approx 0.95 c_{s,xy}$. From these considerations, we propose that the in-plane shear modulus can be calculated through the equation:

$$C_{44} = \rho c_{s,xy}^2 = \rho(0.95 c_{\text{Ray}})^2 \quad (5.10)$$

where c_{Ray} is estimated in the range of 6 to 16 kHz.

5.2.2 Mechanical wave velocity in human cornea

Mechanical waves are generated in the cornea by direct contact with a vibrating probe, as illustrated in Fig. 5-3. The tip is actuated using a stepped-frequency sinusoidal waveform. Frequency is varied from 2 to 16 kHz by increments of 2 kHz while OCT

data is collected in M-B scan mode. A single scan with 8 frequencies lasts 1 s. A cooperative subject can refrain from blinking during about 10 s, so a given measurement included 10 scans at each frequency. More detail on the scanning pattern and stimulus waveforms is presented in the Materials and Methods section of this study.

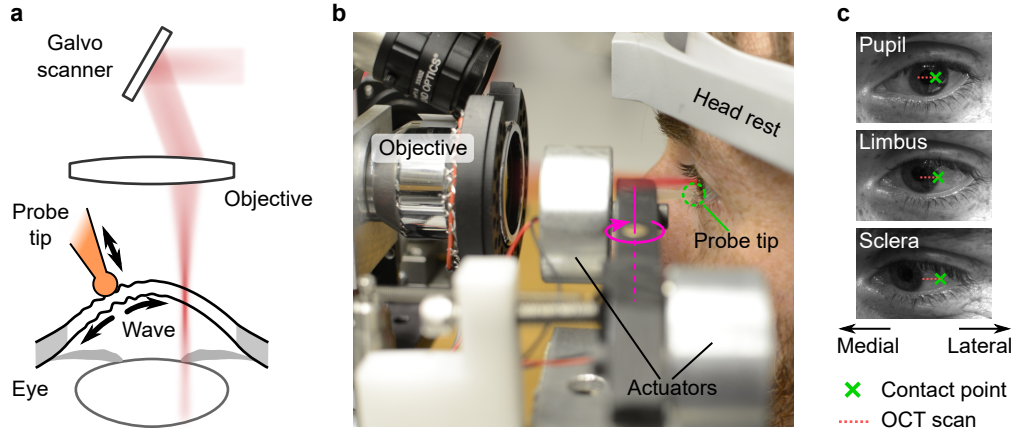


Figure 5-3: System used for *in vivo* corneal elastography. (a) Schematic representation of the principle of operation. A vibrating probe tip makes contact with an anesthetized cornea to generate mechanical waves, which are captured by OCT imaging. (b) Picture of the prototype. The probe tip (circled in green) is mounted on a lever arm which is driven by a pair of linear actuators. The lever arm is compliant to subject motion by rotating around its pivot axis (magenta dotted line). (c) Measurement locations. Mechanical waves were excited from three contact points (green cross), labeled as pupil, limbus and sclera. The OCT beam scan path over which mechanical waves are measured is shown as a red dotted line.

We tested 3 contact points on each subject, shown in Fig. 5-3(c): pupil (contact on the central cornea, near the lateral pupil boundary), limbus (contact at the lateral scleral-corneal boundary), and sclera (contact about 5 mm lateral of the scleral-corneal boundary). All contact points are located as close as possible to the horizontal meridian of the eye. Up to 4 measurements are performed at each location, depending on the ability of the subject to stay still. A complete imaging session typically included 8 to 12 measurements (3-4 per location) and lasted about 15 minutes. Standard volumetric OCT scans (no elastography) were also performed at the end of the session.

Phase-sensitive OCT is used to measure the resulting displacement as a function of position and time. Typical snapshots of wave propagation at different frequencies are shown in Fig. 5-4.

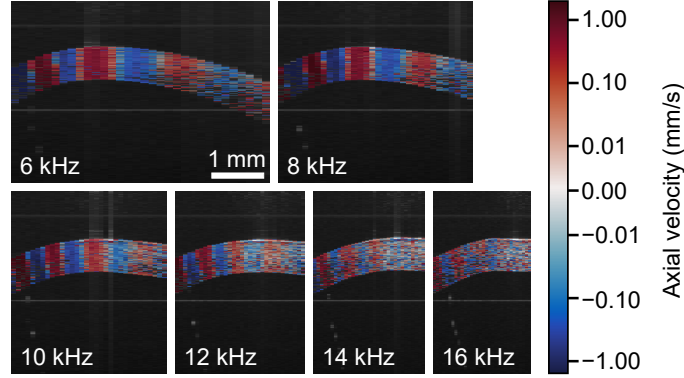


Figure 5-4: Wave propagation in a human cornea *in vivo* (subject #1, first scan) measured by phase-sensitive OCT.

The mechanical wave velocity is computed using a 2D Fourier transform, from time t to frequency f and from lateral position x to wavenumber k , as was described in ref. [143]. Briefly, from the full axial displacement field $u_z(\mathbf{r}, t)$, we first select the motion of the top surface $u_{z,\text{top}}(x, t)$. The resulting data is then Fourier transformed from t to f , and only the component $u_n(x)$ at the driving frequency f_n is retained. The data for subject #1 is shown in Fig. 5-5(a).

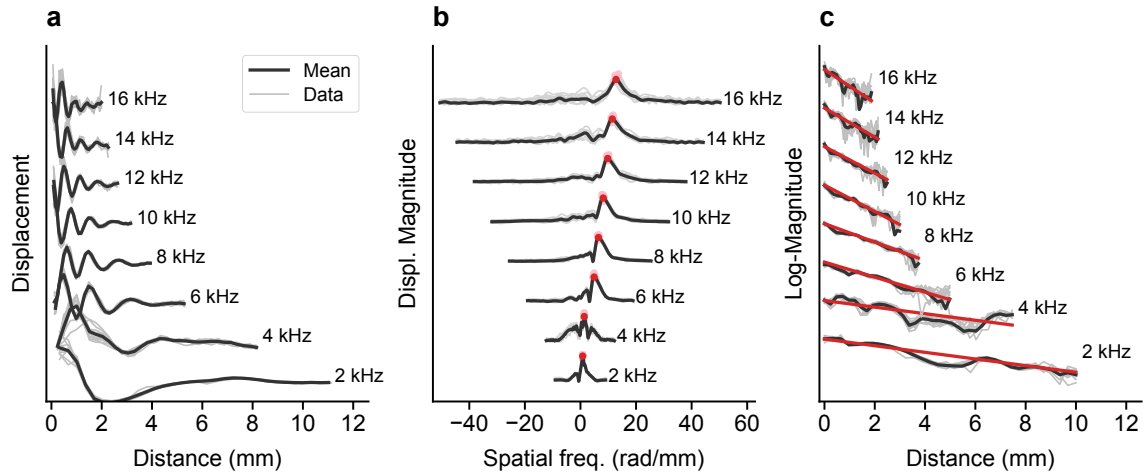


Figure 5-5: Key processing steps for measuring the corneal elastic wave velocity and attenuation, for subject #1. (a) Normalized f - x domain displacement waveforms at each frequency. Only the real part of the complex-valued displacement $u_n(x)$ is shown. The pale lines represent each of the 10 measurements and the dark line is the average. (b) Normalized f - k domain displacement. The red dots represent the location of the identified peak. (c) Measurement of the attenuation constant using a linear fit to the log of the displacement magnitude.

To account for the curvature of the cornea surface when calculating velocity, the propagation distance is expressed in terms of the curvilinear abscissa $s = \int_C ds$ where $ds^2 = dx^2 + dz^2$ and C indicates the integration path along the corneal surface. A second Fourier transform ($s \rightarrow k$) is then carried (Fig. 5-5(b)). The peak wavenumber k_{peak} is found using a bounded max search, followed by quadratic interpolation to further refine its location. The surface wave velocity $c(f_n)$ is then calculated from:

$$c(f_n) = \frac{2\pi f_n}{k_{\text{peak}}} \quad (5.11)$$

This process is repeated for each frequency and each repetition of the scan. Figure 5-6 shows the resulting wave velocity at the center of the cornea for each of our subjects, plotted as a function of frequency. The boxes represent the distribution of the 10 scan repetitions executed during a single measurement.

We note that the apparent wave velocity at low frequencies (2 and 4 kHz) tend to rise suddenly as the frequency approaches zero. This phenomenon, which was discussed in ref. [143], is thought to be due to the interference of the main corneal wave with secondary waves traveling at different velocities. These can include compression waves, bulk motion, and resonances. Such multi-wave measurements are difficult to interpret and the data below 4 kHz was ignored in later processing steps. We also noted that for some subjects, the wave amplitude at higher frequencies was insufficient to accurately extract the wave velocity, presumably due to a poor contact between the vibrating tip and the corneal surface. The low-frequency and low-signal points were ignored in subsequent analyses but are shown in grey on Fig. 5-6 for completeness.

We also calculated the wave attenuation by fitting a linear function to the natural logarithm of the displacement magnitude, $F_n(s) = \kappa_n \log |u_n(s)| + b_n$, where κ_n is the attenuation coefficient associated with frequency f_n .

5.2.3 Factors influencing wave velocity

We have examined the dependence of wave velocity on various factors that could potentially influence or confound our measurements. The parameters examined are

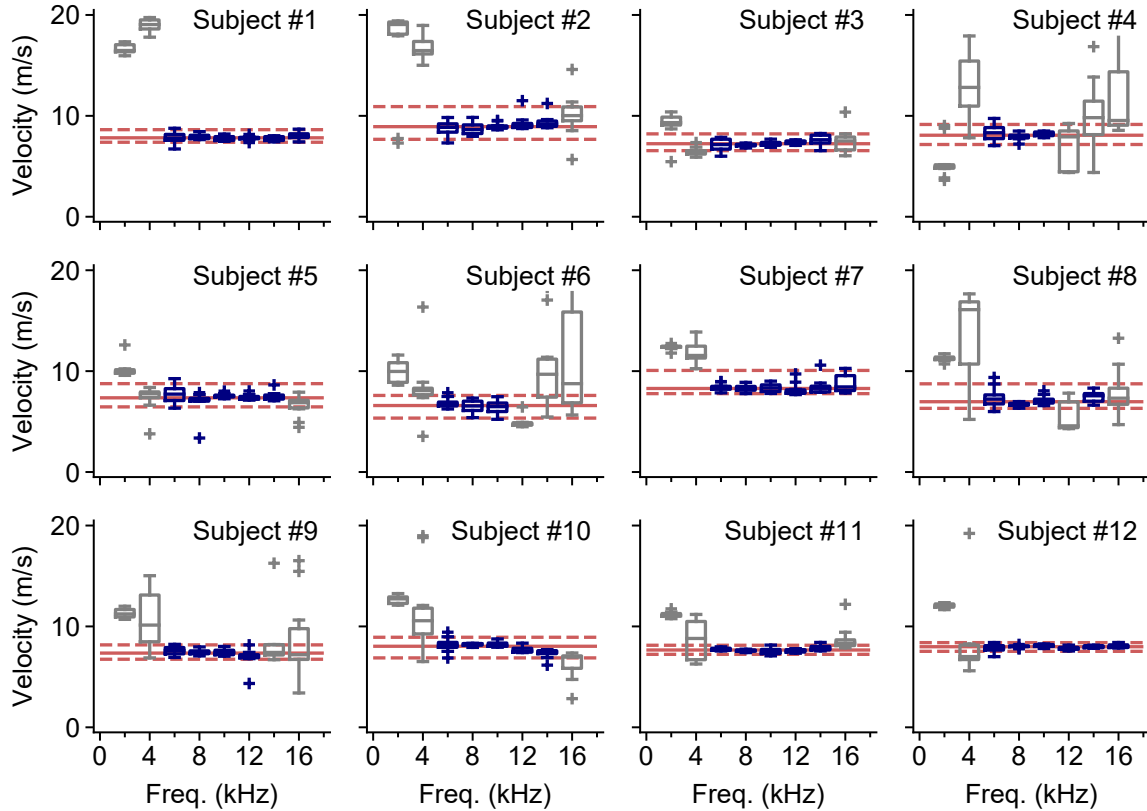


Figure 5-6: Distribution of the measured wave velocities as a function of frequency for each subject. Gray boxes represent rejected data at low frequencies, or with significant noise from insufficient signal. Red lines represent the overall median of the valid data (full line) and the interval containing 95 % (dashed lines).

the subject's age, Goldmann-measured intraocular pressure (IOP), central corneal thickness (CCT), IOP-induced tensile stress (calculated from IOP, CCT and corneal curvature), gender, and contact location.

The results for subject gender and contact point location are shown in Fig. 5-7(a) and (b). We found no significant difference between male and female subjects. We did find a notable difference between wave velocity in the sclera and cornea (pupil region and lateral limbus region). The higher wave velocity observed in the sclera is largely compatible with the larger stiffness values compared to the cornea generally reported in literature [194]. The wide range of wave velocities in the sclera could be explained by the larger heterogeneity of this tissue compared to the cornea. Statistical power was insufficient to establish a difference between the pupil and limbus areas.

Results for continuous variables (age, IOP, CCT and tensile stress) are shown in

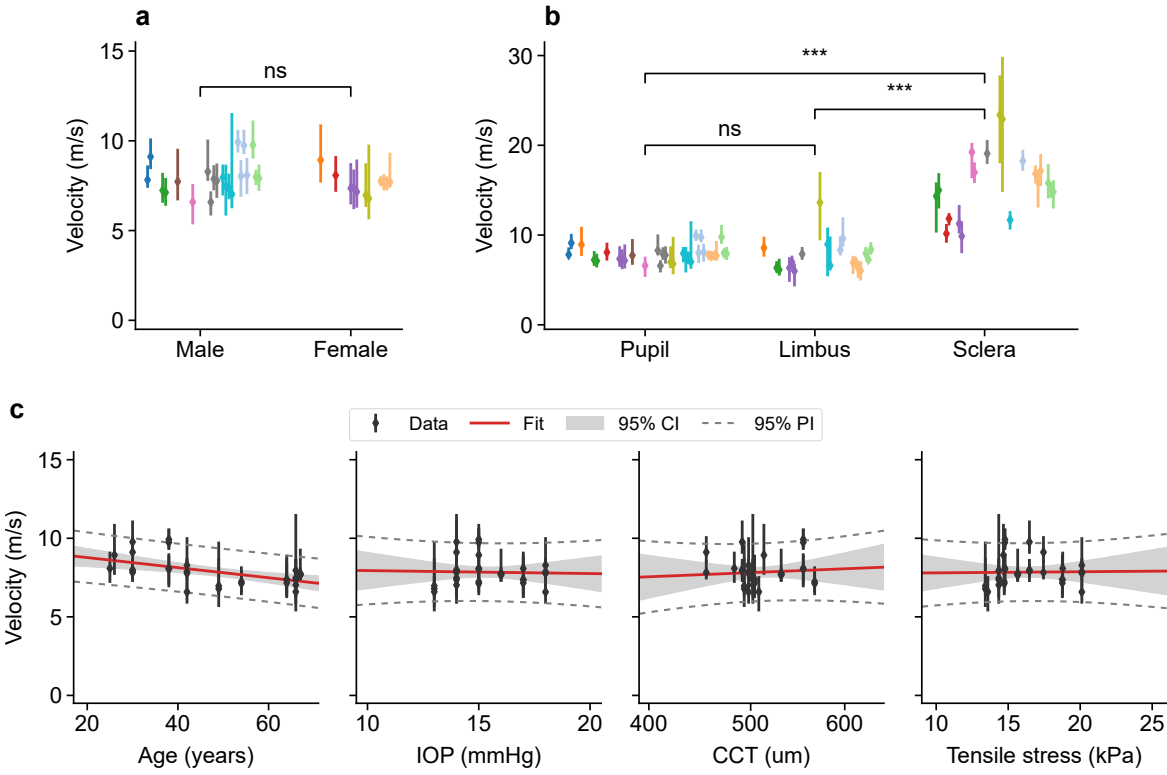


Figure 5-7: Wave velocity as a function of gender (a) and contact location (b). Each individual subject is labeled by a unique color. Multiple repetitions of each scan are plotted as separate markers. Only the pupil area data is shown in the gender comparison. (ns : non-significant, * : $p < 0.05$, ** : $p < 0.01$, *** : $p < 0.001$). (c) Wave velocity as a function of age, intraocular pressure (IOP), central corneal thickness (CCT) and IOP-induced tensile stress. Points and errorbars represent the median wave velocity and the quantile range containing 95 % of the measurements (at valid frequencies and across repetitions).

Fig. 5-7(c). Linear regression analysis was performed on each dataset, and we show the best fit (red line), 95 % confidence interval for the regression (CI, shaded grey area) and prediction interval (PI, dotted line) within which 95 % of measurements should fall. Corneal wave velocity was found to decrease with age with a slope $-3.2 \text{ m/s}/100 \text{ years}$ and a 95 % confidence interval of $\pm 1.7 \text{ m/s}/100 \text{ years}$. No correlation with intraocular pressure, tensile stress and thickness were found.

5.3 Discussion

One important implication of our study is that the in-plane shear modulus and the tensile Young’s modulus are affected in different ways by aging. Previous studies examined the age-dependence of cornea biomechanics [21, 43], and found a significant increase in the tensile modulus with age (about 2-fold over a lifespan). Due to the important anisotropy of corneal tissue, it should not be unexpected that different mechanical properties behave in different ways. Flexural wave velocity measured by OCE probes the in-plane shear modulus of the material, which reflects the properties of the interfibrillar and interlamellar matrix. This modulus can be very different from the in-plane tensile rigidity measured by stretch or inflation tests, which reflects the stiffness of the collagen fibrils themselves.

Literature on the interlamellar and interfibrillar shear cohesion is limited. A handful of studies have attempted to measure the shear modulus using standard *ex vivo* tests and reported values of 2.0 kPa [176], 9.5 kPa [134], 16 kPa [42] and up to 80 kPa [174]. The average Rayleigh wave velocity in our study is 7.85 m/s, corresponding to an in-plane shear modulus of 68 kPa. This result is largely compatible with the abovementioned studies given that the shear modulus of soft viscoelastic tissues generally increases with frequency.

The age dependence of the shear modulus, to our knowledge, has not been examined. Interlamellar cohesive strength was studied by measuring the force required to separate two layers [144, 175]. Correlation with age was poor but positive. However, the “peeling” measurement approach is likely to be dominated once again by tensile properties, more specifically the yield strength of the fibrils that intertwine between lamellae. Overall, there is insufficient literature to either support or invalidate our hypothesis that shear cohesion decreases with age. Further studies using standard shear rheometry should be conducted, but this lies outside the scope of this article.

At this stage, our proposition should be considered as a postulate, but if verified, it could have important implications. According to our models, the mechanical properties of the matrix should be responsible for the flexibility of the cornea, which

gives the tissue strength and toughness to withstand environmental damage. Cell-matrix interaction are also affected by the mechanical properties of the latter, and can potentially affect cell migration, tissue repair, and remodeling after surgeries. Finally, keratoconus involves changes in interlamellar cross-links and abnormal shear behavior [112, 141]. The shear-mechanical information obtained by OCE could therefore provide valuable information for diagnosis and management of corneal ectasias.

5.4 Materials and Methods

5.4.1 Study design

This pilot study presents the data from 13 healthy volunteers. The age of the subjects ranged between 25 and 67 years. Individuals with a refractive error beyond ± 6 D, prior LASIK or other eye surgery, or significant eye disease were excluded from the study. Informed consent was obtained from the subjects after explanation of the nature and possible consequences of the study. The protocol was approved by the institutional review board (IRB) at Massachusetts General Hospital.

Due to space constraints in the instrument, only the left eye was measured. In addition to OCE imaging, a complete measurement session included a standard OCT volumetric scan of the anterior segment, Goldmann tonometry and a fluorescein eye stain under slit lamp examination. Geometric parameters such as CCT and corneal curvature were extracted from volumetric OCT scans performed with our home-built system. They might include some biases due to incorrect geometric calibrations, but relative comparisons between subjects and overall trends examined here should not be affected.

5.4.2 Instrument design

The instrument used in this study is a modified version of the system described in refs. [142, 143]. OCT imaging and deformation measurements are performed with

a home-built, polygon-swept-source system. The laser has a central wavelength of 1300 nm, a -3 dB bandwidth of 108 nm, and a sweep rate (A-line rate) of 43.1 kHz. The total illumination power on the subject's cornea is 15 mW, which is in agreement with the ANSI-Z136.1-2014 safety standard. The axial and transverse resolutions are respectively 15 and 30 μ m.

The imaging arm of the OCT system includes a beam collimator, 2-axis galvanometer scanner (Cambridge Technology, 6210H) and objective lens (Thorlabs, LSM54-1310) with a working distance of 64 mm. This sub-assembly is mounted on a human interface based on a recycled slit-lamp instrument. It provides a chin and forehead rest for the patient, and a joystick for coarse manual alignment to the imaged eye.

The probe tip is custom-designed and 3D-printed in a biocompatible material (Formlabs, Dental SG). The contact end of the probe is spherical with a diameter of 2 mm. It was hand-polished down to a final grit of 300 nm to minimize surface roughness. The other end of the tip is mounted on spring-loaded lever arm, which is designed to apply a constant force of approximately 20 mN. The lever arm is actuated by a pair of electrodynamic transducers (Adafruit, 1784), positioned symmetrically on each side of the lever pivot axis. The frequency response of the actuators was calibrated prior to the experiments, and the applied voltage at any given frequency was set to produce deformation about one third of the maximum detectable amplitude (phase-wrapping limit).

The analog waveforms used to drive the mechanical stimulus and the beam scanning galvanometers are generated by a multi-purpose input/output board (USB-6353, National Instrument). They are hardware-synchronized to the OCT laser sweep rate and data acquisition, ensuring phase-synchronous operation. An off-the-shelves audio amplifier (Crown Audio, XLI) drives the electrodynamic actuators.

5.4.3 Imaging protocol

Proparacaine ophthalmic drops are administered to the targeted eye prior to contact measurements (OCE and tonometry) as a topical anesthetic. At the beginning of an

OCE measurement, the probe tip is withdrawn. The system is first aligned to the subject's eye using standard anatomic OCT imaging. When a satisfying alignment is reached, the subject is instructed to stay as still as possible and refrain from blinking during about 10 s. The probe tip is moved towards the cornea using a thumb screw until contact is made. The tip is then withdrawn after 10 s, allowing the subject to blink and relax between measurements. The subject is instructed to gaze at targets positioned behind the instrument to orient the eye in an angle that exposes the region of interest nearly perpendicular to the imaging beam.

The stimulus waveform and scanning pattern used in this study were designed to minimize the measurement time, and are shown in Fig. 5-8. For adequate temporal sampling at frequencies up to 16 kHz with an A-line rate of 43 kHz, an M-B scan configuration is implemented: M consecutive A-lines are acquired at any specific transverse location x while the stimulus signal is generated. The beam is then moved to a different location and the stimulus waveform is repeated. We typically used $M = 172$ which maintained the duration of an individual M-scan to 4 ms.

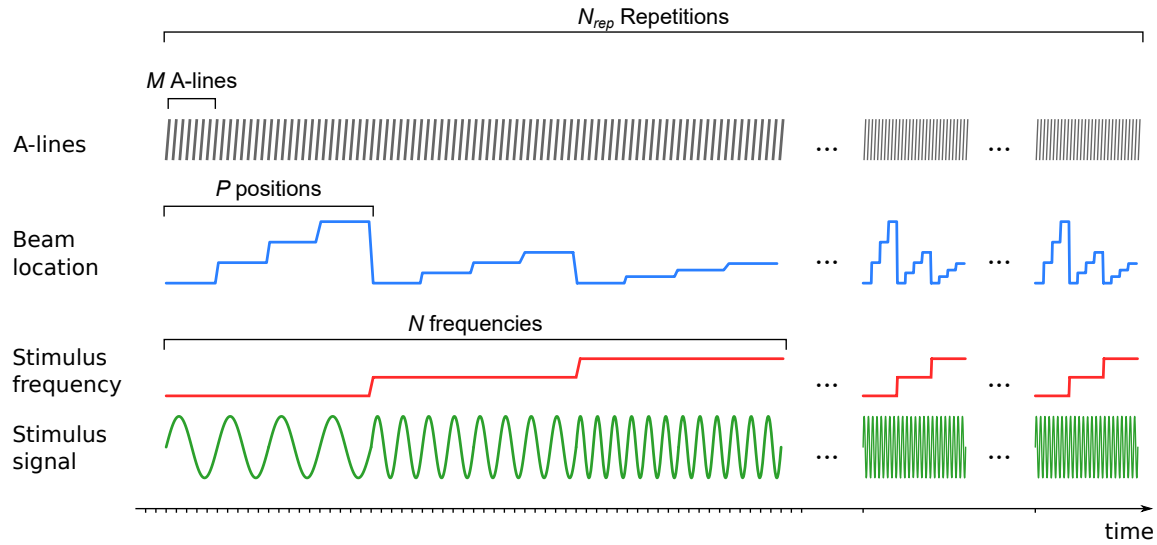


Figure 5-8: Stimulus waveforms and scanning pattern used for *in vivo* OCE. The waveforms are illustrated with smaller values of N_{rep} , M , P and N for clarity.

The spatial sampling density required to correctly capture the acoustic waveform as a function of position depends on the acoustic wavelength. To capture p samples per wavelength λ from a wave driven at frequency f traveling at approximate velocity

c_{approx} , the sampling step δx is given by:

$$\delta x = \frac{\lambda}{p} = \frac{c_{\text{approx}}}{pf} \quad (5.12)$$

In this study, we designed the scanning pattern to sample approximately $p = 8$ points per wavelength, a reasonably safe factor 4 below Nyquist's limit. We assumed $c_{\text{approx}} = 7.5 \text{ m/s}$ based on pilot experiments.

At the same time, mechanical waves traveling in the cornea tend to be rapidly attenuated, and it is thus unnecessary to measure their propagation beyond 3 to 4 wavelengths. Attenuation coefficients in biological tissues typically increase nearly linearly with frequency [102, 193]. We can then fix the total number of sampling points to $P = 4p = 32$, and adjust the scan step δx as the frequency is varied. This dynamic scan size adjustment enables us to maintain the measurement time for a single M-B scan at a given frequency at a duration of 0.128 s, during which patient motion is usually no more than a few hundreds of microns.

A complete measurement includes $N = 8$ different frequencies (2 to 16 kHz by steps of 2 kHz), for a duration of 1 s, and this scan is repeated $N_{\text{rep}} = 10$ times to collect a maximum amount of data during a typical 10 s that a human can stand still without blinking. Note however that each M-B scan is processed independently, and the cumulative bulk motion beyond the 0.128 s measurement time does not affect the results.

5.4.4 Displacement field measurement

The raw data collected by the OCT system is processed using standard swept-source phase-stabilized algorithms, similar to those described in ref. [17]. The resulting complex-valued OCT tomogram is denoted $A(\mathbf{r}, t)$, where t is the time and $\mathbf{r} = (x, z)$ represents the transverse and axial position vector within the dataset. The axial

component of the displacement field $u_z(\mathbf{r}, t)$ is computed from $A(\mathbf{r}, t)$ as:

$$\Delta\phi(\mathbf{r}, t_i) = \arg \left(\sum_{\mathbf{r} \in \text{ROI}} A^*(\mathbf{r}, t_{i-1}) A(\mathbf{r}, t_i) \right) \quad (5.13)$$

$$\phi(\mathbf{r}, t_m) = \sum_{i=1}^m \Delta\phi(\mathbf{r}, t_i), \quad m = 1, 2, \dots, M \quad (5.14)$$

$$u_z(\mathbf{r}, t_m) = \frac{\lambda_0}{4\pi n_c} \left(\phi(\mathbf{r}, t_m) + \phi(\mathbf{r}_{\text{top}}, t_m) \frac{n_c - n_0}{n_0} \right) \quad (5.15)$$

where ROI is a small neighborhood around \mathbf{r} , $\lambda_0 = 1300 \text{ nm}$ is the central free-space wavelength of the OCT beam, $n_0 = 1$ and $n_c = 1.376$ are respectively the refractive indices of the air and the cornea, and $\phi(\mathbf{r}_{\text{top}}, t)$ is the measured phase at the air-sample boundary [178]. The ROI used for z axis projections is a 11×1 window.

Chapter 6

Conclusion and outlook

The work presented in this thesis demonstrates that optical coherence vibrography (OCV) and elastography (OCE) are promising tools to study the mechanical behavior of biological tissues. We have shown that OCV is well suited to measure the natural motion of the middle ear under sound stimulation, which was used to study the modes of motion of the ossicular chain and tympanic membrane at various sound frequencies. We have also demonstrated how OCE can be used to quantify the shear modulus of soft materials, especially the cornea, both *ex vivo* and *in vivo*.

Despite rapid advances from multiple research groups, OCV and OCE are still relatively immature technologies compared with their ultrasound and magnetic resonance counterparts, or with OCT technology as a whole. Further studies are needed to demonstrate utility in a specific clinical context. Middle ear OCV of humans has now been demonstrated by the Adamson group [100]. A pilot study on patients with stapes fixation was recently presented, based on low-frequency vibration amplitude [101]. Follow-up studies should investigate how such measurements can fit in the clinical management of these patients. It would also be interesting to investigate if the vibration phase and higher frequencies can lead to improved diagnosis, especially in milder or more ambiguous cases of conductive hearing loss.

Regarding the cornea study, a logical follow-up step would be to measure patients with mild keratoconus and compare them against the cohort of healthy volunteers examined in our study (chapter 5). If significant differences can be observed, long

term studies would be needed to assess if such measurements can be predictive of the disease progression. Rigorous comparisons with competing approaches such as the air-puff/scheimpflug method [4] should also be conducted.

While the two applications presented here could have a high impact on biological research and medicine, there are many other applications that can be envisioned. The scope of possible organs and materials to study is essentially defined by the relative strengths and weaknesses of OCT compared with other imaging technologies. With a penetration depth of a few millimeters and resolution of a few microns, OCT is particularly well suited to imaging the eye, skin, gastrointestinal and cardiovascular systems, all of which have important biomechanical components.

For example, stiffening of the crystalline lens is related to presbyopia, a disease that affects most of the adult population [54]. OCE, in combination with focused ultrasounds, has been proposed to asses age-related changes in lens stiffness [196]. Another ophtalmic application is myopia, a common condition that affects increasing proportion of the population [65]. It is a multifactorial disease that involves scleral remodeling, and biomechanics-related therapies have been proposed [87]. OCE could play a part in assessing disease progression and help the development of novel treatments. Yet another example would be to assess the wall stiffness of arteries. There is an ongoing effort to include biomechanical parameters in risk assessment of coronary plaque rupture [36]. As catheter-based OCT is becoming increasingly available in interventional cardiology, there is a real opportunity for OCE to contribute to the fight against this important cause of mortality.

OCT technology has rapidly progressed over the last decades, and further improvements to the core technology could have important benefits for OCV and OCE. OCT systems based on broadband supercontinuum light sources can achieve resolutions on the order of $1\text{ }\mu\text{m}$ [97]. The use of OCV in the study of inner ear mechanics has been blooming in parallel with our middle ear work [90, 145], and ultra-high resolution OCT could help elude cochlear mechanics down to the cellular level.

The imaging speed of OCT is also rapidly improving. With the development of Fourier-domain mode-locked (FDML) and stretched-pulse mode-locked (SPML) lasers,

multi-MHz A-line rates are now possible with phase-stable operation [83, 170]. One possibility enabled by such systems is to measure motion synchronously in the B-scan plane, rather than relying on repeated stimuli. This approach could significantly reduce imaging time and thus allow for denser mapping of the vibratory motion and of the elastic properties. Furthermore, tracking the propagation of compression waves becomes realistic at such imaging speeds. This would allow to map multiple components of the stiffness tensor with a single instrument, providing a more complete description of tissue mechanical properties.

Bibliography

- [1] B. Imran Akca, Ernest W. Chang, Sabine Kling, Antoine Ramier, Giuliano Scarcelli, Susana Marcos, and Seok H. Yun. Observation of sound-induced corneal vibrational modes by optical coherence tomography. *Biomedical Optics Express*, 6(9):3313, 2015.
- [2] Keiiti Aki and Paul G. Richards. *Quantitative Seismology*. University Science Books, 2002.
- [3] Wes M. Allen, Ken Y. Foo, Renate Zilkens, Kelsey M. Kennedy, Qi Fang, Lixin Chin, Benjamin F. Dessauvagie, Bruce Latham, Christobel M. Saunders, and Brendan F. Kennedy. Clinical feasibility of optical coherence micro-elastography for imaging tumor margins in breast-conserving surgery. *Biomedical Optics Express*, 9(12):6331, dec 2018.
- [4] Renato Ambrósio, Bernardo T. Lopes, Fernando Faria-Correia, Marcella Q. Salomão, Jens Bühren, Cynthia J. Roberts, Ahmed Elsheikh, Riccardo Vinciguerra, and Paolo Vinciguerra. Integration of Scheimpflug-Based Corneal Tomography and Biomechanical Assessments for Enhancing Ectasia Detection. *Journal of refractive surgery (Thorofare, N.J. : 1995)*, 33(7):434–443, jul 2017.
- [5] Renato Ambrósio and J. Bradley Randleman. Screening for ectasia risk: what are we screening for and how should we screen for it? *Journal of refractive surgery (Thorofare, N.J. : 1995)*, 29(4):230–2, apr 2013.
- [6] Łukasz Ambroziński, Ivan Pelivanov, Shaozhen Song, Soon Joon Yoon, David Li, Liang Gao, Tueng T. Shen, Ruikang K. Wang, and Matthew O’Donnell. Air-coupled acoustic radiation force for non-contact generation of broadband mechanical waves in soft media. *Applied Physics Letters*, 109(4):043701, jul 2016.
- [7] Łukasz Ambroziński, Shaozhen Song, Soon Joon Yoon, Ivan Pelivanov, David Li, Liang Gao, Tueng T. Shen, Ruikang K. Wang, and Matthew O’Donnell. Acoustic micro-tapping for non-contact 4D imaging of tissue elasticity. *Scientific Reports*, 6(October):38967, dec 2016.
- [8] Troels T. Andreassen, Anders Hjorth Simonsen, and Hans Oxlund. Biomechanical properties of keratoconus and normal corneas. *Experimental Eye Research*, 31(4):435–441, oct 1980.

- [9] Troels T. Andreassen, Anders Hjorth Simonsen, Hans Oxlund, a H Simonsen, and Hans Oxlund. Biomechanical properties of keratoconus and normal corneas. *Experimental Eye Research*, 31(4):435–441, oct 1980.
- [10] Marcus Ang, Mani Baskaran, René M. Werkmeister, Jacqueline Chua, Doreen Schmidl, Valentin Aranha Dos Santos, Gerhard Garhöfer, Jodhbir S. Mehta, and Leopold Schmetterer. Anterior segment optical coherence tomography. *Progress in retinal and eye research*, 66:132–156, sep 2018.
- [11] Brian E Applegate, Ryan L Shelton, Simon S Gao, and John S Oghalai. Imaging high-frequency periodic motion in the mouse ear with coherently interleaved optical coherence tomography. *Optics Letters*, 36(23):4716, dec 2011.
- [12] Brian K. Armstrong, Michelle P. Lin, Matthew R. Ford, Marcony R. Santhiago, Vivek Singh, Gregory H. Grossman, Vandana Agrawal, Abhijit Sinha Roy, Robert S. Butler, William J. Dupps, and Steven E. Wilson. Biological and Biomechanical Responses to Traditional Epithelium-Off and Transepithelial Riboflavin-UVA CXL Techniques in Rabbits. *Journal of Refractive Surgery*, 29(5):332–341, may 2013.
- [13] George E. Backus. Long-wave elastic anisotropy produced by horizontal layering. *Journal of Geophysical Research*, 67(11):4427–4440, oct 1962.
- [14] Brecken J Blackburn, Shi Gu, Matthew R Ford, Vinícius de Stefano, Michael W Jenkins, William J Dupps, and Andrew M Rollins. Noninvasive Assessment of Corneal Crosslinking With Phase-Decorrelation Optical Coherence Tomography. *Investigative ophthalmology & visual science*, 60(1):41–51, 2019.
- [15] Brecken J. Blackburn, Michael W. Jenkins, Andrew M. Rollins, and William J. Dupps. A Review of Structural and Biomechanical Changes in the Cornea in Aging, Disease, and Photochemical Crosslinking. *Frontiers in bioengineering and biotechnology*, 7:66, mar 2019.
- [16] Caroline Boudoux. *Fundamentals of Biomedical Optics*. Pollux, 2016.
- [17] Boy Braaf, Koenraad A. Vermeer, Victor Arni D.P. Sicam, Elsbeth van Zeeburg, Jan C. van Meurs, and Johannes F. de Boer. Phase-stabilized optical frequency domain imaging at 1-um for the measurement of blood flow in the human choroid. *Optics Express*, 19(22):20886, 2011.
- [18] Anke Burkhardt, Lars Kirsten, Matthias Bornitz, Thomas Zahnert, and Edmund Koch. Investigation of the human tympanic membrane oscillation ex vivo by Doppler optical coherence tomography. *Journal of Biophotonics*, 7(6):434–441, jun 2014.
- [19] Anke Burkhardt, Julia Walther, Peter Cimalla, Matthias Bornitz, and Edmund Koch. Endoscopic optical coherence tomography for imaging the tympanic membrane. In Rainer A. Leitgeb and Brett E. Bouma, editors, *Proc. SPIE 8091*,

Optical Coherence Tomography and Coherence Techniques V, page 80910Y, jun 2011.

- [20] Anke Burkhardt, Julia Walther, Peter Cimalla, Mirko Mehner, and Edmund Koch. Endoscopic optical coherence tomography device for forward imaging with broad field of view. *Journal of Biomedical Optics*, 17(7):071302, may 2012.
- [21] Nathaniel E Knox Cartwright, John R. Tyrer, and John Marshall. Age-related differences in the elasticity of the human cornea. *Investigative Ophthalmology and Visual Science*, 52(7):4324–4329, 2011.
- [22] Ernest W. Chang, Jeffrey T. Cheng, Christof Röösli, James B. Kobler, John J. Rosowski, and Seok Hyun Yun. Simultaneous 3D imaging of sound-induced motions of the tympanic membrane and middle ear ossicles. *Hearing research*, 304:49–56, oct 2013.
- [23] Ernest W Chang, James B Kobler, and Seok H Yun. Subnanometer optical coherence tomographic vibrography. *Optics Letters*, 37(17):3678–3680, sep 2012.
- [24] Shao-Hsuan Chang, Ashkan Mohammadvali, Kai-Jung Chen, You-Ren Ji, Tai-Horng Young, Tsung-Jen Wang, Colin E Willoughby, Kevin J Hamill, and Ahmed Elsheikh. The Relationship Between Mechanical Properties, Ultrastructural Changes, and Intrafibrillar Bond Formation in Corneal UVA/Riboflavin Cross-linking Treatment for Keratoconus. *Journal of refractive surgery*, 34(4):264–272, apr 2018.
- [25] Jeffrey Tao Cheng, Antti A. Aarnisalo, Ellery Harrington, Maria del Socorro Hernandez-Montes, Cosme Furlong, Saumil N. Merchant, and John J. Rosowski. Motion of the surface of the human tympanic membrane measured with stroboscopic holography. *Hearing Research*, 263(1-2):66–77, may 2010.
- [26] Samuel Choi, Keita Sato, Takeru Ota, Fumiaki Nin, Shogo Muramatsu, and Hiroshi Hibino. Multifrequency-swept optical coherence microscopy for highspeed full-field tomographic vibrometry in biological tissues. *Biomedical Optics Express*, 8(2):608–621, 2017.
- [27] Michael A Choma, Audrey K Ellerbee, Changhuei Yang, Tony L Creazzo, and Joseph A Izatt. Spectral-domain phase microscopy. *Optics letters*, 30(10):1162–1164, 2005.
- [28] Niloy Choudhury, Guiju Song, Fangyi Chen, Scott Matthews, Tanja Tschinkel, Jiefu Zheng, Steven L. Jacques, and Alfred L. Nuttall. Low coherence interferometry of the cochlear partition. *Hearing Research*, 220(1-2):1–9, 2006.
- [29] Ernst Dalhoff, Ralf Gärtner, Ulrich Hofbauer, Hans Tiziani, Hans-Peter Zenner, and Anthony W. Gummer. Low-coherence fibre heterodyne interferometer for both dc and high-frequency vibration measurements in the inner ear. *Journal of Modern Optics*, 45(4):765–775, apr 1998.

- [30] Ombeline de La Rochefoucauld, Shyam M Khanna, and Elizabeth S Olson. Recording depth and signal competition in heterodyne interferometry. *The Journal of the Acoustical Society of America*, 117(3):1267–1284, mar 2005.
- [31] Vinicius S De Stefano and William J Dupps. Biomechanical diagnostics of the cornea. *International Ophthalmology Clinics*, 57(3):75–86, 2017.
- [32] Vinicius S. De Stefano, Matthew R. Ford, Ibrahim Seven, and William J. Dupps. Live human assessment of depth-dependent corneal displacements with swept-source optical coherence elastography. *PLOS ONE*, 13(12):e0209480, dec 2018.
- [33] Hamid R Djalilian, James Ridgway, Majestic Tam, Ali Sepehr, Zhongping Chen, and Brian J F Wong. Imaging the Human Tympanic Membrane Using Optical Coherence Tomography In Vivo. *Otology & Neurotology*, 29(8):1091–1094, dec 2008.
- [34] Hamid R Djalilian, Marc Rubinstein, Edward C Wu, Kaveh Naemi, Shawn Zardouz, Koohyar Karimi, and Brian J F Wong. Optical Coherence Tomography of Cholesteatoma. *Otology & Neurotology*, 31(6):932–935, aug 2010.
- [35] Li Dong, Philip Wijesinghe, James T. Dantuono, David D. Sampson, Peter R T Munro, Brendan F. Kennedy, and Assad A. Oberai. Quantitative Compression Optical Coherence Elastography as an Inverse Elasticity Problem. *IEEE Journal of Selected Topics in Quantum Electronics*, 22(3):277–287, may 2016.
- [36] Pallavi Doradla, Kenichiro Otsuka, Abhijay Nadkarni, Martin Villiger, Antonios Karanasos, Laurens J.C. van Zandvoort, Jouke Dijkstra, Felix Zijlstra, Gijs van Soest, Joost Daemen, Evelyn Regar, Brett E Bouma, and Seemantini K Nadkarni. Biomechanical Stress Profiling of Coronary Atherosclerosis. *JACC: Cardiovascular Imaging*, apr 2019.
- [37] Carlos Dorronsoro, Daniel Pascual, Pablo Pérez-Merino, Sabine Kling, and Susana Marcos. Dynamic OCT measurement of corneal deformation by an air puff in normal and cross-linked corneas. *Biomedical Optics Express*, 3(3):473, mar 2012.
- [38] Wolfgang Drexler and James G. Fujimoto, editors. *Optical Coherence Tomography*. Springer International Publishing, Cham, 2015.
- [39] W J Dupps and C Roberts. Effect of acute biomechanical changes on corneal curvature after photokeratectomy. *Journal of refractive surgery*, 17(6):658–669, 2001.
- [40] C Edmund. Corneal elasticity and ocular rigidity in normal and keratoconic eyes. *Acta ophthalmologica*, 66:134–140, 1988.
- [41] Ahmed Elsheikh, Daad Alhasso, and Paolo Rama. Biomechanical properties of human and porcine corneas. *Experimental Eye Research*, 86(5):783–790, 2008.

- [42] Ahmed Elsheikh, Stuart Ross, Daad Alhasso, and Paolo Rama. Numerical Study of the Effect of Corneal Layered Structure on Ocular Biomechanics. *Current Eye Research*, 34(1):26–35, jan 2009.
- [43] Ahmed Elsheikh, Defu Wang, Michael Brown, Paolo Rama, Marino Campanelli, and David Pye. Assessment of Corneal Biomechanical Properties and Their Variation with Age. *Current Eye Research*, 32(1):11–19, jan 2007.
- [44] Ahmed Elsheikh, Defu Wang, and David Pye. Determination of the modulus of elasticity of the human cornea. *Journal of refractive surgery*, 23(8):808–818, 2007.
- [45] Shaghayegh Es'haghian, Kelsey M. Kennedy, Peijun Gong, Qingyun Li, Lixin Chin, Philip Wijesinghe, David D. Sampson, Robert A. McLaughlin, and Brendan F. Kennedy. In vivo volumetric quantitative micro-elastography of human skin. *Biomedical Optics Express*, 8(5):2458, may 2017.
- [46] José Ferreira-Mendes, Bernardo T. Lopes, Fernando Faria-Correia, Marcella Q. Salomão, Sandra Rodrigues-Barros, and Renato Ambrósio. Enhanced Ectasia Detection Using Corneal Tomography and Biomechanics. *American journal of ophthalmology*, 197:7–16, jan 2019.
- [47] G Fleischer. Evolutionary principles of the mammalian middle ear. *Advances in anatomy, embryology, and cell biology*, 55(5):3–70, 1978.
- [48] Matthew Ford, William J. Dupps, Nikhil Huprikar, Roger Lin, and Andrew M. Rollins. OCT corneal elastography by pressure-induced optical feature flow. In Fabrice Manns, Per G. Söderberg, and Arthur Ho, editors, *Ophthalmic Technologies XVI*, page 61380P, San Jose, CA, feb 2006. SPIE.
- [49] Matthew R. Ford, William J. Dupps, Andrew M. Rollins, Abhijit Sinha Roy, and Zhilin Hu. Method for optical coherence elastography of the cornea. *Journal of biomedical optics*, 16(January):016005, 2011.
- [50] Matthew R. Ford, Abhijit Sinha Roy, Andrew M. Rollins, and William J. Dupps. Serial biomechanical comparison of edematous, normal, and collagen crosslinked human donor corneas using optical coherence elastography. *Journal of Cataract & Refractive Surgery*, 40(6):1041–1047, jun 2014.
- [51] P Fratzl. *Collagen: Structure and Mechanics, an Introduction*, chapter 1, pages 1–13. Springer US, Boston, MA, 2008.
- [52] J. Fu, M. Haghghi-Abayneh, F. Pierron, and P. D. Ruiz. Depth-Resolved Full-Field Measurement of Corneal Deformation by Optical Coherence Tomography and Digital Volume Correlation. *Experimental Mechanics*, 56(7):1203–1217, sep 2016.

- [53] J. L. Gennisson, T. Deffieux, M. Fink, and M. Tanter. Ultrasound elastography: Principles and techniques. *Diagnostic and Interventional Imaging*, 94(5):487–495, 2013.
- [54] Adrian Glasser and Melanie C.W. Campbell. Presbyopia and the optical changes in the human crystalline lens with age. *Vision research*, 38(2):209–29, jan 1998.
- [55] J. Gloster, E. S. Perkins, and M.-L. Pommier. Extensibility of strips of sclera and cornea. *British Journal of Ophthalmology*, 41(2):103–110, feb 1957.
- [56] José A. P. Gomes, Donald Tan, Christopher J. Rapuano, Michael W. Belin, Renato Ambrósio, José L. Guell, François Malecaze, Kohji Nishida, Virender S. Sangwan, and Group of Panelists for the Global Delphi Panel of Keratoconus and Ectatic Diseases. Global consensus on keratoconus and ectatic diseases. *Cornea*, 34(4):359–69, apr 2015.
- [57] Joseph W Goodman. *Statistical optics*. Wiley classics library. Wiley, New York, wiley classics library ed. edition, 2000.
- [58] Karl F Graff. *Wave Motion in Elastic Solids*. Dover Publications, 1975.
- [59] Zhaolong Han, Salavat R. Aglyamov, Jiasong Li, Manmohan Singh, Shang Wang, Srilatha Vantipalli, Chen Wu, Chih-hao Liu, Michael D Twa, and Kirill V. Larin. Quantitative assessment of corneal viscoelasticity using optical coherence elastography and a modified Rayleigh–Lamb equation. *Journal of Biomedical Optics*, 20(2):020501, feb 2015.
- [60] Zhaolong Han, Jiasong Li, Manmohan Singh, Salavat R. Aglyamov, Chen Wu, Chih-hao Hao Liu, and Kirill V. Larin. Analysis of the effects of curvature and thickness on elastic wave velocity in cornea-like structures by finite element modeling and optical coherence elastography. *Applied Physics Letters*, 106(23):233702, jun 2015.
- [61] Zhaolong Han, Jiasong Li, Manmohan Singh, Chen Wu, Chih-hao Liu, Raksha Raghunathan, Salavat R. Aglyamov, Srilatha Vantipalli, Michael D. Twa, and Kirill V. Larin. Optical coherence elastography assessment of corneal viscoelasticity with a modified Rayleigh-Lamb wave model. *Journal of the Mechanical Behavior of Biomedical Materials*, 66(October 2016):87–94, 2017.
- [62] Ziad Hassan, Laszlo Modis, Eszter Szalai, Andras Berta, and Gabor Nemeth. Examination of ocular biomechanics with a new Scheimpflug technology after corneal refractive surgery. *Contact Lens and Anterior Eye*, 37(5):337–341, oct 2014.
- [63] R Heermann, C Hauger, P R Issing, and T Lenarz. Application of Optical Coherence Tomography (OCT) in middle ear surgery. *Laryngo- rhino- otologie*, 81(6):400–5, jun 2002.

- [64] R S Heffner and H E Heffner. Behavioral hearing range of the chinchilla. *Hearing research*, 52(1):13–6, mar 1991.
- [65] Brien A Holden, Timothy R Fricke, David A Wilson, Monica Jong, Kovin S Naidoo, Padmaja Sankaridurg, Tien Y Wong, Thomas J Naduvilath, and Serge Resnikoff. Global Prevalence of Myopia and High Myopia and Temporal Trends from 2000 through 2050. *Ophthalmology*, 123(5):1036–42, may 2016.
- [66] Kyle W Hollman, Stanislav Y Emelianov, Jason H Neiss, Gagik Jotyan, Gregory J.R. Spooner, Tibor Juhasz, Ron M Kurtz, and Matthew O'Donnell. Strain imaging of corneal tissue with an ultrasound elasticity microscope. *Cornea*, 21(1):68–73, jan 2002.
- [67] D Huang, E. Swanson, C. Lin, J. Schuman, W. Stinson, W Chang, M. Hee, T Flotte, K Gregory, C. Puliafito, and Al. Et. Optical coherence tomography. *Science*, 254(5035):1178–1181, nov 1991.
- [68] Alexander M Huber, Christoph Schwab, Thomas Linder, Sandro J Stoeckli, Mattia Ferrazzini, Norbert Dillier, and Ugo Fisch. Evaluation of Eardrum Laser Doppler Interferometry as a Diagnostic Tool. *The Laryngoscope*, 111(3):501–507, mar 2001.
- [69] Philip David Jaycock, Leon Lobo, Jamal Ibrahim, John Tyrer, and John Marshall. Interferometric technique to measure biomechanical changes in the cornea induced by refractive surgery. *Journal of Cataract & Refractive Surgery*, 31(1):175–184, jan 2005.
- [70] B M Johnstone and A J F Boyle. Basilar Membrane Vibration Examined with the Mossbauer Technique. *Science*, 158(3799):389–390, oct 1967.
- [71] T. Just, E. Lankenau, G. Hüttmann, and H. W. Pau. Optical coherence tomography as a guide for cochlear implant surgery? In Nikiforos Kollias, Bernard Choi, Haishan Zeng, Reza S. Malek, Brian J. Wong, Justus F. R. Ilgner, Kenton W. Gregory, Guillermo J. Tearney, Henry Hirschberg, and Steen J. Madsen, editors, *Proc. SPIE 6842, Photonic Therapeutics and Diagnostics IV*, page 68421F, feb 2008.
- [72] T Just, E Lankenau, G Hüttmann, and H W Pau. Intraoperative application of optical coherence-tomography (OCT) for visualization of the oval window niche. *Laryngo- rhino- otologie*, 88(3):168–73, mar 2009.
- [73] T Just, E Lankenau, G Hüttmann, and H W Pau. Optical coherence tomography in middle ear surgery. *HNO*, 57(5):421–7, may 2009.
- [74] T Just, E Lankenau, G Hüttmann, and H W Pau. Optical coherence tomography of the oval window niche. *The Journal of Laryngology & Otology*, 123(06):603, jun 2009.

- [75] C. Kasai, K. Namekawa, A. Koyano, and R. Omoto. Real-Time Two-Dimensional Blood Flow Imaging Using an Autocorrelation Technique. *IEEE Transactions on Sonics and Ultrasonics*, 32(3):458–464, may 1985.
- [76] Brendan F Kennedy, Robert a McLaughlin, Kelsey M Kennedy, Lixin Chin, Andrea Curatolo, Alan Tien, Bruce Latham, Christobel M Saunders, and David D Sampson. Optical coherence micro-elastography: mechanical-contrast imaging of tissue microstructure. *Biomedical optics express*, 5(7):2113–24, 2014.
- [77] Julien Kerautret, Joseph Colin, David Touboul, and Cynthia Roberts. Biomechanical characteristics of the ectatic cornea. *Journal of Cataract and Refractive Surgery*, 34:510–513, 2008.
- [78] Shyam M. Khanna and Juergen Tonndorf. Tympanic Membrane Vibrations in Cats Studied by Time-Averaged Holography. *The Journal of the Acoustical Society of America*, 51(6B):1904–1920, 1972.
- [79] Mitchell A. Kirby, Ivan Pelivanov, Shaozhen Song, Łukasz Ambrozinski, Soon Joon Yoon, Liang Gao, David Li, Tueng T. Shen, Ruikang K. Wang, and Matthew O'Donnell. Optical coherence elastography in ophthalmology. *Journal of Biomedical Optics*, 22(12):121720, dec 2017.
- [80] Lars Kirsten, Simon Baumgärtner, Mikael Timo Erkkilä, Jonas Golde, Max Kemper, Thomas Stoppe, Matthias Bornitz, Marcus Neudert, Thomas Zahnert, and Edmund Koch. Doppler optical coherence tomography as a promising tool for detecting fluid in the human middle ear. *Current Directions in Biomedical Engineering*, 2(1):443–447, jan 2016.
- [81] Lars Kirsten, Anke Burkhardt, Jonas Golde, Julia Walther, Thomas Stoppe, Matthias Bornitz, Max Kemper, Thomas Zahnert, and Edmund Koch. Imaging the tympanic membrane oscillation ex vivo with Doppler optical coherence tomography during simulated Eustachian catarrh. In Brett E. Bouma and Maciej Wojtkowski, editors, *Proc. SPIE 9541, Optical Coherence Imaging Techniques and Imaging in Scattering Media*, page 95410R, jul 2015.
- [82] J. R. Klauder, A. C. Price, S. Darlington, and W. J. Albersheim. The theory and design of chirp radars. *Bell System Technical Journal*, 39(4):745–808, jul 1960.
- [83] Thomas Klein and Robert Huber. High-speed OCT light sources and systems [Invited]. *Biomedical Optics Express*, 8(2):828, 2017.
- [84] Sabine Kling and Farhad Hafezi. Corneal biomechanics – a review. *Ophthalmic and Physiological Optics*, 37(3):240–252, 2017.
- [85] Aachal Kotecha. What biomechanical properties of the cornea are relevant for the clinician? *Survey of Ophthalmology*, 52(6, Supplement):S109–S114, nov 2007.

- [86] Ronald R Krueger and William J Dupps. Biomechanical effects of femtosecond and microkeratome-based flap creation: prospective contralateral examination of two patients. *Journal of refractive surgery*, 23(8):800–807, oct 2007.
- [87] Sheldon J. J. Kwok, Sarah Forward, Christian M. Wertheimer, Andreas C. Liapis, Harvey H. Lin, Moonseok Kim, Theo G Seiler, Reginald Birngruber, Irene E. Kochevar, Theo Seiler, and Seok-Hyun Yun. Selective Equatorial Sclera Crosslinking in the Orbit Using a Metal-Coated Polymer Waveguide. *Investigative ophthalmology & visual science*, 60(7):2563–2570, jun 2019.
- [88] Andrew K.C. Lam, Davie Chen, and Jimmy Tse. The usefulness of waveform score from the ocular response analyzer, 2010.
- [89] Kirill V. Larin and David D. Sampson. Optical coherence elastography – OCT at work in tissue biomechanics [Invited]. *Biomedical Optics Express*, 8(2):1172, feb 2017.
- [90] Hee Yoon Lee, Patrick D Raphael, Jesung Park, Audrey K Ellerbee, Brian E Applegate, and John S Oghalai. Noninvasive *in vivo* imaging reveals differences between tectorial membrane and basilar membrane traveling waves in the mouse cochlea. *Proceedings of the National Academy of Sciences*, 112(10):3128–3133, mar 2015.
- [91] Rainer A Leitgeb, Maciej Szkulmowski, Cedric Blatter, and Maciej Wojtkowski. *Doppler Fourier Domain Optical Coherence Tomography for Label-Free Tissue Angiography*, pages 1321–1352. Springer International Publishing, Cham, 2015.
- [92] Leonard Levin, Siv Nilsson, James Ver Hoeve, Samuel Wu, Paul Kaufman, and Albert Alm. *Adler's Physiology of the Eye*. Elsevier, 11 edition, 2011.
- [93] Chunhui Li, G Guan, Z Huang, M Johnstone, and R K Wang. Noncontact all-optical measurement of corneal elasticity. *Optics letters*, 37(10):1625–7, may 2012.
- [94] Jiasong Li, Shang Wang, M Singh, S Aglyamov, S Emelianov, M D Twa, and Kirill V. Larin. Air-pulse OCE for assessment of age-related changes in mouse cornea *in vivo*. *Laser Physics Letters*, 11(6):065601, jun 2014.
- [95] Chih-Hao Liu, Dmitry Nevozhay, Alexander Schill, Manmohan Singh, Susobhan Das, Achuth Nair, Zhaolong Han, Salavat Aglyamov, Kirill V. Larin, and Konstantin V. Sokolov. Nanobomb optical coherence elastography. *Optics Letters*, 43(9):2006, may 2018.
- [96] Jun Liu and Cynthia J. Roberts. Influence of corneal biomechanical properties on intraocular pressure measurement. *Journal of Cataract & Refractive Surgery*, 31(1):146–155, jan 2005.

- [97] Linbo Liu, Joseph a Gardecki, Seemantini K Nadkarni, Jimmy D Toussaint, Yukako Yagi, Brett E Bouma, and Guillermo J Tearney. Imaging the subcellular structure of human coronary atherosclerosis using micro-optical coherence tomography. *Nature medicine*, 17(8):1010–1014, 2011.
- [98] M.J.S. Lowe. Matrix techniques for modeling ultrasonic waves in multilayered media. *IEEE Transactions on Ultrasonics, Ferroelectrics and Frequency Control*, 42(4):525–542, jul 1995.
- [99] David A. Luce. Determining in vivo biomechanical properties of the cornea with an ocular response analyzer. *Journal of Cataract and Refractive Surgery*, 31:156–162, 2005.
- [100] Dan MacDougall, Joshua Farrell, Jeremy Brown, Manohar Bance, and Robert Adamson. Long-range, wide-field swept-source optical coherence tomography with GPU accelerated digital lock-in Doppler vibrography for real-time, in vivo middle ear diagnostics. *Biomedical Optics Express*, 7(11):4621, nov 2016.
- [101] Dan MacDougall, Loran Morrison, Christine Morrison, David P. Morris, Manohar Bance, and Robert B. A. Adamson. Optical Coherence Tomography Doppler Vibrometry Measurement of Stapes Vibration in Patients With Stapes Fixation and Normal Controls. *Otology & neurotology*, 40(4):e349–e355, apr 2019.
- [102] Ernest L. Madsen, H. John Sathoff, and James A. Zagzebski. Ultrasonic shear wave properties of soft tissues and tissuelike materials. *The Journal of the Acoustical Society of America*, 74(5):1346–1355, nov 1983.
- [103] Ravi Kiran Manapuram, Salavat R. Aglyamov, Floredes M. Monediado, Maleeha Mashiatulla, Jiasong Li, Stanislav Y. Emelianov, and Kirill V. Larin. In vivo estimation of elastic wave parameters using phase-stabilized swept source optical coherence elastography. *JBO Letters*, 17(10):15–18, 2012.
- [104] Susana Marcos, Giuliano Scarcelli, Antoine Ramier, and Seok H Yun. Probing Ocular Mechanics With Light. In *Encyclopedia of Modern Optics (Second Edition)*, pages 140–154. Elsevier, Oxford, 2018.
- [105] Yogesh K. Mariappan, Kevin J. Glaser, and Richard L. Ehman. Magnetic resonance elastography: A review, 2010.
- [106] Veronica Mas Tur, Cheryl MacGregor, Rakesh Jayaswal, David O’Brart, and Nicholas Maycock. A review of keratoconus: Diagnosis, pathophysiology, and genetics. *Survey of Ophthalmology*, 62(6):770–783, nov 2017.
- [107] Charles N. J. McGhee, Bia Z. Kim, and Peter J. Wilson. Contemporary Treatment Paradigms in Keratoconus. *Cornea*, 34 Suppl 1:S16–23, oct 2015.
- [108] K M Meek. *The Cornea and Sclera*, chapter 13, pages 359–396. Springer US, Boston, MA, 2008.

- [109] K M Meek and N J Fullwood. Corneal and scleral collagens—a microscopist's perspective. *Micron*, 32(3):261–72, apr 2001.
- [110] Keith M. Meek and Craig Boote. The organization of collagen in the corneal stroma. *Experimental Eye Research*, 78(3):503–512, mar 2004.
- [111] Keith M. Meek and Craig Boote. The use of X-ray scattering techniques to quantify the orientation and distribution of collagen in the corneal stroma. *Progress in Retinal and Eye Research*, 28(5):369–392, sep 2009.
- [112] Keith M. Meek, Stephen J. Tuft, Yifei Huang, Paulvinder S. Gill, Sally Hayes, Richard H. Newton, and Anthony J. Bron. Changes in collagen orientation and distribution in keratoconus corneas. *Investigative Ophthalmology and Visual Science*, 46:1948–1956, 2005.
- [113] Marc André Meyers and Krishan Kumar Chawla. *Mechanical Behavior of Materials*. Cambridge University, Cambridge, 2008.
- [114] Eric Mikula, Kyle Hollman, Dongyul Chai, James V. Jester, and Tibor Juhasz. Measurement of Corneal Elasticity with an Acoustic Radiation Force Elasticity Microscope. *Ultrasound in Medicine & Biology*, 40(7):1671–1679, jul 2014.
- [115] Eric R. Mikula, James V. Jester, and Tibor Juhasz. Measurement of an Elasticity Map in the Human Cornea. *Investigative ophthalmology & visual science*, 57(7):3282–6, jun 2016.
- [116] Guillermo L Monroy, Paritosh Pande, Ryan L Shelton, Ryan M Nolan, Darold R Spillman, Ryan G Porter, Michael A Novak, and Stephen A Boppart. Non-invasive optical assessment of viscosity of middle ear effusions in otitis media. *Journal of Biophotonics*, 10(3):394–403, mar 2017.
- [117] Guillermo L Monroy, Ryan L Shelton, Ryan M Nolan, Cac T Nguyen, Michael A Novak, Malcolm C Hill, Daniel T McCormick, and Stephen A Boppart. Non-invasive depth-resolved optical measurements of the tympanic membrane and middle ear for differentiating otitis media. *The Laryngoscope*, 125(8):E276–E282, aug 2015.
- [118] Frank E Musiek and Jane A Baran. *The Auditory System : Anatomy, Physiology, and Clinical Correlates*. Plural Publishing, 2 edition, 2018.
- [119] I S Nash, P R Greene, and C S Foster. Comparison of mechanical properties of keratoconus and normal corneas. *Experimental eye research*, 35(5):413–423, nov 1982.
- [120] Adnan H. Nayfeh. *Wave Propagation in Layered Anisotropic Media : With Applications to Composites*. Elsevier, 1995.

- [121] Ivan Z Nenadic, Matthew W Urban, Scott A Mitchell, and James F Greenleaf. Lamb wave dispersion ultrasound vibrometry (LDUV) method for quantifying mechanical properties of viscoelastic solids. *Physics in Medicine and Biology*, 56(7):2245–2264, apr 2011.
- [122] Cac T Nguyen, Woonggyu Jung, Jeehyun Kim, Eric J Chaney, Michael Novak, Charles N Stewart, and Stephen A Boppart. Noninvasive *in vivo* optical detection of biofilm in the human middle ear. *Proceedings of the National Academy of Sciences*, 109(24):9529–9534, jun 2012.
- [123] Thu-Mai Nguyen, Bastien Arnal, Shaozhen Song, Zhihong Huang, Ruikang K Wang, and Matthew O’Donnell. Shear wave elastography using amplitude-modulated acoustic radiation force and phase-sensitive optical coherence tomography. *Journal of biomedical optics*, 20(1):16001, 2015.
- [124] Thu-Mai Nguyen, Shaozhen Song, Bastien Arnal, Emily Y. Wong, Zhihong Huang, Ruikang K Wang, and Matthew O’Donnell. Shear wave pulse compression for dynamic elastography using phase-sensitive optical coherence tomography. *Journal of Biomedical Optics*, 19(1):016013, jan 2014.
- [125] Alfred L Nuttall, David F Dolan, and G Avinash. Laser Doppler velocimetry of basilar membrane vibration. *Hearing Research*, 51(2):203–213, feb 1991.
- [126] Alfred L. Nuttall and Anders Fridberger. Instrumentation for studies of cochlear mechanics: From von Békésy forward. *Hearing Research*, 293(1-2):3–11, nov 2012.
- [127] Gerald W. Nyquist. Rheology of the cornea: Experimental techniques and results. *Experimental Eye Research*, 7(2):183–188, apr 1968.
- [128] Dolores Ortiz, David Piñero, Mohamed H. Shabayek, Francisco Arnalich-Montiel, and Jorge L. Alió. Corneal biomechanical properties in normal, post-laser *in situ* keratomileusis, and keratoconic eyes. *Journal of Cataract & Refractive Surgery*, 33(8):1371–1375, aug 2007.
- [129] Scott Page, Roozbeh Ghaffari, and Dennis M. Freeman. Doppler optical coherence microscopy and tomography applied to inner ear mechanics. In *AIP Conf. Proc. Mechanics of Hearing: Protein to Perception*, page 040002, 2015.
- [130] B Hyle Park and Johannes F de Boer. *Polarization Sensitive Optical Coherence Tomography*, pages 1055–1101. Springer International Publishing, Cham, 2015.
- [131] Jesung Park, Esteban F Carbajal, Xi Chen, John S Oghalai, and Brian E Applegate. Phase-sensitive optical coherence tomography using an Vernier-tuned distributed Bragg reflector swept laser in the mouse middle ear. *Optics Letters*, 39(21):6233–6, 2014.

- [132] Jesung Park, Jeffrey T. Cheng, Daniel Ferguson, Gopi Maguluri, Ernest W. Chang, Caitlin Clancy, Daniel J. Lee, and Nicusor Iftimia. Investigation of middle ear anatomy and function with combined video otoscopy-phase sensitive OCT. *Biomedical Optics Express*, 7(2):238, 2016.
- [133] Michal E. Pawlowski, Sebina Shrestha, Jesung Park, Brian E. Applegate, John S. Oghalai, and Tomasz S. Tkaczyk. Miniature, minimally invasive, tunable endoscope for investigation of the middle ear. *Biomedical Optics Express*, 6(6):2246, jun 2015.
- [134] Steven J Petsche, Dimitri Chernyak, Jaime Martiz, Marc E Levenston, and Peter M Pinsky. Depth-dependent transverse shear properties of the human corneal stroma. *Investigative Ophthalmology & Visual Science*, 53(2):873, feb 2012.
- [135] Costas Pitriss, Kathleen T Saunders, James G Fujimoto, and Mark E Brezinski. High-Resolution Imaging of the Middle Ear With Optical Coherence Tomography. *Archives of Otolaryngology–Head & Neck Surgery*, 127(6):637, jun 2001.
- [136] Sunil Puria and Jont B. Allen. Measurements and model of the cat middle ear: Evidence of tympanic membrane acoustic delay. *The Journal of the Acoustical Society of America*, 104(6):3463–3481, dec 1998.
- [137] Sunil Puria and Charles Steele. Tympanic-membrane and malleus–incus-complex co-adaptations for high-frequency hearing in mammals. *Hearing Research*, 263(1–2):183–190, may 2010.
- [138] Yueqiao Qu, Youmin He, Arya Saidi, Yihang Xin, Yongxiao Zhou, Jiang Zhu, Teng Ma, Ronald H. Silverman, Don S. Minckler, Qifa Zhou, and Zhongping Chen. In Vivo Elasticity Mapping of Posterior Ocular Layers Using Acoustic Radiation Force Optical Coherence Elastography. *Investigative Ophthalmology & Visual Science*, 59(1):455, jan 2018.
- [139] Yueqiao Qu, Youmin He, Yi Zhang, Teng Ma, Jiang Zhu, Yusi Miao, Cuixia Dai, Mark Humayun, Qifa Zhou, and Zhongping Chen. Quantified elasticity mapping of retinal layers using synchronized acoustic radiation force optical coherence elastography. *Biomedical Optics Express*, 9(9):4054, sep 2018.
- [140] Yueqiao Qu, Teng Ma, Youmin He, Jiang Zhu, Cuixia Dai, Mingyue Yu, Shenghai Huang, Fan Lu, K. Kirk Shung, Qifa Zhou, and Zhongping Chen. Acoustic radiation force optical coherence elastography of corneal tissue. *IEEE Journal of Selected Topics in Quantum Electronics*, 22(3):288–294, may 2016.
- [141] W Radner, M Zehetmayer, C Skorpik, and R Mallinger. Altered organization of collagen in the apex of keratoconus corneas. *Ophthalmic research*, 30(5):327–32, 1998.

- [142] Antoine Ramier, Jeffrey Tao Cheng, Michael E. Ravicz, John J. Rosowski, and Seok-Hyun Yun. Mapping the phase and amplitude of ossicular chain motion using sound-synchronous optical coherence vibrography. *Biomedical Optics Express*, 9(11):5489, nov 2018.
- [143] Antoine Ramier, Behrouz Tavakol, and Seok-Hyun Yun. Measuring mechanical wave speed, dispersion, and viscoelastic modulus of the cornea using optical coherence elastography. *Optics Express*, 27(12):16635, jun 2019.
- [144] J Bradley Randleman, Daniel G Dawson, Hans E Grossniklaus, Bernard E McCarey, and Henry F Edelhauser. Depth-dependent cohesive tensile strength in human donor corneas: implications for refractive surgery. *Journal of refractive surgery (Thorofare, N.J. : 1995)*, 24(1):S85–9, 2008.
- [145] Michael E. Ravicz, Nam H. Cho, Nima Maftoon, and Sunil Puria. Motion of intracochlear structures measured with a commercial optical coherence tomography (OCT) system. *The Journal of the Acoustical Society of America*, 141(5):3896–3897, may 2017.
- [146] Michael E Ravicz and John J Rosowski. Middle-ear velocity transfer function, cochlear input immittance, and middle-ear efficiency in chinchilla. *The Journal of the Acoustical Society of America*, 134(4):2852–2865, oct 2013.
- [147] Marjan Razani, Adrian Mariampillai, Cuiru Sun, Timothy W. H. Luk, Victor X. D. Yang, and Michael C. Kolios. Feasibility of optical coherence elastography measurements of shear wave propagation in homogeneous tissue equivalent phantoms. *Biomedical Optics Express*, 3(5):972, 2012.
- [148] Payam Razavi, Michael E. Ravicz, Ivo Dobrev, Jeffrey Tao Cheng, Cosme Furlong, and John J. Rosowski. Response of the human tympanic membrane to transient acoustic and mechanical stimuli: Preliminary results. *Hearing Research*, 340:15–24, oct 2016.
- [149] Alberto Recio-Spinoso and John S. Oghalai. Mechanical tuning and amplification within the apex of the guinea pig cochlea. *The Journal of Physiology*, apr 2017.
- [150] Tianying Ren, Wenxuan He, and Peter G Barr-Gillespie. Reverse transduction measured in the living cochlea by low-coherence heterodyne interferometry. *Nature communications*, 7:10282, 2016.
- [151] L Robert, J.M Legeais, A.M Robert, and G Renard. Corneal collagens. *Pathologie Biologie*, 49(4):353–363, jan 2001.
- [152] Cynthia J. Roberts and William J. Dupps. Biomechanics of corneal ectasia and biomechanical treatments. *Journal of Cataract and Refractive Surgery*, 40(6):991–998, 2014.

- [153] Luis Robles, Andrei N. Temchin, Yun-Hui Fan, and Mario A. Ruggero. Stapes Vibration in the Chinchilla Middle Ear: Relation to Behavioral and Auditory-Nerve Thresholds. *Journal of the Association for Research in Otolaryngology*, 16(4):447–457, aug 2015.
- [154] John J. Rosowski, Ivo Dobrev, Morteza Khaleghi, Weina Lu, Jeffrey Tao Cheng, Ellery Harrington, and Cosme Furlong. Measurements of three-dimensional shape and sound-induced motion of the chinchilla tympanic membrane. *Hearing research*, 301:44–52, jul 2013.
- [155] John J. Rosowski, Hideko H. Nakajima, and Saumil N Merchant. Clinical utility of laser-Doppler vibrometer measurements in live normal and pathologic human ears. *Ear and hearing*, 29(1):3–19, 2008.
- [156] Abhijit Sinha Roy and William J Dupp. Patient-specific modeling of corneal refractive surgery outcomes and inverse estimation of elastic property changes. *Journal of biomechanical engineering*, 133:011002, 2011.
- [157] Mario A. Ruggero and Nola C. Rich. Application of a commercially-manufactured Doppler-shift laser velocimeter to the measurement of basilar-membrane vibration. *Hearing Research*, 51(2):215–230, 1991.
- [158] Mario A. Ruggero, Nola C. Rich, Luis Robles, and Bhagyalakshmi G. Shivapuja. Middle-ear response in the chinchilla and its relationship to mechanics at the base of the cochlea. *The Journal of the Acoustical Society of America*, 87(4):1612–1629, apr 1990.
- [159] Giuliano Scarcelli, Sebastien Besner, Roberto Pineda, Patricia Kalout, and Seok Hyun Yun. In vivo biomechanical mapping of normal and keratoconus corneas. *JAMA ophthalmology*, 133(4):480–482, apr 2015.
- [160] Giuliano Scarcelli, Sabine Kling, Elena Quijano, Roberto Pineda, Susana Marcos, and Seok Hyun Yun. Brillouin microscopy of collagen crosslinking: Noncontact depth-dependent analysis of corneal elastic modulus. *Investigative Ophthalmology and Visual Science*, 54(2):1418–1425, 2013.
- [161] Giuliano Scarcelli, Roberto Pineda, and Seok Hyun Yun. Brillouin optical microscopy for corneal biomechanics. *Investigative Ophthalmology and Visual Science*, 53:185–190, 2012.
- [162] Giuliano Scarcelli and Seok Hyun Yun. Confocal Brillouin microscopy for three-dimensional mechanical imaging. *Nature Photonics*, 2:39–43, 2008.
- [163] Joseph M. Schmitt. OCT elastography: imaging microscopic deformation and strain of tissue. *Optics Express*, 3(6):199, sep 1998.
- [164] M. Schroeder. Synthesis of low-peak-factor signals and binary sequences with low autocorrelation. *IEEE Transactions on Information Theory*, 16(1):85–89, jan 1970.

- [165] Jan Seifert, Christian M. Hammer, Johannes Rheinlaender, Saadettin Sel, Michael Scholz, Friedrich Paulsen, and Tilman E. Sch??ffer. Distribution of young's modulus in porcine corneas after riboflavin/UVA-induced collagen cross-linking as measured by atomic force microscopy. *PLoS ONE*, 9(1):1–8, 2014.
- [166] T Seiler, M Matallana, S Sendler, and T Bende. Does Bowman's layer determine the biomechanical properties of the cornea? *Refractive & corneal surgery*, 8(2):139–142, 1992.
- [167] Sunil Shah, Mohammed Laiquzzaman, Rajan Bhojwani, Sanjay Mantry, and Ian Cunliffe. Assessment of the biomechanical properties of the cornea with the ocular response analyzer in normal and keratoconic eyes. *Investigative ophthalmology & visual science*, 48(7):3026–31, jul 2007.
- [168] Peng Shao, Amira M. Eltony, Theo G. Seiler, Behrouz Tavakol, Roberto Pineda, Tobias Koller, Theo Seiler, and Seok-Hyun Yun. Spatially-resolved Brillouin spectroscopy reveals biomechanical abnormalities in mild to advanced keratoconus in vivo. *Scientific Reports*, 9(1):7467, dec 2019.
- [169] Peng Shao, Theo G. Seiler, Amira M. Eltony, Antoine Ramier, Sheldon J. J. Kwok, Giuliano Scarcelli, Roberto Pineda II, and Seok-Hyun Yun. Effects of Corneal Hydration on Brillouin Microscopy In Vivo. *Investigative Ophthalmology & Visual Science*, 59(7):3020, jun 2018.
- [170] Meena Siddiqui, Ahhyun S. Nam, Serhat Tozburun, Norman Lippok, Cedric Blatter, and Benjamin J. Vakoc. High-speed optical coherence tomography by circular interferometric ranging. *Nature Photonics*, 12(2):111–116, feb 2018.
- [171] Manmohan Singh, Zhaolong Han, Achuth Nair, Alexander Schill, Michael D. Twa, and Kirill V. Larin. Applanation optical coherence elastography: noncontact measurement of intraocular pressure, corneal biomechanical properties, and corneal geometry with a single instrument. *Journal of Biomedical Optics*, 22(2):020502, 2017.
- [172] Manmohan Singh, Jiasong Li, Srilatha Vantipalli, Shang Wang, Zhaolong Han, Achuth Nair, Salavat R. Aglyamov, Michael D. Twa, and Kirill V. Larin. Non-contact Elastic Wave Imaging Optical Coherence Elastography for Evaluating Changes in Corneal Elasticity Due to Crosslinking. *IEEE Journal of Selected Topics in Quantum Electronics*, 22(3):266–276, may 2016.
- [173] Manmohan Singh, Achuth Nair, Salavat R. Aglyamov, Chen Wu, Zhaolong Han, Ericka Lafon, and Kirill V. Larin. Noncontact optical coherence elastography of the posterior porcine sclera in situ as a function of IOP. In Fabrice Manns, Per G. Söderberg, and Arthur Ho, editors, *Proc. SPIE 10045, Ophthalmic Technologies XXVII*, volume 10045, page 1004524, feb 2017.

- [174] Stephen R. Sloan, Yousuf M. Khalifa, and Mark R. Buckley. The location- and depth-dependent mechanical response of the human cornea under shear loading. *Investigative ophthalmology & visual science*, 55(12):7919–24, oct 2014.
- [175] M K Smolek and B E McCarey. Interlamellar adhesive strength in human eyebank corneas. *Investigative ophthalmology & visual science*, 31(6):1087–95, jun 1990.
- [176] Anders P. Søndergaard, Anders Ivarsen, and Jesper Hjortdal. Corneal resistance to shear force after UVA-riboflavin cross-linking. *Investigative ophthalmology & visual science*, 54(7):5059–69, jul 2013.
- [177] Shaozhen Song, Zhihong Huang, Thu-Mai Nguyen, Emily Y Wong, Bastien Arnal, Matthew O’Donnell, and Ruikang K Wang. Shear modulus imaging by direct visualization of propagating shear waves with phase-sensitive optical coherence tomography. *Journal of Biomedical Optics*, 18(12):121509, nov 2013.
- [178] Shaozhen Song, Zhihong Huang, and Ruikang K. Wang. Tracking mechanical wave propagation within tissue using phase-sensitive optical coherence tomography: motion artifact and its compensation. *Journal of biomedical optics*, 18(12):121505, oct 2013.
- [179] Shaozhen Song, Wei Wei, Bao-Yu Hsieh, Ivan Pelivanov, Tueng T. Shen, Matthew O’Donnell, and Ruikang K. Wang. Strategies to improve phase-stability of ultrafast swept source optical coherence tomography for single shot imaging of transient mechanical waves at 16 kHz frame rate. *Applied Physics Letters*, 108(19):191104, may 2016.
- [180] Robert Stoneley. The Seismological Implications of Aeolotropy in Continental Structure. *Geophysical Supplements to the Monthly Notices of the Royal Astronomical Society*, 5(8):343–353, mar 1949.
- [181] Hrebesh M Subhash, Anh Nguyen-Huynh, Ruikang K Wang, Steven L Jacques, Niloy Choudhury, and Alfred L. Nuttall. Feasibility of spectral-domain phase-sensitive optical coherence tomography for middle ear vibrometry. *Journal of biomedical optics*, 17(6):060505, jun 2012.
- [182] M. Tanter, D. Touboul, Jean Luc Gennisson, Jeremy Bercoff, and Mathias Fink. High-resolution quantitative imaging of cornea elasticity using supersonic shear imaging. *IEEE Transactions on Medical Imaging*, 28:1881–1893, 2009.
- [183] J Tonndorf and S M Khanna. Submicroscopic displacement amplitudes of the tympanic membrane (cat) measured by a laser interferometer. *Journal of the Acoustical Society of America*, 44(6):1546–1554, 1968.
- [184] Andre A M Torricelli, Matthew R. Ford, Vivek Singh, Marcony R. Santhiago, William J. Dupps, and Steven E. Wilson. BAC-EDTA transepithelial riboflavin-UVA crosslinking has greater biomechanical stiffening effect than standard epithelium-off in rabbit corneas. *Experimental Eye Research*, 125:114–117, 2014.

- [185] Michael D Twa, Gongpu Lan, Manmohan Singh, and Kirill Larin. In-vivo human corneal elasticity imaging: a phase sensitive optical coherence elastography method. In *Investigative Ophthalmology & Visual Science. ARVO Annual Meeting*, volume 58, page 4324, Baltimore, MD, 2017.
- [186] B Vakoc, Seok-Hyun Yun, J de Boer, G Tearney, and B Bouma. Phase-resolved optical frequency domain imaging. *Optics express*, 13(14):5483–5493, 2005.
- [187] Hans R. Vellara and Dipika V. Patel. Biomechanical properties of the keratoconic cornea: a review. *Clinical and Experimental Optometry*, 98(1):31–38, jan 2015.
- [188] Georg von Békésy. Über die Messung Schwingungsamplitude der Gehörknöchelchen mittels einer kapazitiven Sonde [About the vibration amplitude of the ossicles measured by means of a capacitive probe]. *Akust Zeits*, 6:1–16, 1941.
- [189] Ruikang K Wang and Alfred L. Nuttall. Phase-sensitive optical coherence tomography imaging of the tissue motion within the organ of Corti at a subnanometer scale: a preliminary study. *Journal of Biomedical Optics*, 15(5):056005, 2010.
- [190] Shang Wang and Kirill V. Larin. Noncontact depth-resolved micro-scale optical coherence elastography of the cornea. *Biomedical optics express*, 5(11):3807–3821, nov 2014.
- [191] Shang Wang, Kirill V. Larin, Jiasong Li, S Vantipalli, R K Manapuram, S Aglyamov, S Emelianov, and M D Twa. A focused air-pulse system for optical-coherence-tomography-based measurements of tissue elasticity. *Laser Physics Letters*, 10(7):075605, 2013.
- [192] Rebecca L Warren, Sripriya Ramamoorthy, Nikola Ciganović, Yuan Zhang, Teresa M Wilson, Tracy Petrie, Ruikang K Wang, Steven L Jacques, Tobias Reichenbach, Alfred L. Nuttall, and Anders Fridberger. Minimal basilar membrane motion in low-frequency hearing. *Proceedings of the National Academy of Sciences*, 113(30):E4304–E4310, jul 2016.
- [193] P.N.T. Wells. Absorption and dispersion of ultrasound in biological tissue. *Ultrasound in Medicine & Biology*, 1(4):369–376, mar 1975.
- [194] S.L-Y Woo, A.S. Kobayashi, W.A. Schlegel, and C. Lawrence. Nonlinear material properties of intact cornea and sclera. *Experimental Eye Research*, 14(1):29–39, jul 1972.
- [195] Woonggyu Jung, Jeehyun Kim, Mansik Jeon, Eric J. Chaney, Charles N. Stewart, and Stephen A. Boppart. Handheld Optical Coherence Tomography Scanner for Primary Care Diagnostics. *IEEE Transactions on Biomedical Engineering*, 58(3):741–744, mar 2011.
- [196] Chen Wu, Zhaolong Han, Shang Wang, Jiasong Li, Manmohan Singh, C.-h. Liu, Salavat Aglyamov, Stanislav Emelianov, Fabrice Manns, and Kirill V. Larin.

- Assessing Age-Related Changes in the Biomechanical Properties of Rabbit Lens Using a Coaligned Ultrasound and Optical Coherence Elastography System. *Investigative Ophthalmology & Visual Science*, 56(2):1292–1300, feb 2015.
- [197] Dan Xia, Shuai Zhang, Jesper Østergaard Hjortdal, Qiang Li, Karen Thomsen, Jacques Chevallier, Flemming Besenbacher, and Mingdong Dong. Hydrated Human Corneal Stroma Revealed by Quantitative Dynamic Atomic Force Microscopy at Nanoscale. *ACS Nano*, 8(7):6873–6882, jul 2014.
 - [198] Siavash Yazdanfar, Changhuei Yang, Marinko V. Sarunic, and Joseph A. Izatt. Frequency estimation precision in Doppler optical coherence tomography using the Cramer-Rao lower bound. *Optics Express*, 13(2):410, 2005.
 - [199] S. Yun, G. Tearney, Johannes de Boer, N. Iftimia, and B. Bouma. High-speed optical frequency-domain imaging. *Optics Express*, 11(22):2953, nov 2003.
 - [200] Seok H. Yun, Guillermo J. Tearney, Benjamin J. Vakoc, Milen Shishkov, Wang Y. Oh, Adrien E. Desjardins, Melissa J. Suter, Raymond C. Chan, John A. Evans, Ik-Kyung Jang, Norman S. Nishioka, Johannes F. de Boer, and Brett E. Bouma. Comprehensive volumetric optical microscopy in vivo. *Nature Medicine*, 12(12):1429–1433, 2006.
 - [201] Thomas Zahnert, Marie-Luise Metasch, Hannes Seidler, Matthias Bornitz, Nicoloz Lasurashvili, and Marcus Neudert. A New Intraoperative Real-time Monitoring System for Reconstructive Middle Ear Surgery. *Otology & Neurotology*, 37(10):1601–1607, dec 2016.